ATTRACTOR AND BIFURCATION MORPHING MODES FOR HIGH-SENSITIVITY SENSING

by

Joosup Lim

A dissertation submitted in partial fulfillment
of the requirements for the degree of
Doctor of Philosophy
(Mechanical Engineering)
in The University of Michigan
2011

Doctoral Committee:

      Associate Professor Bogdan I. Epureanu, Chair
      Professor Robert F. Beck
      Assistant Professor Kenn R. Oldham
      Visiting Research Scholar Matthew P. Castanier

To my family

ACKNOWLEDGEMENTS

TABLE OF CONTENTS

LIST OF FIGURES

LIST OF TABLES

CHAPTER I

Introduction

1.1 Dissertation Objective

Analysis of nonlinear dynamics has been essential in a diversity of engineering fields. The research in this dissertation focuses on analysis of nonlinear dynamics and its applications to sensing. Most of current sensing approaches are to measure variations of linear features of a system to detect variations in parameters of interest. These methods usually focus on minimizing the effects of the nonlinear features. Recently, however, several new studies have been focused on high sensitivity nonlinear features and have discussed how to take advantages of them for high-sensitivity sensing. Particularly, attractor morphing modes and bifurcation morphing modes have been introduced as high-sensitive nonlinear features for application to sensing and damage detection.

While previous studies of sensitivity vector field (SVF) introduced the basic concept of attractor morphing modes and example applications, it was implicitly assumed that SVFs are uniformly linear to small variations in the system parameters throughout the chaotic attractors. For attractor morphing modes, the goal of this dissertation is to discuss several examples where proportionality of SVF is not well achieved due to strong or weak nonlinearities in the SVF. These nonlinearities are undesirable. Hence, a goal is to develop new techniques to expand the applicability of the SVF method to those cases. In this work,

a numerical model of a tapping-mode atomic force microscope (AFM) is introduced as an example. This example is used to discuss nonlinear characteristics of the AFM and to demonstrate a novel operation algorithm of the AFM in chaotic regimes using the SVF approach.

Bifurcation morphing modes are used with nonlinear feedback excitation in applications. This active interrogation approach has been numerically shown to have high sensitivity to variations in the system parameters of interest. However, the bifurcation morphing method has several challenges when used in practical applications. First, the effect of the time delay onto the bifurcation morphing modes should be studied because the time delay cannot be avoided. Second, the time required to detect the bifurcation diagram should be significantly reduced as quick operation is desirable for sensors. Third, sweeping parameters across bifurcation points is not desirable because driving the system into the post-bifurcation regime can be dangerous. Thus, one objective of this work is to develop novel techniques to enhance the bifurcation morphing method for sensing, and to demonstrate experimentally the cantilever-based sensing using the bifurcation morphing method.

To enhance the bifurcation morphing method, a novel approach of forecasting bifurcations is discussed. Forecasting bifurcations before they occur is a significant challenge and an important need in several fields. Existing approaches detect bifurcations before they occur by exploiting the critical slowing down phenomenon. However, the perturbations used in those approaches are limited to being very small, and this represents a significant drawback. Large levels of perturbation have not been used mainly because of a lack of an adequate formulation that is robust to experimental noise. Thus, a goal of this work is to develop a mathematical formulation applicable to large levels of perturbation, and to apply the proposed forecasting approach to enhance the bifurcation morphing method.

1.2 Dissertation Background

1.2.1 Atomic Force Microscopes and Higher Harmonics

Since atomic-force microscopes (AFMs) were introduced [1], they have become important tools for modern nano-science and engineering for nanoscale imaging and surface manipulation. AFMs are able to resolve surfaces at the atomic level for both conducting and nonconducting samples. Their applications are broad, ranging from biological science to nano-electronic engineering. AFMs monitor the dynamics of a microcantilever and a probe tip (which is attached at the end of the microcantilever). The microcantilever interacts with the sample surface through nonlinear atomic interaction forces. Lennard-Jones (LJ) potentials [2–5] are one of the approaches to model these nonlinear forces. Using LJ potentials, a smooth model for the tip-sample interaction is obtained, which approximates the real contact mechanics. In tapping mode, the nonlinear aspects of the AFM dynamics are more significant [6, 7]. Hence, analyzing this nonlinearity is essential for fully enhancing the performance of tapping mode AFM.

Recent studies showed that higher harmonics play an important role in AFMs [8, 9]. Also, by enhancing and exploiting the dynamics of the higher harmonics, the resolution of AFM can be enhanced [10–13]. In particular, Stark showed that the higher harmonics cannot be neglected in the analysis of the tapping mode AFMs [14, 15].

1.2.2 Linear and Nonlinear Analysis for Vibration-Based Methods

Vibration-based techniques have been essential tools for nondestructive system identification [16]. Such system identification has been studied for a variety of problems such as sensing and damage detection. Early studies focused on various linear vibratory properties for damage detection [17–24]. Recently, nonlinear system analysis has become an important part of system identification approaches. In particular, It was showed that use of

nonlinear properties of a system has a great potential to enhance the sensitivity of damage detection. Linear systems subject to chaotic excitation [25–28], and chaotic systems either with or without excitation [29–31] have been discussed. Also, a variety of attractor-based metrics have been demonstrated to quantify geometric changes of attractors in state-space due to system parameter variations. These approaches use attractor dimensions [32, 33], a scalar tracking metric [34, 35], and statistical characterization of the distribution of points in an attractor [30,31,36–38]. Furthermore, pattern recognition techniques based on proper orthogonal decomposition of the shape changes between attractors (for undamaged and damaged systems) were proposed. These methods provide a basis for detecting multiple simultaneous damages and levels [30, 39, 40]. Also, an approach has been proposed to enhance sensitivity by enhancing nonlinearity of linear or weakly nonlinear systems by nonlinear feedback excitations [41, 42].

Nonlinearities have been shown also to be important in micro and nano scale vibration-based methods. Chaotic motions in tapping-mode atomic force microscopy (AFM) have been studied [43–46], and new sensing algorithms using chaotic motions have been discussed also. These include applications of SVFs [44, 45] or local flow variations [47]. The increased importance of AFM [1] also has been accompanied by rapid growth of various other cantilever-based sensing approaches. These approaches are usually monitoring either static (bending-mode) or dynamic (resonant-mode) responses of cantilever beams. Among resonant-mode approaches, MEMS/NEMS resonant mass sensors have demonstrated remarkable sensitivity [48–53]. Monitoring resonant frequency is the most common approach in cantilever-based mass sensors. For higher sensitivity, the use of higher order resonance modes and the reduction of device dimensions have been discussed [54]. Recent approaches have demonstrated to achieve attogram (10^{-18} g) level mass sensing, by using suspended micro-channel resonators [55], or integrated electronic displacement

transducers [56]. While MEMS/NEMS sensors monitoring linear resonant frequencies continues to be studied, sensing techniques using nonlinear features have gained attention also, such as ones focused on electrostatic nonlinear forcing [57], parametric resonances [58, 59], or nonlinear modal interactions [60]. Studies of the nonlinear approaches are important because they suggest that higher sensitivity can be achieved by just changing the algorithm of sensing for the same sensors which use linear techniques, instead of further dimensional and structural modifications.

1.2.3   Forecasting Bifurcations

Forecasting bifurcations is a significant challenge, especially when an accurate model of the system is not available. Specifically, jump phenomena (via subcritical and/or saddle-node bifurcations) are important because they exhibit sudden and dramatic changes in the system dynamics. Jump phenomena have been observed and discussed in a variety of systems, e.g. physical systems governed by equations of motion such as the Schrödinger equation [61] or the Swift-Hohenberg equation [62], climate systems [63], ecological systems [64, 65], biomedical systems (exhibiting behaviors such as asthma [66] or epileptic seizures [67, 68]), neuron systems (exhibiting pulse propagation [69]), and global finance systems [70].

Several characteristics of systems have been discussed for forecasting bifurcations of interest, such as noise-induced spectrum [71], virtual Hopf phenomenon [72], skewness of probability distributions [73] or flickering in bistable regions before bifurcations [74, 75]. In particular, the critical slowing down [76] has been studied as the physical basis of various existing approaches for forecasting bifurcations [77]. Consider an attractor of the dynamics of a system, such as a stable fixed point, a stable limit cycle or a chaotic attractor. When a small perturbation is applied to the system, the dynamics converge

toward the attractor at some recovery rate. The critical slowing down indicates that this recovery rate approaches zero as the size of the basin of attraction shrinks to nil when a parameter of the system approaches the bifurcation point [78]. As a result, in the pre-bifurcation regime, the recovery rates decrease as the system approaches the bifurcation. These effects can be observed quite far from the bifurcation [77]. Therefore, quantifying the effects of the critical slowing down is one method which can be used as an indicator of nearby bifurcations.

Nearby bifurcations have been predicted in various complex systems by monitoring the recovery rates of the system from small perturbations. Methods used have included monitoring changes in the autocorrelation [79] or the variance [80] of the system response to small perturbations (which are consequences of the critical slowing down [77]). These techniques for forecasting bifurcations have been studied for various systems, such as ecosystems [80–82], climate dynamics [83], cell signaling [84], and ocean dynamics [79]. Such studies are still far from being able to predict/forecast the most complicated bifurcations when an accurate model of the system is not available. Also, in current techniques there are often two implicit assumptions that the dynamics of the system takes place on a very low dimensional manifold, and that the bifurcations are co-dimension one. Even more importantly, when a physical system is available for testing, the level of perturbations which can be applied to the system have to be very small. That is because the formulations based on observations of critical slowing down have been derived in close proximity to the attractor (by linearization after eliminating higher order terms).

1.3 Dissertation Outline

The remaining chapters of this dissertation are compiled from a collection of three manuscripts published or accepted to scientific journals and one manuscript prepared for

submission to a scientific journal. Therefore, some of the background materials as well as mathematical developments are repeated in various chapters.

Chapter II expands the SVF approach to a multi-mode system where mode shapes vary due to perturbation in system parameters. The variation of mode shapes creates certain challenges for exploiting SVFs. Specifically, attractor points corresponding to identical initial conditions in the modal space correspond to non-identical physical states. Hence, the sensitivity vectors are not zero at the initial time. However, mode shape variations do not change the most important property of the sensitivity vectors that they are proportional to the parameter variations. Hence, the SVF approach can be applied to parameter reconstruction for multi-mode dynamics. A discussion of the modified SVF approach is presented and several issues related to parameter reconstruction by SVFs are discussed. To ensure linearity during parameter reconstruction (which is a crucial property), a specialized filtering of the sample points used for SVF is required. Through this filtering, one can eliminate undesired possible strong nonlinearity of the SVFs. However, after filtering, certain parameters may be difficult or impossible to reconstruct. There are two reasons for this. First, filtering may cause a significant loss of sensitivity for certain parameter variations. When one parameter has a very low sensitivity compared to the other parameters, it is difficult to reconstruct sets of multiple simultaneous parameter variations that include the low-sensitivity parameter. Second, filtering may cause SVFs for distinct parameters to be linearly dependent. In such situations, it is impossible to reconstruct the parameters which have linearly dependent SVFs. Nonetheless, one can perform parameter reconstructions for sets of parameters which have linearly independent SVFs. One can also observe weak nonlinearity of certain parameters even after filtering the sample points. This issue can be resolved by introducing a correction factor. One can calculate the correction factor from the sample SVFs of the corresponding parameter variations by accounting for the role

of the second order terms. After implementing the novel filtering, the re-selection of the available parameters for reconstruction, and after the calculation of the correction factor, the parameter reconstruction by SVF approach performs well for multiple simultaneous parameter variations. Chapter III introduces several new studies of bifurcation morphing and nonlinear feedback excitation [42] for practical applications in both damage detection and sensing. The primary discussion is focused on the time delay in the nonlinear feedback excitation. This time delay is unavoidable in practical applications due to the delay caused by measuring the dynamics, calculating the nonlinear feedback, and forming the feedback loop. The side-effects of time delays include undesirable high sensitivity of the bifurcation boundary to small variations in the time delay. That is demonstrated by numerical simulation. To alleviate the effects of this side-effect, an additional time delay is introduced as a new design parameter. As the controllable time delay increases, the stable region surrounded by the bifurcation boundary converges to a smaller area. This convergence provides the great advantage of minimizing the effects caused by variability in the time delay. The increased time delay also helps to enhance sensitivity and robustness of the proposed approach. Next, this chapter discusses calibration issues. The sensing approach based on bifurcation morphing requires two bending sensors to be placed at distinct locations on the beam and used to construct nonlinear feedback signals. Various sensor locations are tested to identify the ones which provide the highest sensitivity. By choosing various sensor locations, the proposed method can be adapted for detecting simultaneous damages at multiple locations. These features also enable sensing multiple analytes at multiple locations calibrated for ultra high sensitivity. A multi-mode clamped-free cantilever beam finite element model is used for computational analysis. Bending sensors and uniformly distributed bending moments are used for applying the nonlinear feedback excitation. Density variations for multiple finite elements are considered as models for mass

variations at certain locations. Parameter reconstructions are demonstrated for several test cases (with high sensitivity to simultaneous mass variations at multiple locations).

Chapter IV provides an alternate approach to characterizing the recovery rates of dynamical systems. Specifically, the rate of change of the amplitude of the dynamics (including certain higher order terms) is quantified. This new characterization shows that critical slowing down can also be observed when using much larger levels of perturbation. By tracking the change of the recovery rate from large perturbations, it is possible to predict both stable and unstable branches in a bifurcation diagram. Of course, when an accurate numerical model is available, bifurcation branches can be computed using several computational bifurcation tools, e.g. AUTO [85], DDE-BIFTOOL [86] and PDDE-CONT [87]. Only a few recent studies consider detecting unstable periodic orbits in the bifurcation diagram experimentally [88–90]. These approaches use controllers to stabilize unstable orbits and track them while a parameter of the system is varied. Such approaches are useful in detecting many types of bifurcations. However, controller-based approaches have many requirements. In contrast, the proposed approach does not require a controller and does not need the parameter to vary (or to enter the post-bifurcation region). Instead, this approach predicts the bifurcation and the unstable branches simply by tracking the recovery rate of the system dynamics. These advantages come at the price of limiting the class of bifurcations which can be tracked. Specifically, only Hopf and saddle-node bifurcations can be handled. Nonetheless, the characterized recovery rates can be used to predict both the occurrence and the type of bifurcations (i.e. supercritical or subcritical) before they occur. Numerical simulations and experimental results are provided to demonstrate the use of our technique for forecasting bifurcations. Limit cycle oscillations of a simple mechanical system are used in the experiments. To simulate bifurcations of limit cycle oscillations, properly designed nonlinear feedback excitations are applied so

that the desired types of bifurcations take place in an otherwise linear system. Nonlinear feedback excitations have been employed in structural health monitoring [42, 91] and sensing [92] as an active interrogation approach. However, the feedback control, in this work, is only used as a tool to simulate a desired nonlinear dynamics. The proposed approach does not require any type of control to be applied. As the time scale of the system used herein is very short (compared to several systems used in current studies [77]), our experimental set-up provides large amounts of data in a short time. Moreover, the results obtained using the proposed approach suggest that predictions of bifurcations by critical slowing down can be sufficiently accurate for applications to engineered systems which generally require high precision (such as sensing). Many of engineered systems experience the class of bifurcations of interest here (subcritical/supercritical Hopf bifurcations and/or saddle-node bifurcations), e.g. relief valves [93], shape memory oscillators [94], aeroelastic systems [95], machine tools [96], and automotive components such as torque converter clutches [97].

Chapter V discusses the implementation of the two novel techniques discussed in Chapters III and IV to enhance the bifurcation morphing method as applied to cantilever-based sensors. First, the time delay in the controller is increased to minimize the system's undesirable sensitivity to small variations in the (unavoidable) time delay. Second, a novel approach of forecasting bifurcations is applied to the proposed sensor. This approach significantly reduces the time required to obtain bifurcation diagrams. Both techniques are demonstrated experimentally in detecting mass variations of a test cantilever beam. The cantilever-based sensor based on the bifurcation morphing method is demonstrated to be accurate, quick and robust in the experimental tests.

CHAPTER II

Sensitivity Vector Fields for Atomic Force Microscopes

2.1   Introduction

Atomic-force microscopes (AFMs) have become important tools for modern nano-science and engineering for nanoscale imaging and surface manipulation since they were first introduced [1]. AFMs are capable of resolving surfaces at the atomic level for both conducting and nonconducting samples, and their applications are broad, ranging from biological science to nano-electronic engineering. The core operation of an AFM is based on monitoring the dynamics of a microcantilever and a probe tip (which is attached at the end of the microcantilever). The microcantilever interacts with the sample surface through nonlinear atomic interactive forces. One approach to model these nonlinear forces is by Lennard-Jones (LJ) potentials [2–5]. Using LJ potentials, a smooth model for the tip-sample interaction is obtained, which approximates the real contact mechanics. In tapping mode, the nonlinear aspects of the AFM dynamics are more significant [6, 7]. Hence, analyzing this nonlinearity is essential for fully enhancing the performance of tapping mode AFM.

Recently, it has been observed that higher harmonics play an important role in AFMs [8, 9]. Also, by enhancing and exploiting the dynamics of the higher harmonics, the reso-lution of AFM can be enhanced [10–13]. Stark showed that the higher harmonics cannot

be neglected in the analysis of the tapping mode AFMs [14, 15]. Herein, we show that due to nonlinearities under certain operation conditions, the effects of higher order modes change the predictions for the system dynamics qualitatively from periodic to chaotic motion. These predictions refer to establishing when the response is periodic (limit cycle oscillations) and what are its amplitude and frequency content. Even with a driving force at the first resonance, the predictions for the dynamics obtained during a single mode can be quantitatively inadequate despite the fact that higher order modes have much smaller amplitudes than the first mode. Herein we demonstrate numerically that higher modes affect the dynamics of the system.

A novel concept referred to as sensitivity vector fields (SVFs), and a novel approach to determine multiple parameter variations very accurately [98] are also presented. The proposed approach can be used in many areas such as system identification, sensing, damage detection, and others [39, 99]. The approach allows the detection of simultaneous variations of multiple parameters by exploiting the morphology of chaotic attractors. The application of this method in the context of AFM assists in analyzing the dynamics of the microcantilever and probe tip, enhances its capability of detecting multiple parameter variations, and allows a more effective monitoring of the effective spring constants and other important parameters of the system. Also, the proposed method has the advantage of reducing the calibration effort. This approach opens the door to the accurate operation of AFMs even in chaotic regimes. By using SVFs, one can obtain accurate output information (i.e. reconstructed parameters) even with slight damages or structural changes in the AFM microcantilever.

Hashmi and Epureanu [39] have shown the basic concept for the application of SVFs to AFMs. Herein, that approach is expanded upon for a multi-mode system where mode shapes vary due to perturbation in system parameters. The variation of mode shapes cre-

ates certain challenges for exploiting SVFs. Specifically attractor points corresponding to identical initial conditions in the modal space correspond to non-identical physical states. Hence, the sensitivity vectors are not zero at the initial time. However, mode shape variations do not change the most important property of the sensitivity vectors that they are proportional to the parameter variations. Hence, the SVF approach can be applied to parameter reconstruction for multi-mode dynamics. A discussion of the modified SVF approach is presented and several issues related to parameter reconstruction by SVFs are discussed.

To ensure linearity during parameter reconstruction (which is a crucial property), a specialized filtering of the sample points used for SVF is required. Through this filtering, one can eliminate undesired possible strong nonlinearity of the SVFs. However, after filtering, certain parameters may be difficult or impossible to reconstruct. There are two reasons for this. First, filtering may cause a significant loss of sensitivity for certain parameter variations. When one parameter has a very low sensitivity compared to the other parameters, it is difficult to reconstruct sets of multiple simultaneous parameter variations that include the low-sensitivity parameter. Second, filtering may cause SVFs for distinct parameters to be linearly dependent. In such situations, it is impossible to reconstruct the parameters which have linearly dependent SVFs. Nonetheless, one can perform parameter reconstructions for sets of parameters which have linearly independent SVFs.

One can also observe weak nonlinearity of certain parameters even after filtering the sample points. This issue can be resolved by introducing a correction factor. One can calculate the correction factor from the sample SVFs of the corresponding parameter variations by accounting for the role of the second order terms. After implementing the novel filtering, the re-selection of the available parameters for reconstruction, and after the calculation of the correction factor, the parameter reconstruction by SVF approach performs

Figure 2.1: Schematic of the AFM microcantilever model showing tip-sample distance Z, beam deflection $u(x, t)$, base excitation $y(t)$, and static deflection $\tilde{w}$.

well for multiple simultaneous parameter variations, as shown in the following.

2.2 Modeling and Parameter Reconstruction using SVFs

2.2.1 AFM Microcantilever Model

Various researchers have proposed models for the tip-sample interaction in tapping mode AFM [100–103]. Some approaches consider this interaction as piecewise smooth while others account for the contact mechanics by employing strongly nonlinear, yet smooth potentials. One of the latter models is based on LJ potentials, which account for the attractive and repulsive tip-sample interaction forces. Although the LJ potentials lead to a smooth set of equations, the model closely approximates the contact mechanics through the use of very strong nonlinearities. Herein, we choose to use LJ potentials to avoid mathematical complexity while taking advantage of its qualitative resemblance to the real contact mechanics. In general, regardless of the specific details of the model used, the SVF approach can be employed. In fact, the SVF approach can be applied even without a model as long as the parameters of the dynamics are not of interest, and the only identified quantity is the distance to sample.

The LJ potential energy and the corresponding tip-sample interaction force for an AFM microcantilever are given in the literature [104] as

$$U_{LJ} = \frac{A_1 R}{1260 Z^7} - \frac{A_2 R}{6Z}, \qquad P_{LJ} = -\frac{\partial U_{LJ}}{\partial Z} = \frac{A_1 R}{180 Z^8} - \frac{A_2 R}{6Z^2}, \qquad (2.1)$$

where A_1, A_2 are the Hamaker constants, R is the radius of the probe tip, and Z is an instantaneous gap between the tip and the surface of sample as shown in FIG. 2.1. A single mode model has been used in the past [105]. Herein, the effects of higher order modes are of interest in the context of multiple simultaneous parameter variations. The static deflection $\tilde{w}(x)$ of the microcantilever may be obtained from

$$EI\tilde{w}''''(x) = 0, \qquad (2.2)$$

with the boundary conditions expressed as

$$\begin{aligned}
\tilde{w}(0) &= 0, \\
\tilde{w}'(0) &= 0, \\
\tilde{w}''(L) &= 0, \\
-EI\tilde{w}'''(L) &= -\frac{A_1 R}{180[Z - \tilde{w}(L)]^8} + \frac{A_2 R}{6[Z - \tilde{w}(L)]^2}, \quad (2.3)
\end{aligned}$$

where L is the length of the microcantilever. The equilibrium gap between the tip and sample is denoted by $\tilde{\eta} = Z - \tilde{w}(L)$. The total time-dependent deflection of the micro-cantilever $w(x, t)$ may be expressed as

$$w(x, t) = \tilde{w}(x) + y(t) + u(x, t), \qquad (2.4)$$

where $u(x, t)$ is the microcantilever deflection relative to a non-inertial frame attached to its moving base, as shown in FIG. 2.1, and $y(t)$ is the excitation which is applied as base excitation by a piezoelectric actuator located at the left end of the microcantilever

in FIG. 2.1. The base excitation $y(t)$ is modeled as a harmonic motion $y(t) = Y \sin \Omega t$.

Next, the equation of motion of the vibrating microcantilever may be expressed as

$$
\begin{aligned}
\rho A \ddot{u}(x,t) \quad &+ EI \left[u''''(x,t) + \tilde{w}''''(x) \right] \\
= \quad &\left\{ -\frac{A_1 R}{180[\tilde{\eta} - u(L,t) - Y \sin \Omega t]^8} \right. \\
&\left. + \frac{A_2 R}{6[\tilde{\eta} - u(L,t) - Y \sin \Omega t]^2} \right\} \delta(x - L) \\
&+ \rho A \Omega^2 Y \sin \Omega t,
\end{aligned}
\tag{2.5}
$$

where ρ is the material density, A is the cross sectional area, and A_1, A_2 are Hamaker constants for the microcantilever, and δ is the delta function. Eq. (2.5) may be rearranged by using

$$
EI \tilde{w}''''(x) = \left[-\frac{A_1 R}{180 \tilde{\eta}^8} + \frac{A_2 R}{6 \tilde{\eta}^2} \right] \delta(x - L)
\tag{2.6}
$$

to obtain

$$
\begin{aligned}
\rho A \ddot{u}(x,t) \quad &+ EI u''''(x,t) \\
= \quad &\left\{ -\frac{A_1 R}{180} \left[\frac{1}{[\tilde{\eta} - u(L,t) - Y \sin \Omega t]^8} - \frac{1}{\tilde{\eta}^8} \right] \right. \\
&\left. + \frac{A_2 R}{6} \left[\frac{1}{[\tilde{\eta} - u(L,t) - Y \sin \Omega t]^2} - \frac{1}{\tilde{\eta}^2} \right] \right\} \delta(x - L) \\
&+ \rho A \Omega^2 Y \sin \Omega t.
\end{aligned}
\tag{2.7}
$$

Next, a Ritz approach is used to discretize Eq. (2.7) in space and obtain a set of ordinary differential equations. To solve for the linear eigenmodes, one may consider the linearized system around its static equilibrium position. Using Eq. (2.1), the linearized equivalent spring constant k_{LJ} caused by the gradient of the LJ potential at the equilibrium position may be expressed as

$$
k_{LJ} = -\left. \frac{\partial P_{LJ}(Z, w(L,t))}{\partial w(L,t)} \right|_{u=0} = \frac{2 A_1 R}{45 \left[Z - \tilde{w}(L) \right]^9} - \frac{A_2 R}{3 \left[Z - \tilde{w}(L) \right]^3}.
\tag{2.8}
$$

Next, the deflection $u(x, t)$ can be expressed as a sum of eigenmodes as follows

$$u(x, t) = \sum_{n=1}^{\infty} U_n(x) T_n(t). \tag{2.9}$$

The equation of the free (unforced) linearized system for each eigenmode is

$$U_n'''' - \beta_n^4 U_n = 0, \tag{2.10}$$

where $\beta_n^4 = \frac{\rho A \omega_n^2}{EI}$, and the boundary conditions are given by

$$
\begin{aligned}
U_n(0) &= 0, \\
U_n'(0) &= 0, \\
U_n''(L) &= 0, \\
-EIU_n''''(L) &= -k_{LJ} U_n(L). \tag{2.11}
\end{aligned}
$$

The ordinary differential equations for $T_n(t)$ are obtained in the usual Galerkin fashion by substituting $u(x, t)$ from Eq. (2.9) into Eq. (2.7) and by taking the inner products with each of the mode shapes. Finally, one obtains an equation of motion for each mode.

The modal amplitudes T_n are nondimensionalized as $\xi_n = \frac{U_{n0}(L) T_n}{\tilde{\eta}_0}$, where U_{n0} and $\tilde{\eta}_0$ are the nominal value of n-th mode shape at $x = L$ and the equilibrium gap between the tip and sample for the nominal system. The parameters of interest for reconstruction are denoted by $P_1 = A_1 R$, $P_2 = A_2 R$, $P_3 = EI$, $P_4 = Z$, and $P_5 = \bar{y} = \frac{Y}{\tilde{\eta}_0}$. The nonlinear equations of motion in linear modal coordinates are obtained as

$$
\begin{aligned}
\ddot{\xi}_n = {} & -d\dot{\xi}_n - \frac{\omega_n^2}{\omega_{10}^2} \xi_n \\
& + \kappa_n C_{n1} \left\{ \frac{1}{(\epsilon - \xi_{tot} - P_5 \sin \bar{\Omega}\tau)^8} - \frac{1}{\epsilon^8} \right\} \\
& + \kappa_n C_{n2} \left\{ \frac{1}{(\epsilon - \xi_{tot} - P_5 \sin \bar{\Omega}\tau)^2} - \frac{1}{\epsilon^2} \right\} \\
& + E_n P_5 \bar{\Omega}^2 \sin \bar{\Omega}\tau, \tag{2.12}
\end{aligned}
$$

where subscript 0 indicates a nominal value, and

$$\omega_n^2 = \frac{P_3 f_{n3}}{\rho A f_{n2}}, \quad \xi_n = \frac{U_{n0}(L) T_n(\tau)}{\tilde{\eta}_0}, \quad \tau = \omega_{10} t, \quad \bar{y} = P_5 = \frac{Y}{\tilde{\eta}_0},$$

$$\bar{\Omega} = \frac{\Omega}{\omega_{10}}, \quad \xi_{tot} = \sum_{n=1}^{\infty} \kappa_n \xi_n, \quad w_{10} = \text{ unperturbed value of } w_1,$$

$$\kappa_n = \frac{U_n(L)}{U_{n0}(L)}, \quad E_n = U_{n0}(L) \frac{f_{n1}}{f_{n2}}, \quad d = \text{damping parameter},$$

$$C_{n1} = -\frac{U_{n0}^2(L)}{180 \rho A \tilde{\eta}_0^9 \omega_{10}^2} \frac{P_1}{f_{n2}}, \quad C_{n2} = \frac{U_{n0}^2(L)}{6 \rho A \tilde{\eta}_0^3 \omega_{10}^2} \frac{P_2}{f_{n2}}, \quad \epsilon = \frac{\tilde{\eta}}{\tilde{\eta}_0},$$

$$f_{n1} = \int_0^L U_n dx, \quad f_{n2} = \int_0^L U_n^2 dx, \quad f_{n3} = \int_0^L U_n U_n'''' dx.$$

2.2.2 SVFs for a Multi-Mode Model

The basic algorithm for the SVF method [39, 98, 99] can be summarized as follows. Individual sensitivity vectors are collected throughout the attractor for a given set of parameter variations. These sensitivity vectors are then grouped to form one SVF, which is interpreted as a snapshot. Distinct SVFs are recorded under known sets of parameter variations. The collection of snapshots is analyzed by proper orthogonal decomposition to construct an optimal basis for representing all SVFs using a small number of basis vector fields. Each of these basis fields corresponds to a known set of parameter variations (in the parameter space). Once this optimal basis is constructed, detection can be implemented as follows. A SVF is sampled by using the attractor of the dynamics for a system with an unknown set of parameter variations. Next, the sampled SVF is projected along the optimal basis of fields. Finally, the coordinates along each of these basis fields are used to identify/reconstruct the unknown parameter variations. To form SVFs across the attractor, randomly chosen sample points within the attractor are used as initial points for calculation of SVFs. The sample points are selected by sampling the system response in time. Note that the fact that the attractor is visited by the trajectory ensures that the samples are likely distributed throughout the attractor. However, the number of cycles need to use SVFs is

likely larger than that of other linear-based techniques. Nonetheless, that may be acceptable in many applications and is accompanied by two significant advantages: detection of multiple simultaneous parameters and increased sensitivity as discussed next.

From Eq. (2.12), each sample point in state space has $2k$ state variables for a k-mode approximate model. A state vector for each sample point can be defined as

$$\mathbf{z}_i = \begin{bmatrix} \kappa_1 \xi_{i1} & \kappa_1 \dot{\xi}_{i1} & \cdots & \kappa_k \xi_{ik} & \kappa_k \dot{\xi}_{ik} \end{bmatrix}^T. \tag{2.13}$$

For simplicity of indexing variables, we define $\bar{\kappa}_{2l-1} = \kappa_l$ and $\bar{\kappa}_{2l} = \kappa_l$. Also, we define $\bar{U}_{2l-1}(L) = U_l(L)$ and $\bar{U}_{2l}(L) = U_l(L)$. Hence, Eq. (2.13) becomes

$$\mathbf{z}_i = \begin{bmatrix} \bar{\kappa}_1 z_{i1} & \bar{\kappa}_2 z_{i2} & \cdots & \bar{\kappa}_{2k-1} z_{i(2k-1)} & \bar{\kappa}_{2k} z_{i2k} \end{bmatrix}^T, \tag{2.14}$$

where i is the index of a sample point. A snapshot vector can be defined for the whole set of sample points for a given set of parameters as

$$\boldsymbol{\sigma} = \begin{bmatrix} \mathbf{z}_1 & \cdots & \mathbf{z}_i & \cdots & \mathbf{z}_N \end{bmatrix}^T, \tag{2.15}$$

where N is the total number of sample points. Numerically, the SVF can be defined as the difference between the snapshot vectors of the perturbed and unperturbed systems, which can be expressed as

$$\mathbf{s} = \delta \boldsymbol{\sigma} = \boldsymbol{\sigma}_p - \boldsymbol{\sigma}_0, \tag{2.16}$$

where $\boldsymbol{\sigma}_p$ is the snapshot vector for the perturbed system, and $\boldsymbol{\sigma}_0$ is the snapshot vector for the unperturbed system. This numerical SVF is a representation for the SVF expressed as

$$\mathbf{s} = \delta \boldsymbol{\sigma} = \begin{bmatrix} \dfrac{\partial \mathbf{z}_1}{\partial \mathbf{P}} \bigg|_{\mathbf{P}_0} \delta \mathbf{P} & \cdots & \dfrac{\partial \mathbf{z}_i}{\partial \mathbf{P}} \bigg|_{\mathbf{P}_0} \delta \mathbf{P} & \cdots & \dfrac{\partial \mathbf{z}_N}{\partial \mathbf{P}} \bigg|_{\mathbf{P}_0} \delta \mathbf{P} \end{bmatrix}^T, \tag{2.17}$$

where $\mathbf{P}$ is a vector containing all parameters. One can further expand each entry j of the

Property	Symbol	Value
length	L	449 μm
width	b	46 μm
thickness	h	1.7 μm
tip radius	R	150 nm
material density	ρ	2330 kg/m^3
elastic modulus	E	176 GPa
1$^{\text{st}}$ resonance	f_1	11.804 kHz
Hamaker (repulsive)	A_1	1.3596×10^{-70} Jm^6
Hamaker (attractive)	A_2	1.865×10^{-19} J

Table 2.1: Properties of the microcantilever

column i of $\mathbf{s}$ as

$$
\begin{aligned}
\left(\left. \frac{\partial \mathbf{z}_i}{\partial \mathbf{P}} \right|_{\mathbf{P}_0} \delta \mathbf{P} \right)_j &= \left. \frac{\partial \left(\bar{\kappa}_j z_{ij} \right)}{\partial \mathbf{P}} \right|_{\mathbf{P}_0} \delta \mathbf{P} \qquad (\text{for } j = 1, \cdots, 2k) \\
&= \bar{\kappa}_j \left. \frac{\partial z_{ij}}{\partial \mathbf{P}} \right|_{\mathbf{P}_0} \delta \mathbf{P} + \left. \frac{\partial \bar{\kappa}_j}{\partial \mathbf{P}} \right|_{\mathbf{P}_0} z_{ij} \delta \mathbf{P} \\
&= \frac{\bar{U}_j}{\bar{U}_{j0}} \left. \frac{\partial z_{ij}}{\partial \mathbf{P}} \right|_{\mathbf{P}_0} \delta \mathbf{P} + \frac{1}{\bar{U}_{j0}} \left. \frac{\partial \bar{U}_j}{\partial \mathbf{P}} \right|_{\mathbf{P}_0} z_{ij} \delta \mathbf{P} \\
&= \left. \frac{\partial z_{ij}}{\partial \mathbf{P}} \right|_{\mathbf{P}_0} \delta \mathbf{P} + \frac{1}{\bar{U}_{j0}} \left. \frac{\partial \bar{U}_j}{\partial \mathbf{P}} \right|_{\mathbf{P}_0} z_{ij} \delta \mathbf{P}, \qquad (2.18)
\end{aligned}
$$

where $\bar{U}_j = \bar{U}_{j0} + \left. \frac{\partial \bar{U}_j}{\partial \mathbf{P}} \right|_{\mathbf{P}_0} \delta \mathbf{P}$. Eq. (2.18) shows that $\mathbf{s}$ is non-zero at the initial sampling time because $\frac{1}{\bar{U}_{j0}} \left. \frac{\partial \bar{U}_j}{\partial \mathbf{P}} \right|_{\mathbf{P}_0} z_{ij} \delta \mathbf{P}$ is nonzero. This is caused by the variations of the mode shapes due to the parameter variations. The initial nonzero term, however, also ensures the most important property of the SVF that it is proportional to $\delta \mathbf{P}$. Note that $\left. \frac{\partial z_{ij}}{\partial \mathbf{P}} \right|_{\mathbf{P}_0}$ is zero at the initial sampling time because, at that instant, $\left. \frac{\partial \xi_{ij}}{\partial \mathbf{P}} \right|_{\mathbf{P}_0}$ and $\left. \frac{\partial \dot{\xi}_{ij}}{\partial \mathbf{P}} \right|_{\mathbf{P}_0}$ are zero for all parameter values.

2.3 Enhancements and Results

A numerical analysis is carried out for the representative case of the interaction of a soft monocrystalline silicon microcantilever with the (111) reactive face of a flat silicon sample used by Rutzel et al. [105]. The Si-Si interaction parameters are taken from Pfeiffer et al.

a. Phase portrait of tip displacement

b. Time history of the tip displacement

c. Phase portrait of 1st mode

d. Phase portrait of 2nd mode
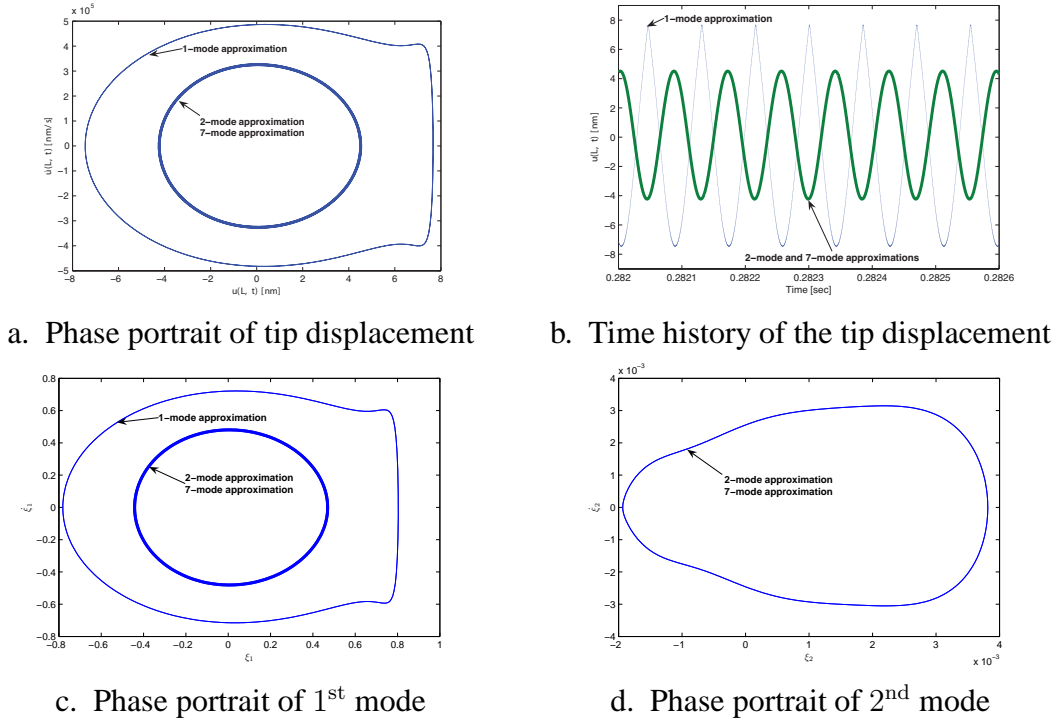
Figure 2.2: The frequency of the base excitation is at 1st resonance (11.8 kHz). The motion of the tip predicted by a 1-mode approximation is different from that of (more accurate) multi-mode approximations, from 2-mode through 7-mode.

[106], and corresponding attractive and repulsive Hamaker constants are from Israelachvili

[107] and Basso et al. [108]. The physical parameters used are listed in Tab. 2.1.

2.3.1 Importance of the Higher Harmonics

When the frequency of the base excitation is at the first resonant frequency of 11.8 kHz, the responses of the higher order modes are very small in deflection and velocity. However, the motion of the tip predicted by a 1-mode approximation is different from that of (more accurate) multi-mode approximations, from 2-mode through 7-mode. Figs. 2.2a and 2.2b show that the predictions for the tip motion converge if at least 2 modes are used in the approximation. Figs. 2.2c and 2.2d show, in modal coordinates, that the use of the first 2 modes leads to a converged prediction for the dynamics. These results show that a 1-mode model may be inaccurate even if the higher harmonics are much smaller in amplitudes

a. 1-mode approximation   b. 2-mode approximation
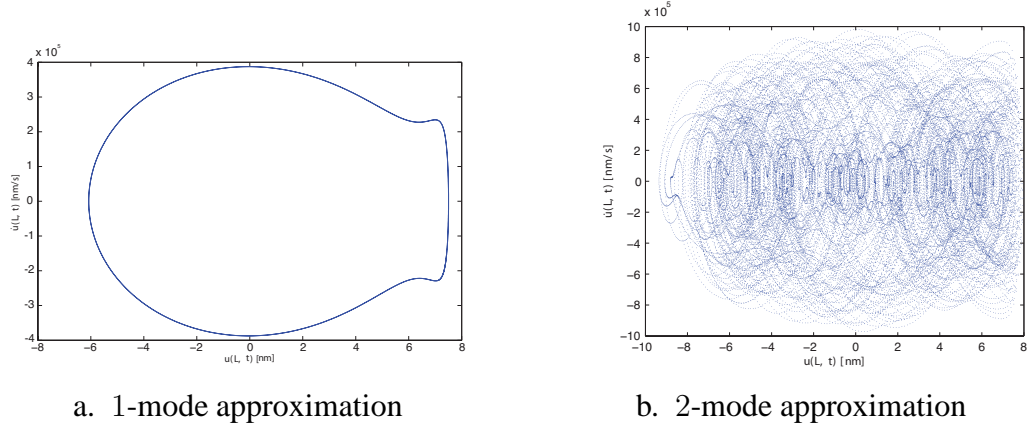
Figure 2.3: The frequency of the base excitation is 9.9 kHz, away from the 1st resonance. Figures above are phase portraits of the tip displacement obtained by approximations with different numbers of modes. The system dynamics changes from periodic motion to chaotic motion due to the effects of the second mode.

than the first mode.

One may suspect that the results in Fig. 2.2 are caused by two coexisting attractors (i.e. a bistable regime). We explored this interesting possibility and found that the cases studied do not belong to a bistable regime. To check that, we started the time marching simulation using a 1-mode model from initial conditions which are very closely along the limit cycles observed using the multi-mode models. Also, we started the time marching simulation using the multi-mode models from initial conditions which are precisely along the limit cycles observed using the 1-mode models. In all cases, the trajectory experiences transients and eventually settles onto the same limit cycles as presented in Fig. 2.2, without exhibiting bistability.

Next, we consider a case where the excitation frequency is away from the first resonance. A numerical computation was carried out with the excitation frequency at 9.9 kHz. The system dynamics changes from periodic motion to chaotic motion by adding the effects of the second mode (as shown in Figs. 2.3a and 2.3b). Figs. 2.2 and 2.3 show not only that a 1-mode approximation is not enough to quantify the dynamics of the system,
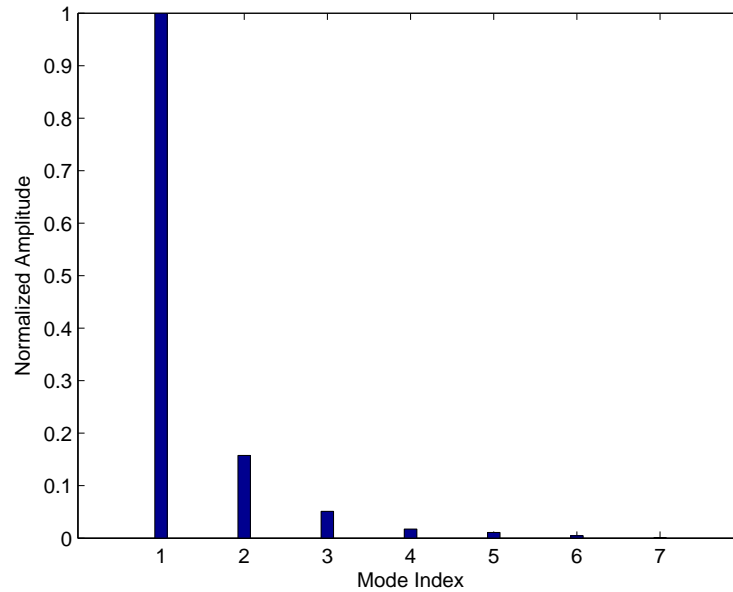
Figure 2.4: The normalized amplitude of each mode is presented for a base excitation of 9.9 kHz. The amplitude of the higher modes is shown to decrease rapidly from the 2nd mode, to much less than 1% of the 1st mode amplitude for the 4th mode.

but they show also that a 1-mode approximation may fail to predict even qualitatively the dynamics of the system. Note that in FIG. 2.4, the amplitude of the higher modes is shown to decrease rapidly from the 2nd mode, to much less than 1% of the 1st mode amplitude for the 4th mode. Hence, a 3-mode model is used in the results hereafter.

2.3.2 Sample Points and Verification of the SVFs

To perform parameter reconstruction by using the SVF approach, one first chooses the sample points to be used from the (tip displacement) attractor of the system. The axes in the plots in FIG. 2.5 show the displacement and velocity of the tip of the microcantilever. The points in FIG. 2.5a are collected at instants in time which are separated by one period T of the excitation. Thus, FIG. 2.5a is a Poincar map of the dynamics (for the tip of the cantilever) of the 3-mode approximate model of the AFM microcantilever. The

a. Attractor of the system   b. Sample points from the attractor
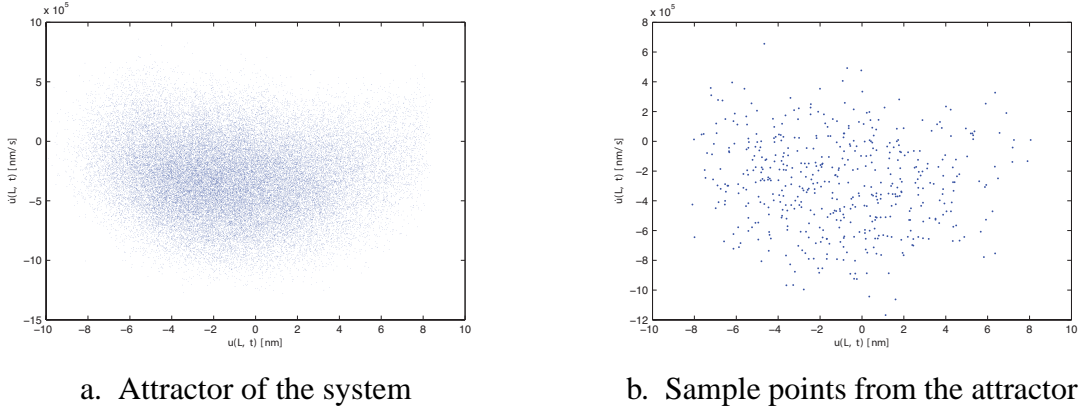
Figure 2.5: The attractor of the system is shown in a Poincaré map. The axes are the displacement and velocity of the tip of the microcantilever. 500 sample points are randomly chosen over the attractor for the calculation of the sensitivity vectors.

points shown in FIG. 2.5b represent the sampled points where the sensitivity vectors are calculated. In general, the sensitivity vectors do not have to be collected at all points in the (sampled) attractor, but just at a few of these points. In the study discussed herein, 500 sample points were randomly chosen. However the number of samples does not necessarily have to be as large as 500. We chose this large number of sample points to demonstrate the linear independence of the SFVs and discuss certain issues related to the nonlinearity of sensitivity vectors at some locations (as presented in the next sections). Theoretically, there can be as few sample points as parameters to be detected. Hence, the number of cycles at a single locus does not have to be extremely large. However, while that theoretical lower limit is possible, the approach performs much better when more points are used, especially when multiple parameters are to be identified and noise is present in the data.

Note that ΔT can be interpreted as a tool for adjusting the sensitivity of the analysis. For short ΔT, the sensitivity is low, whereas for long ΔT, the sensitivity tends to be higher. Thus, from the perspective of experimental measurements, the crucial issue is the level of parameter variation that is of interest and the capability of the experimental apparatus (i.e. the sampling rate and the smallest measurable ΔT). If the parameter variations of interest

a. 0.1% variation for each parameter   b. Modified variation for each parameter
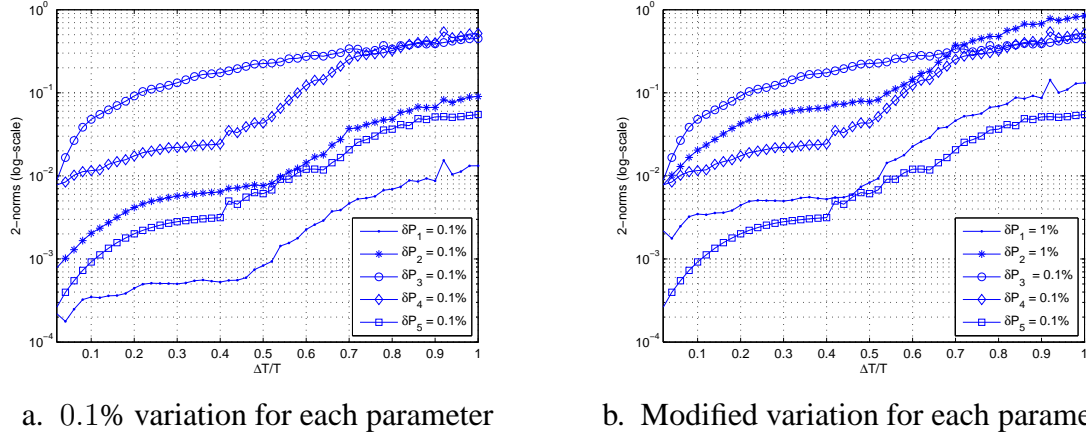
Figure 2.6: The 2-norm of the sensitivity vector fields ($\|\mathbf{s}\|_2$) for a fixed parameter variation of 0.1% (referred to as the baseline parameter variation) of each parameter is plotted to check the sensitivity level of the SVFs. With same variation level of each parameter, the sensitivities of the SVFs for P_1, P_2, and P_5 are lower than those of P_3 and P_4. Hence, levels of parameter variations δP_1 and δP_2 larger than δP_3 and δP_4 are considered for reconstruction. Thus, values of 1% for δP_1 and δP_2 are considered as the baseline for variations in P_1 and P_2. As a direct result of that choice, the magnitudes of the SVFs for P_1 and P_2 increase.

are small, then a larger ΔT should be used. The values for ΔT used in this study are of the order of one period T of the excitation. The best results were obtained for ΔT of approximately $0.4\,T$.

2.3.3 Level of Sensitivity of the SVFs

After verifying the calculation of the SVFs, the parameter reconstruction has been tested for all 5 parameters $P_1 = A_1 R$, $P_2 = A_2 R$, $P_3 = EI$, $P_4 = Z$, and $P_5 = \bar{y}$. It is observed that the parameter set (P_3, P_4, P_5) is reconstructed well for cases with a low level of variation (lower than 0.5%), while the whole set of 5 parameters cannot be reconstructed accurately. To investigate the causes of the failure of the parameter reconstruction that include P_1 and P_2, one can check the sensitivity of the SVFs for each parameter variation. To check this sensitivity, one can observe the 2-norm of the sensitivity vector fields ($\|\mathbf{s}\|_2$) for a fixed parameter variation of 0.1% (referred to as the baseline parameter variation)

a. Proportionality, p b. Linear dependence
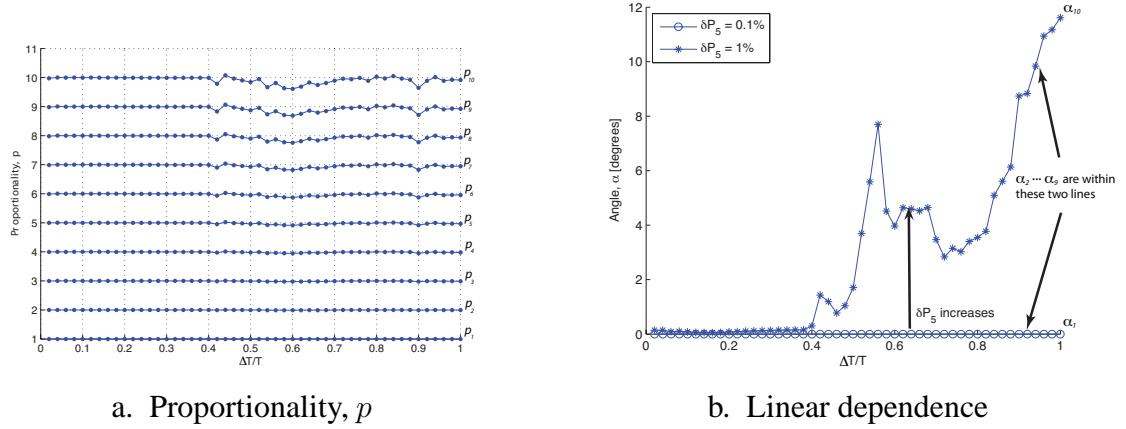
Figure 2.7: The linearity of SVFs for various levels of parameter variation δP_5 is demonstrated in two figures in terms of proportionality and angles between the baseline and the other parameter variations. The linear increases of p_j and small values of α_j indicate a strong linearity of the SVFs with respect to the parameter variation δP_5.

of each parameter. As shown in FIG. 2.6a, the sensitivities of the SVFs for P_1, P_2, and P_5 are lower than those of P_3 and P_4. Hence, only levels of parameter variations δP_1 and δP_2 larger than δP_3 and δP_4 can be reconstructed. Thus, values of 1% for δP_1 and δP_2 are considered as the baseline for variations in P_1 and P_2. Of course, a direct result of that choice is that the magnitude of the SVFs for P_1 and P_2 increase, as shown in FIG. 2.6b.

2.3.4 Linearity of the SVFs

The most important property of the SVFs is that they vary linearly with the level of variation in each single parameter. To check this linearity, one can generate 10 test SVFs for each parameter starting from the baseline parameter variation and up to 10 times that variation. A proportionality factor and an angle between SVFs can be defined for each

a. Proportionality, p b. Linear dependence
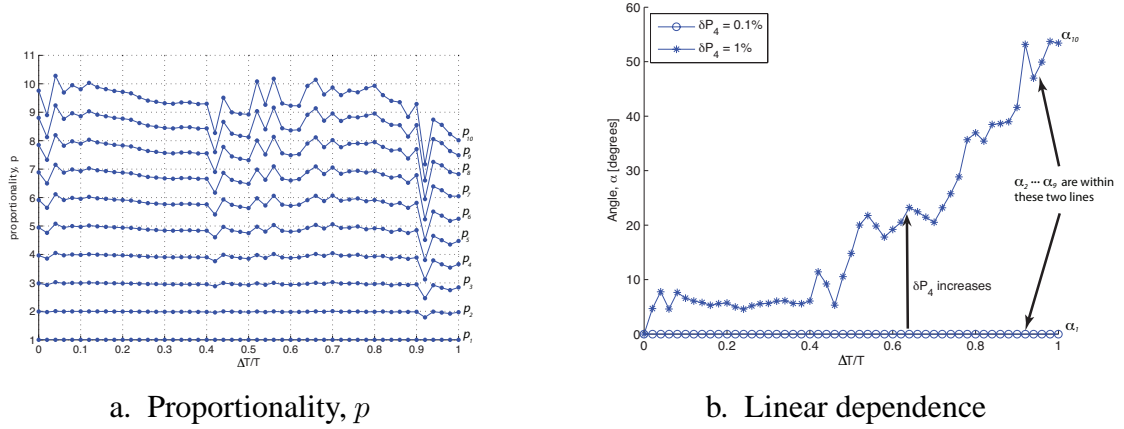
Figure 2.8: The linearity of SVFs for various levels of parameter variation δP_4 is demonstrated in two figures in terms of proportionality and angles between the baseline and the other parameter variations. The increase of p_j is not linear and α_j are becoming much larger than zero as j increases. This indicates that the SVFs are varying nonlinearly with respect to the parameter variation δP_4.

single parameter variation δP_i $(i = 1, \cdots, 5)$ as

$$p_j \equiv \frac{\|\mathbf{s}_{i,j}\|_2}{\|\mathbf{s}_{i,1}\|_2} \quad (j = 1, \cdots, 10),$$

$$\alpha_j \equiv \text{angle between } \mathbf{s}_{i,1} \text{ and } \mathbf{s}_{i,j}$$

$$= \cos^{-1} \frac{\mathbf{s}_{i,1} \cdot \mathbf{s}_{i,j}}{\|\mathbf{s}_{i,1}\| \, \|\mathbf{s}_{i,j}\|}$$

where

$$\mathbf{s}_{i,j} = \text{SVF for a variation in } \delta P_j \text{ of magnitude } j \cdot \delta P_{i,b},$$

$$\delta P_{i,b} = \text{parameter variation of parameter } P_i \text{ for the baseline SVF},$$

$$\mathbf{s}_{i,1} = \text{baseline SVF}.$$

Note that α_j is the angle between two higher-dimensional vectors as defined above. Hence, this angle is a measure of linear independence. When the angle is zero, the two vectors are proportional to each other, while when the angle is close to $90°$ or $270°$, the two vectors

are almost perpendicular to each other. Thus, the condition for ideal linearity is as follows,

$$p_j = j,$$

$$\alpha_j = 0°.$$

As an example, the proportionality and angle for the sensitivity vector fields of P_5 are shown in FIG. 2.7. As the variation level increases, the SVFs have amplitudes which increase linearly with δP_5. This linear increase is indicated by the magnitudes (2-norms) of the SVFs and their small angles with respect to the SVF for the baseline variation $\delta P_{5,b}$. In contrast to the SVFs for P_5, the SVFs for P_4 exhibit a weakly nonlinear variation with respect to the magnitude of parameter variation. For P_4, as the variation level increases, the SVF amplitudes increase nonlinearly, and the direction of the SVFs change. That is demonstrated in FIG. 2.8 for P_4.

2.3.5 Filtering of Sample Points

An important information one may require from the parameter reconstruction is the variation of P_4, which is the tip-sample distance Z. The ability to accurately detect the tip-sample distance while simultaneously monitoring other AFM parameters is an important advantage of the SVF approach for the general operation of atomic force microscopes. Simultaneously identifying multiple parameter variations is much easier when the nonlinearity of the SVFs for P_4 is minimized. To that aim, a novel point filtering is applied to the samples used in the SVF. Consider the SVFs for P_4. From FIG. 2.8, the sample points are selected so that the filtered sample points have the value of $\frac{\|\mathbf{s}_{4,10}\|_2}{\|\mathbf{s}_{4,1}\|_2}$ in the range from 9.7 to 10.3. A total of 157 sample points are selected when filtered with the delay time ΔT from 0 to 0.68 T, where T is the period of base excitation. Similarly, 121 sample points are selected with ΔT from 0 to 0.7 T. The first set of 157 filtered sample points are chosen for parameter reconstruction hereafter. The filtered sample points from the initial set of
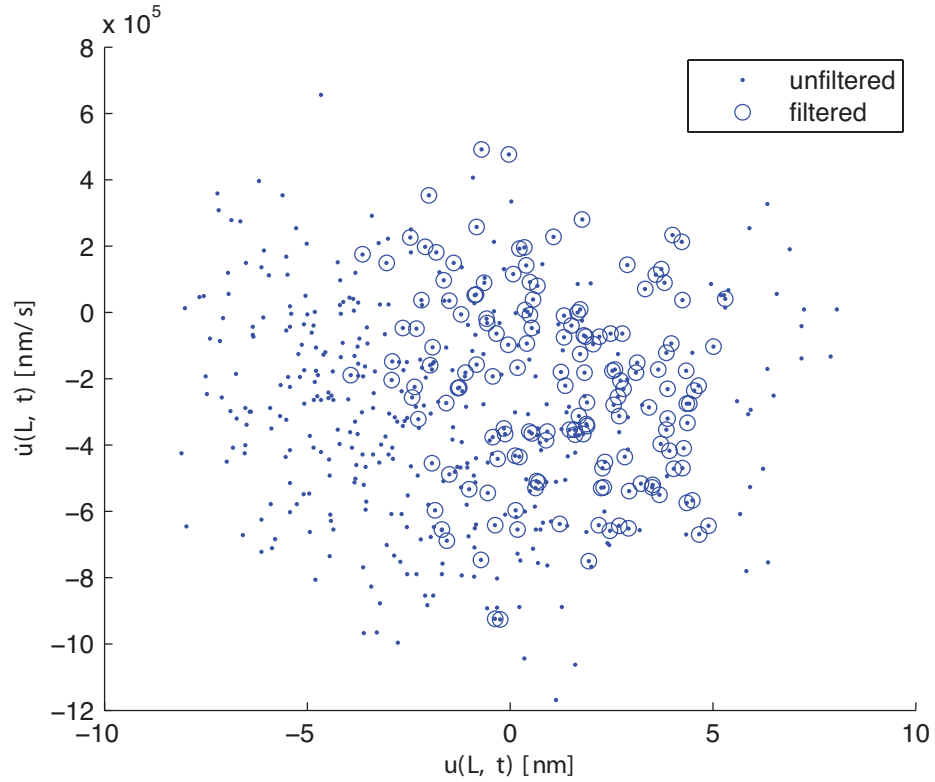
Figure 2.9: To alleviate the undesired strong nonlinearity of the SVFs for some parameter variations (especially for δP_4, which is the tip-sample distance), the sample points are selected so that the filtered sample points have the value of p_{10} for δP_4 in the range from 9.7 to 10.3. A total of 157 sample points are selected from the initial 500 sample points when filtered with the delay time ΔT from 0 to $0.68\,T$, where T is the period of base excitation.

sample points are shown in FIG. 2.9. After filtering, the SVFs for P_4 exhibit linearity, similar to the SVFs for P_5. As an example, the SVFs of P_4 from the filtered sample points are shown in FIG. 2.10.

One can still observe a weak nonlinearity in the SVFs, which leads to increasing relative errors as the parameter variation level increases, as presented in Tab. 2.2. A correction factor to account for this weak nonlinearity of the SVFs for P_4 is introduced in Section 2.3.7 below.

a. Proportionality, p　　　　　　　　b. Linear dependence
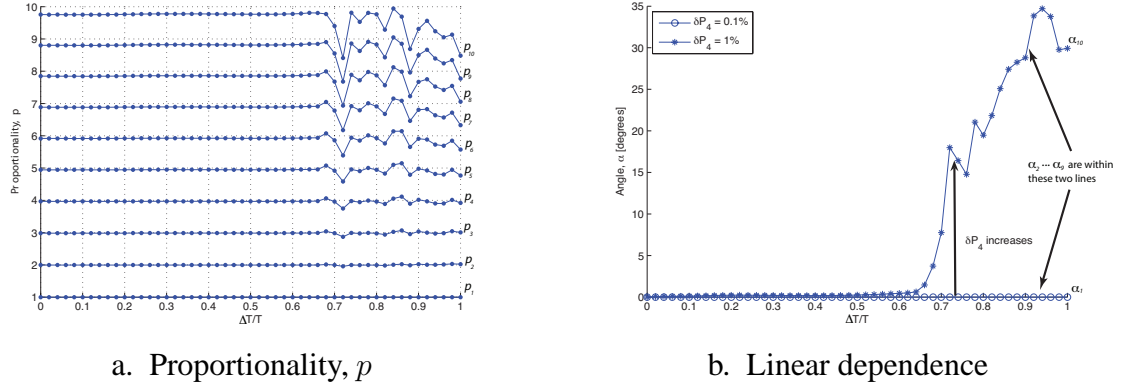
Figure 2.10: The linearity of SVFs for various levels of parameter variation δP_4 after filtering shows that the strong nonlinearity has been removed. A weak nonlinearity, however, is still observed. This weak nonlinearity leads to increasing relative errors as the parameter variation level increases.

2.3.6　Parameter Identifiability by the SVF Approach

After increasing the baseline variation level to reach a higher sensitivity, and after filtering the sample points, δP_1 and δP_2 cannot be reconstructed by the SVF approach. The reasons for the failure are discussed next. One of the unintended consequences of filtering is a reduction in the magnitude of certain SVFs. FIG. 2.11 shows that the SVFs for P_1 decreases significantly. This loss of the sensitivity makes it very difficult to detect the variation of P_1 simultaneously with other parameters which have much higher sensitivities. The SVFs of P_2, however, still have acceptable sensitivity after filtering.

Another unintended consequence of filtering is a change in the direction of the SVFs. The change in directions may lead to linearly dependent SVFs for distinct parameters. Linear dependence (collinearity) of two parameters are checked by comparing the angles between their SVFs. Consider for example the SVFs for P_2 and P_4. FIG. 2.12 shows that those SVFs become almost linearly dependent after filtering. The linear dependence of these SVFs makes it impossible to reconstruct both parameters P_2 and P_4 simultaneously. Due to the loss of the sensitivity and the linear dependence of distinct SVFs, P_1 and P_2 are
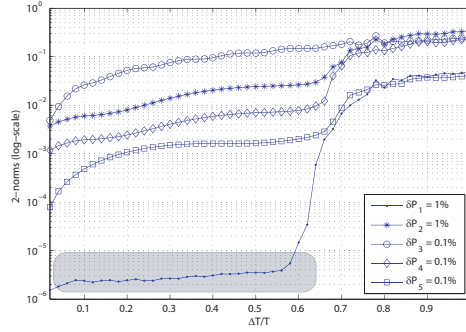
Figure 2.11: One of the unintended consequences of sample points filtering is a reduction in the magnitude (2-norm) of certain SVFs. The figure shows that the 2-norm of SVFs for P_1 decreases significantly. This loss of sensitivity makes it very difficult to detect the variation of P_1 simultaneously with other parameters which have much higher sensitivities. The SVFs of P_2, however, still have acceptable magnitude (sensitivity) after filtering.

eliminated from the parameter reconstruction.

2.3.7 Correction Factor for Weak Nonlinearity

To resolve the weak nonlinearity of the SVFs for P_4 as shown in FIG. 2.10 and Tab. 2.2, a correction factor is introduced. The parameter reconstruction is generally achieved under the assumption that higher order terms in Eq. (2.17) are negligible, so that the SVF $\mathbf{s}_{i,\delta P_i}$ (for a magnitude δP_i of variation for P_i) depends linearly on δP_i. Note that $\mathbf{s}_{i,\delta P_i}$ refers to a general value for δP_i, which is not necessarily $j \cdot \delta P_{i,b}$. Hence, the notation $\mathbf{s}_{i,\delta P_i}$ is

Variation	Normalization	Relative Error [%]	f_c
0.002	1.9947	-0.2634	-2.6274
0.003	2.9842	-0.5256	-2.6211
0.004	3.9685	-0.7865	-2.6148
0.005	4.9477	-1.0461	-2.6085
0.006	5.9217	-1.3045	-2.6022
0.007	6.8907	-1.5616	-2.5960
0.008	7.8546	-1.8715	-2.5898
0.009	8.8135	-2.0722	-2.5836
0.010	9.7674	-2.3257	-2.5774

Table 2.2: Weak nonlinearity of δP_4 and correction factor (f_c)

a. Before filtering   b. After filtering
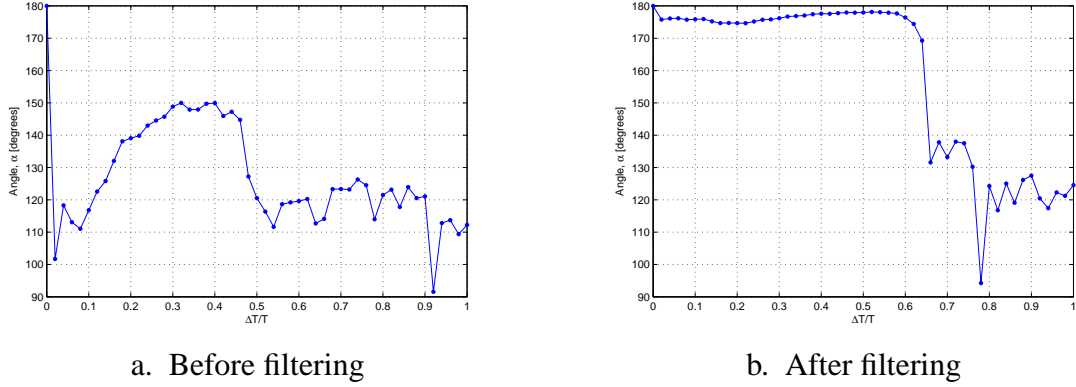
Figure 2.12: Another unintended consequence of sample points filtering is a change in the direction of the SVFs. The change in direction may lead to linearly dependent SVFs for distinct parameters. A linear dependence of δP_2 to δP_4 is revealed by the angle between the SVFs for P_2 and P_4. The figures show that those SVFs become almost linearly dependent after filtering. The linear dependence of these SVFs makes it impossible to reconstruct both parameters P_2 and P_4 simultaneously.

distinct from the previous notation $\mathbf{s}_{i,j}$. Also note that, when the parameter variation δP_i is at its baseline value $\delta P_{i,b}$, then the SVF is denoted by $\mathbf{s}_{i,1}$. The linearity ensures that

$$\|\mathbf{s}_{i,\delta P_i}\|_2 = \frac{\|\mathbf{s}_{i,1}\|_2}{\delta P_{i,b}}\delta P_i. \tag{2.19}$$

This assumption has to be modified for P_4. Considering the higher order effects of δP_4 on the corresponding SVFs, one obtains

$$\|\mathbf{s}_{i,\delta P_i}\|_2 = \frac{\|\mathbf{s}_{i,1}\|_2}{\delta P_{i,b}}(\delta P_i + f_c\delta P_i^2 + H.O.T). \tag{2.20}$$

The correction factor f_c in Eq. (2.20) is the dominant nonlinear term, and the higher order terms ($H.O.T.$) are neglected. Using Eq. (2.20), the corrected parameter variation δP_i can be expressed as

$$\delta P_{i,c} = \frac{2}{1 + \sqrt{1 + 4f_c\delta P_{i,o}}}\delta P_{i,o}, \tag{2.21}$$

where $\delta P_{i,c}$ is the corrected (actual) parameter variation, and $\delta P_{i,o}$ is the obtained parameter variation from the parameter reconstruction based on Eq. (2.19) under the assumption of linearity.

One can calculate the correction factor f_c from the test SVFs used for the linearity check by using an equation for f_c obtained from Eq. (2.20) and expressed as

$$\frac{\delta P'_{i,c} + f_c \delta P'^2_{i,c}}{\delta P_{i,c} + f_c \delta P^2_{i,c}} = \frac{\delta P'_{i,o}}{\delta P_{i,o}}, \tag{2.22}$$

where the parameter variations $\delta P_{i,c}$, and $\delta P_{i,o}$ are for the baseline variation of P_i, and the variations $\delta P'_{i,c}$, and $\delta P'_{i,o}$ are for the test variations of P_i. One value for f_c is obtained for each test case/variation. When calculating the correction factor for δP_4, the baseline variation is 0.1% and the test variations are in the range from 0.2% to 1%. The calculated correction factors are shown in the last column of Tab. 2.2. One can observe the small changes in f_c as the variation level increases. These small differences are likely due to the $H.O.T.$ from Eq. (2.20) which are ignored in the calculation of f_c. Nonetheless, the level of the differences in f_c is acceptable in the parameter reconstruction. The value of f_c from the variation level of 0.6% ($f_c = -2.6022$) is chosen for all the parameter reconstruction results in next section.

The correction factor suggested here is a calibration process for the SVF approach, but the number of measurements required for that is not very large. Herein, we used a large number of SVFs just to demonstrate that the correction factor is indeed approximately constant throughout the parameter range of interest. Note that the correction factor is mathematically derived from Eq. (2.22) as a direct consequence of the higher order terms affecting SVFs, and can be applied to the SVF approach for many nonlinear systems.

2.3.8 Parameter Reconstruction Results

Based on the analyses presented in the previous sections, parameters P_3, P_4 and P_5 were chosen for reconstruction by using the SVF approach. The results obtained were very accurate in the variation range from -1% to 1%. Two sample cases are presented in FIG. 2.13 and Tab. 3.3.

a. Case 1: δP_3 b. Case 1: δP_4 c. Case 1: δP_5

a. Case 2: δP_3 b. Case 2: δP_4 c. Case 2: δP_5
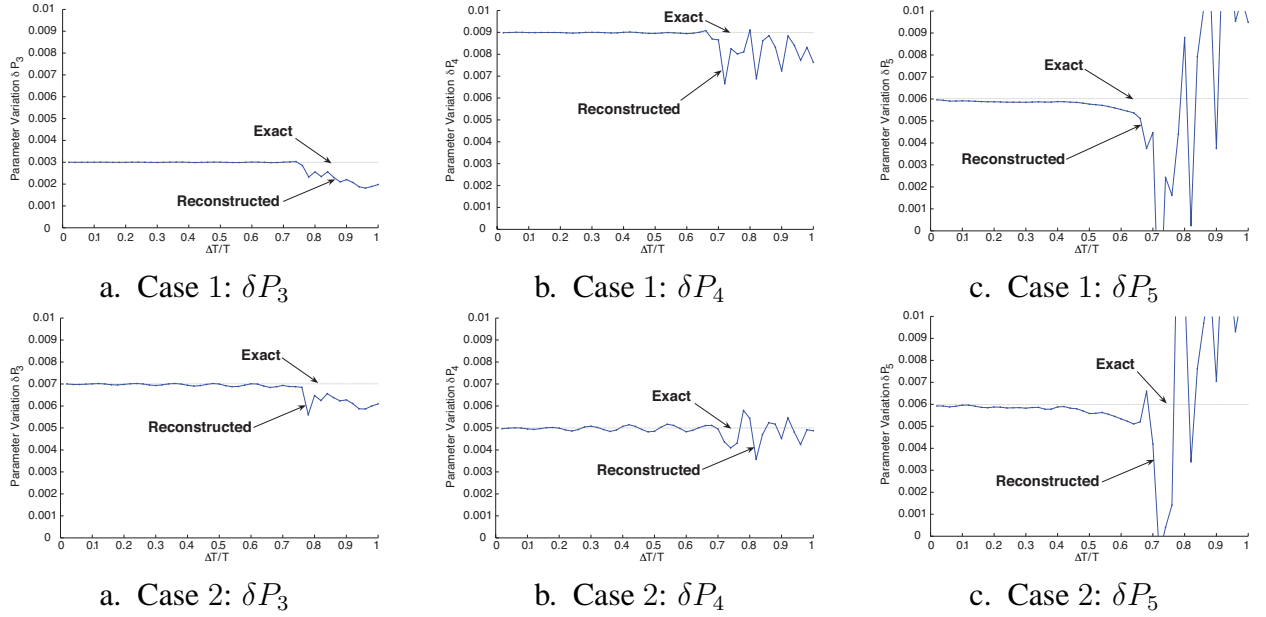
Figure 2.13: Parameters P_3, P_4 and P_5 were chosen for reconstruction by using the SVF approach. The results obtained are shown. These results are very accurate in the variation range from -1% to 1% with a delay time ΔT up to $0.5\ T$. Note that the SVF for P_5 has lower magnitude (2-norm) than the SVFs of the other parameters. Hence, the reconstruction results for δP_5 show larger relative errors than the other parameters.

As we noted previously, the SVFs for P_5 have lower magnitude than those of the other parameters. Hence, the reconstruction results for δP_5 show larger relative errors than the other parameters. FIG. 2.13 shows that the parameter reconstruction for all parameters is very accurate with a delay time ΔT up to $0.5\ T$. The parameter reconstruction results for $\Delta T = 0.2\ T$ are shown in Tab. 3.3. The maximum relative errors for the percentage variation and the physical variation are calculated in the range of ΔT from 0 to $0.5\ T$. Tab. 3.3 shows that the maximum physical relative error among all parameter variations is about 0.04% of δP_5, which is very small. As in FIG. 2.11, the sensitivity of the SVFs of P_3 is the largest. Tab. 3.3 also shows that the reconstruction performance for Case 1 is more robust than that for Case 2. This is likely because δP_4 in Case 1 is larger than δP_3, and that is consistent with the result shown in FIG. 2.11.

Case	δP	Relative Parameter Variation	Reconstruction Performed at $\Delta T = 0.2\,T$	Percentage Relative Error [%]	Max Percent Relative Error [%]	Max Physical Relative Error [%]
1	δP_3	0.003	0.002998	0.0672	0.3665	0.0011
	δP_4	0.009	0.008990	0.1210	0.5558	0.0050
	δP_5	0.006	0.005870	2.1681	3.9039	0.0234
2	δP_3	0.007	0.006981	0.2742	1.3657	0.0096
	δP_4	0.005	0.004990	0.2005	3.5514	0.0178
	δP_5	0.006	0.005876	2.0667	7.0141	0.0421

Table 2.3: Parameters reconstructed at $\Delta T = 0.2\,T$, and maximum relative errors calculated in range of $0 \leq \Delta T \leq 0.5\,T$, where ΔT is the delay time, and T is the period of the base excitation

2.4 Conclusions and Discussion

The major influence of the higher harmonics onto the tapping mode AFM dynamics has been discussed. For certain regimes, higher order modes have been shown to predict chaotic dynamics for the system although a single-mode approximation predicts limit cycle oscillations. These observations have been demonstrated and discussed along with the application of the sensitivity vector fields (SVFs) to the detection of multiple simultaneous parameter variations in the chaotic regime.

In the common tapping-mode AFM operation, the microcantilever is excited near a resonant frequency, and variations in the amplitude of the limit cycle experienced by the cantilever is measured to detect variations in the tip-sample displacement. For example, one may perform numerical simulations with an excitation frequency near the first resonant frequency of the cantilever (11.8 kHz) for Z=10 nm and separately for Z=10.01 nm (i.e. for a 0.1% variation in Z). The change in the amplitude of the limit cycle due to the 0.1% variation in Z is approximately 0.012 nm. Hence, the relative change in amplitude (ratio of the change in the amplitude versus the limit cycle amplitude) is approximately 0.0026. This quantity is much smaller than the relative sensitivity obtained using SVFs. However, the two sensitivities are hard to compare directly. Nonetheless, these results

suggest that it is generally more effective to measure the divergence of the trajectories in chaotic attractors than it is to measure variation in the amplitude of limit cycles. Also, note that the SVFs are formed based not only on displacements but also on velocities. Also, note that the main focus of this chapter is to demonstrate how to utilize chaotic dynamics of the AFM for sensing, and how to take advantages of chaotic attractors in terms of detection of multiple parameter variations.

Various issues regarding the implementation of the SVF approach for AFM and the methods to resolve those issues have been discussed. To achieve the most important property of the SVF approach, which is the linearity of the SVFs for single parameter variations, an approach of filtering sample points was introduced with a focus on the most important parameter (P_4). By filtering, one can generally ensure a satisfactory level of linearity for all parameters to be reconstructed. After filtering, the re-selection process is performed by investigating the SVFs for each single parameter variation. The possible significant loss of sensitivity and the possible linear dependence among distinct parameters have been discussed. Thus, certain parameters had to be eliminated from the reconstruction process.

A correction factor has been introduced to resolve the weak nonlinearity of the SVFs of certain parameter variations (e.g. δP_4). The correction factor has been calculated from test SVFs of known single parameter variations. The parameter variations identified using the correction factor have been shown to be very accurate.

The use of SVFs for AFM in tapping mode has been shown to result in an accurate parameter reconstruction. The operation of the atomic force microscope in a chaotic regime and by using a parameter reconstruction based on the SVF approach to the multi-mode microcantilever model has several advantages. First, one can avoid calibration efforts for searching the linear operation conditions. Second, the atomic force microscope can be op-

erated accurately with high sensitivity even when multiple parameter changes occur in the system. The third and most important advantage is that one can use the atomic force microscope to determine the tip-sample distance while simultaneously monitoring multiple parameters of the AFM microcantilever.

An important requirement for the proposed approach is the ability to collect/measure the SVF at sample locations. To do that it is not necessary for the initial conditions to be extremely close. That requirement can be eliminated, for example, by the use of point cloud averaging (PCA) approach [39, 98, 99]. The PCA approach has been demonstrated both numerically and experimentally. Using PCA for the AFM is possible. However, the focus of this paper is to demonstrate that SVFs can be used, are effective, and provide enhanced sensitivity and the ability to measure multiple parameters simultaneously. The next level of development of the approach is the use of PCA and, even beyond that, the use of embedded coordinates. Certainly, those are exciting topics which are part of future work. However, they are beyond the scope of this paper.

To use experimental data, one has to first decide if a model is available and is to be used or not. If a model is to be used, then the model is simulated, data is collected, and the attractor is computed. Next, samples are numerically collected for various parameter variation levels, and the linearity assumption is evaluated (and sample point filtering is applied).

If a model is not available or not to be used, then the prototype (or the device) is used to collect data. The attractor is measured using the actual experimental set-up. Then parameter variations are applied experimentally, and the deformed attractor is collected. The SVFs are estimated (using either data that include very close initial conditions, or using PCA). The linearity is estimated based on the measured SVFs. The measured samples are then filtered as described herein (note that the filter is applied at this calibration stage). The

end results are samples of the full SVFs. These SVF samples are for the locations (in the attractor) where the linearity is acceptable. Finally, after the calibration is performed, an actual parameter reconstruction (measurement) can be performed as follows. An attractor is collected for a system with unknown parameters. The collected data is used to determine the sensitivity vectors at the locations where the linearity assumption is acceptably satisfied and where SVFs have been measured.

Note that, if the parameter variations are larger than about 1% then the usual available measurement techniques should be used. The proposed approach provides much enhanced sensitivity, which is not needed when the parameter variations are large. Also, if multiple parameters exhibit nonlinear behavior, then the approach as described in the manuscript cannot be used for detecting multiple parameter variations simultaneously. A generalization of the approach is possible, but that is beyond the scope of this paper.

Also, note that the choice of ΔT can indeed be based on the linearity requirements (relative to P_5 for example). However, ΔT can also be chosen in relation to the parameter variations expected. These two aspects are connected. If parameter variations are small, a larger ΔT can be used because the linearity requirement is satisfied (for larger ΔT values).

CHAPTER III

Exploiting Delayed Nonlinear Feedback for Sensing Based on Bifurcation Morphing

3.1 Introduction

Vibration-based techniques have been essential tools for nondestructive system identification over 40 years. [16] Such system identification has been applied to a variety of problems such as sensing and damage detection. Early explorations focused on various linear vibratory properties for damage detection [17–24]. Recently nonlinear system analysis has become an important aspect of system identification approaches. For example, several studies showed that use of nonlinear properties of a system has a great potential for damage detection by providing an enhanced sensitivity. For instance, linear systems subject to chaotic excitation [25–28], and chaotic systems either with or without excitation [29–31] have been exploited. Also, a variety of attractor-based metrics have been presented to quantify geometric changes of attractors in state-space due to system parameter variations, e.g. damage. These approaches use Lyapunov exponents or attractor dimensions [32, 33], a scalar tracking metric [34, 35], and statistical characterization of the distribution of points in an attractor [30, 31, 36–38]. For further enhancement, pattern recognition techniques based on proper orthogonal decomposition of the shape changes between attractors (for undamaged and damaged systems) were proposed. These meth-

ods provide a basis for detecting multiple simultaneous damages and levels [30, 39, 40]. Furthermore, a novel approach has been proposed to enhance sensitivity by enhancing nonlinearity of linear or weakly nonlinear systems by means of nonlinear feedback excitations [41, 42].

Nonlinearities have been studied and were shown to be important in micro and nano scale vibration-based methods as well. For example, chaotic motions in tapping-mode atomic force microscopy (AFM) have been studied [43–46], and new operating algorithms using chaotic motions have also been discussed. These are based on sensitivity vector fields [44, 45] or local flow variations. [47] The increased use of AFM [1] also has been accompanied by rapid growth of various other cantilever-based sensing techniques. These techniques are usually monitoring either static (bending-mode) or dynamic (resonant-mode) responses of cantilever beams. Among resonant-mode approaches, nanomechanical resonant mass sensors have demonstrated remarkable sensitivity. [48–53] Monitoring resonant frequency is the most common approach in cantilever-based mass sensors, and continues to be studied for sensing increasingly smaller scale mass. For higher sensitivity, the use of higher order resonance modes and the reduction of device dimensions have been discussed. [54] Recent approaches have been developed to achieve attogram (10^{-18} g) level mass sensing, by using suspended micro-channel resonators [55], or integrated electronic displacement transducers [56]. While MEMS/NEMS sensors monitoring linear resonant frequencies continues to be studied, sensing techniques using nonlinear features have gained attention in various studies, such as ones focused on electrostatic nonlinear forcing [57], parametric resonances [58, 59], or nonlinear modal interactions. [60]

In this paper, several new studies of the novel concept of bifurcation morphing and nonlinear feedback excitation [42] are presented for practical applications in both damage detection and sensing. The primary discussion is focused on the time delay in the nonlinear

feedback excitation. This time delay is unavoidable in practical applications due to the delay caused by measuring the dynamics, calculating the nonlinear feedback, and forming the feedback loop. The side-effects of time delays include undesirable high sensitivity of the bifurcation boundary to small variations in the time delay. That is demonstrated by numerical simulation. To alleviate the effects of this side-effect, an additional time delay is introduced as a new design parameter. As the controllable time delay increases, the stable region surrounded by the bifurcation boundary converges to the smallest area. This convergence provides the great advantage of minimizing the effects caused by variability in the time delay. The increased time delay also helps to enhance sensitivity and robustness of the proposed approach.

Next, the paper discusses calibration issues. The sensing approach based on bifurcation morphing requires two bending-sensors to be placed at distinct locations on the beam and used to construct nonlinear feedback signals. Various sensor locations are tested to identify the ones which provide the highest sensitivity. By choosing various sensor locations, the proposed method can be adapted for detecting simultaneous damages at multiple locations. These features also enable sensing multiple analytes at multiple locations calibrated for ultra high sensitivity. A multi-mode clamped-free cantilever beam finite element model is used for computational analysis. Bending-sensors and uniformly distributed bending moments are used for applying the nonlinear feedback excitation. Density variations for multiple finite elements are considered as models for mass variations at certain locations. Parameter reconstructions are demonstrated for several test cases with high sensitivity to simultaneous mass variations at multiple locations.

Figure 3.1: Schematic of nonlinear feedback control.

3.2 Theory and Modeling

3.2.1 Bifurcation morphing with delayed nonlinear feedback excitation

A closed loop system for nonlinear feedback excitation consists of sensors, a controller, and an actuator. As shown in FIG. 3.1, the process of calculating feedback excitation (STEP2) may generate the majority of the time delay (t_1), while the time delay caused by the signal transfer from sensors to controller input (STEP1) and the signal transfer from controller output to actuator (STEP4) are much shorter and can be neglected. To exploit the boundary between stable and unstable dynamics for parameter identification, it is important to investigate the influence of the time delay on the bifurcation boundary. Note that an additional time delay t_2 can be applied by the controller (STEP3). The entire time delay is thus $\tau = t_1 + t_2$.

To gain an analytical perspective on the bifurcation morphing with delayed nonlinear feedback, one may start from the basic concept of bifurcation morphing method with non-
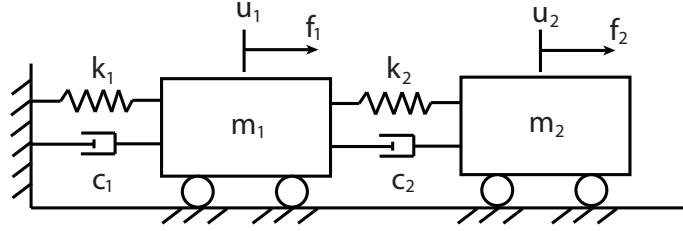
Figure 3.2: Two-degree-of-freedom spring-mass system subjected to nonlinear feedback excitation.

linear feedback presented by Yin et al. [42]. For the linear stability analysis, the nonlinear feedback term is ignored. The equation of motion for an m-DOF system can be expressed as

$$\mathbf{M\ddot{u}} + \mathbf{C\dot{u}} + \mathbf{Ku} = \mathbf{Gu}_d, \tag{3.1}$$

where matrices $\mathbf{M}$, $\mathbf{C}$, and $\mathbf{K}$ are the mass, damping, and stiffness matrices, $\mathbf{G}$ is the linear feedback gain matrix, $\mathbf{u}$ is the displacement vector, and $\mathbf{u}_d$ is the delayed displacement vector.

Two sensors are considered for feedback in the proposed approach. Thus, $\mathbf{G}$ is composed of two feedback gain parameters G_a and G_b. Eq. (3.1) can be solved for $\mathbf{u}$ by seeking a solution of the form

$$\mathbf{u} = \bar{\mathbf{u}}e^{\lambda t},$$

$$\mathbf{u}_d = \bar{\mathbf{u}}e^{\lambda t}e^{-\lambda \tau}, \tag{3.2}$$

where τ is time delay of the feedback excitation. Substituting Eq. (3.2) into Eq. (3.1), one obtains

$$\left[\lambda^2 \mathbf{M} + \lambda \mathbf{C} + \mathbf{K} - \mathbf{G}e^{-\lambda \tau}\right] \bar{\mathbf{u}} = 0. \tag{3.3}$$

For a non-trivial solution to exist, the matrix

$$\Lambda(\lambda) = \lambda^2 \mathbf{M} + \lambda \mathbf{C} + \mathbf{K} - \mathbf{G}e^{-\lambda \tau} \tag{3.4}$$

must be singular. Hence, the characteristic equation of the system is

$$det\left[\Lambda(\lambda)\right] = 0. \tag{3.5}$$

Bifurcation boundary of Hopf bifurcation on the G_a-G_b parameter space can be obtained by solving Eq. (3.6) for $\lambda = \pm j\omega$. One obtains

$$det\left[\Lambda(\pm j\omega)\right] = 0, \tag{3.6}$$

which consists of real and imaginary parts that must vanish. Hence,

$$Re\{det\left[\Lambda(\pm j\omega)\right]\} = 0,$$

$$Im\{det\left[\Lambda(\pm j\omega)\right]\} = 0. \tag{3.7}$$

Eq. (3.7) has 3 undetermined variables (G_a, G_b, ω). The frequency ω can be interpreted as the frequency of the limit cycle which appears right after the bifurcation occurs. As there are only two equations, and the goal is to obtain the bifurcation boundary in the parameter space (G_a, G_b), one can fix ω as various values and solve for the corresponding G_a and G_b. This can be done for increasing ω from $\omega = 0$ to higher frequency as needed.
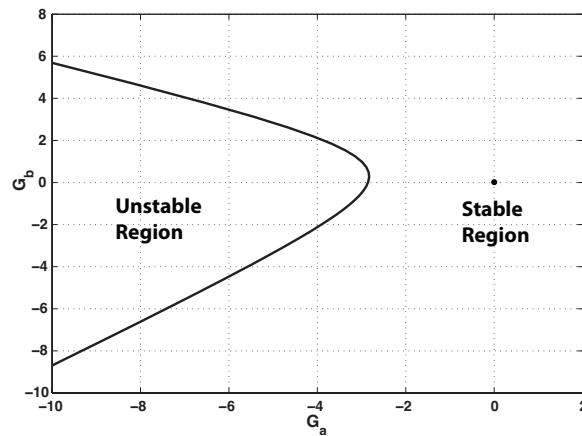
Figure 3.3: Bifurcation boundary without time delay.

a. shrinkage of the stable region

b. convergence of the stable region

c. upper region of the boundary

d. lower region of the boundary
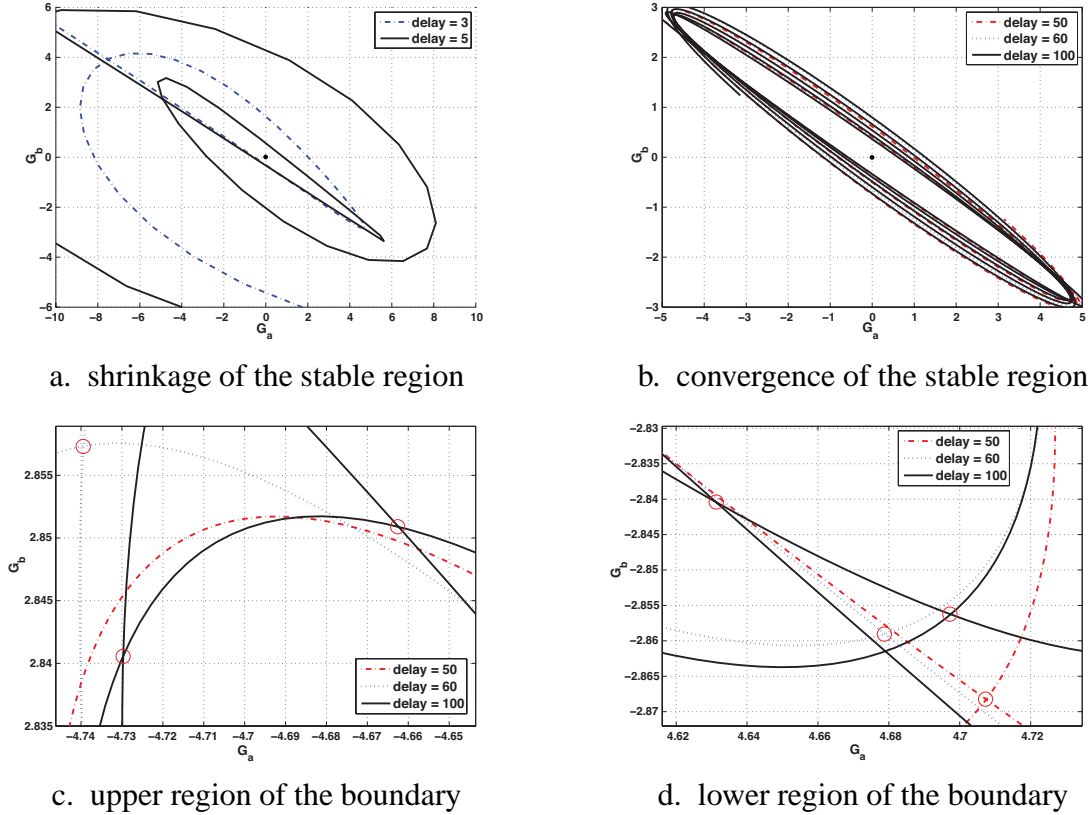
Figure 3.4: As time delays increase, the bifurcation boundary converges to a minimal area with increasing numbers of intersections.

To observe the influence of the time delay, consider the simple two-degree-of-freedom (2-DOF) mass-spring model from Yin et al. [42], as shown in FIG. 3.2. The equation of motion for this system is as same as Eq. (3.1), where

$$
\mathbf{M} = \begin{bmatrix} m_1 & 0 \\ 0 & m_2 \end{bmatrix}, \quad \mathbf{C} = \begin{bmatrix} c_1 + c_2 & -c_2 \\ -c_2 & c_2 \end{bmatrix}, \quad \mathbf{K} = \begin{bmatrix} k_1 + k_2 & -k_2 \\ -k_2 & k_2 \end{bmatrix},
$$

$$
\mathbf{G} = \begin{bmatrix} 0 & 0 \\ G_a & G_b \end{bmatrix}.
$$

The system parameters are $m_1 = m_2 = 1$, $c_1 = c_2 = 1$ and $k_1 = k_2 = 1$. Solving Eq. (3.7) for G_a and G_b at various ω, one obtains a curve in the parameter space. This curve divides the space into stable and unstable regions, as shown in Figs. 3.3 and 3.4 . Without time

delay ($\tau = 0$), G_a and G_b can be obtained as

$$
\begin{aligned}
G_a &= -\frac{\omega^4 + 2}{\omega^2}, \\
G_b &= \frac{-\omega^5 + \omega^3 + \omega}{\omega^3}.
\end{aligned}
\tag{3.8}
$$

FIG. 3.3 shows the bifurcation boundary formed by Eq. (3.8). Noting that $\lim_{\omega \to 0} G_b = \infty$, $\lim_{\omega \to \infty} G_b = -\infty$, and $\frac{\delta G_b}{\delta \omega} < 0$ for all ω, this boundary divides the parameter space into half-opened regions: an unstable region (left-hand side) and a stable region (right-hand side). This is obvious for the 2-DOF system because it only has one pair of roots for Eq. (3.6). Hence, every solution is a bifurcation point in the parameter space.

Applying time delay to the system ($\tau \neq 0$), there are now an infinite number of roots for Eq. (3.6), as the equation becomes transcendental. G_a and G_b are obtained as

$$
\begin{aligned}
G_a &= -\frac{\omega(\omega^4 + 2)\cos(\tau\omega) + (\omega^6 + 5\omega^2 - 2)\sin(\tau\omega)}{\omega^3}, \\
G_b &= \frac{(-\omega^5 + \omega^3 + \omega)\cos(\tau\omega) + (2\omega^4 + 2\omega^2 - 1)\sin(\tau\omega)}{\omega^3}
\end{aligned}
\tag{3.9}
$$

Every set of (G_a, G_b) does not physically represent a threshold between stable and unstable dynamics of the system anymore because a bifurcation occurs only if the corresponding roots are *the first pair* passing through the imaginary axis to right-hand side of the complex plane. As shown in Figs. 3.4a and 3.4b, a solution curve starts intersecting itself and forms a closed region including the origin. Note that the origin in the parameter space means no feedback excitation to the system, and the region including the origin is always stable. From FIG. 3.4a and FIG. 3.4b, the stable region of the system is observed to converge to the smallest area as the time delay increases. Figs. 3.4c and 3.4d show the uppermost and lowermost areas of FIG. 3.4b. An increasing number of intersections of the boundary are observed as the time delay increases.

As not all pairs (G_a, G_b) are on the bifurcation boundary, we consider polar coordinates in the parameter space. The bifurcation boundary can be defined for a given τ as a set of

a. polar coordinates of the boundary

b. convergence of r_{min} when $\theta = 0, \pi$
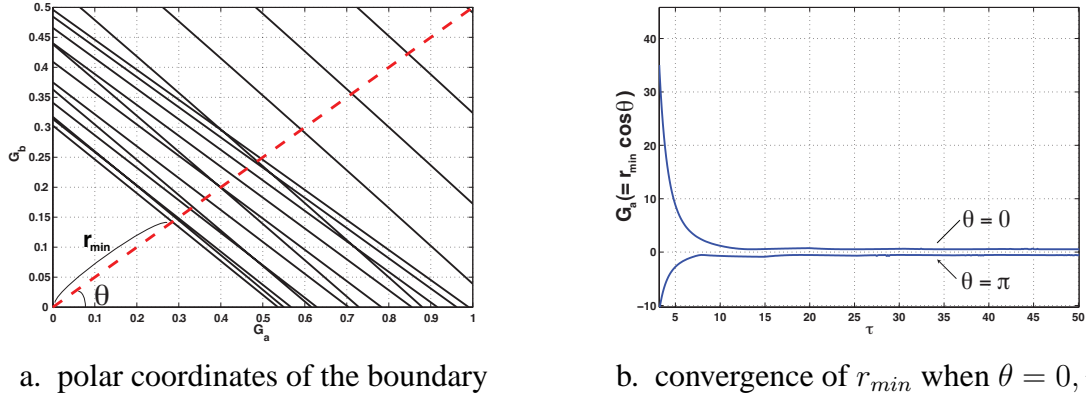
Figure 3.5: The bifurcation boundary can be defined in polar coordinates, and the convergence of the boundary can be demonstrated by the convergence of r_{min}

.

minimum radius (r_{min}) for all θ from 0 to 2π, as shown in FIG. 3.5a. FIG. 3.5b shows the convergence of r_{min} as the time delay increases, and $\theta = 0, \pi$ (i.e. $G_b = 0$ and r_{min} is the minimum of $|G_a|$). Another interesting phenomenon observed through the analytical calculations is that the frequency of the instability near the bifurcation boundary becomes less sensitive to parameter changes when the time delay increases. This phenomenon is also observed for the computational model and demonstrates that each boundary curve corresponds to a very narrow range of frequencies for the fully developed (or converged) bifurcation boundary.

3.2.2 Computational model for parameter reconstruction
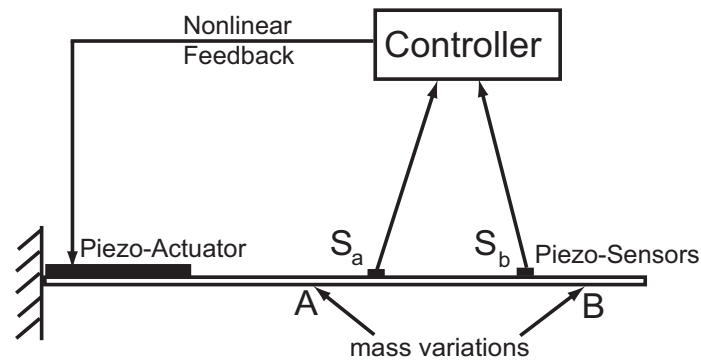
Figure 3.6: Schematic of the cantilever beam test system.

In this section we consider a closed loop system composed of a controller which acts on a clamped-free cantilever beam structure, as shown in FIG. 3.6. The cantilever beam, the actuator, and the sensors are modeled using a finite element formulation. In FIG. 3.7, a 2D elastic beam element is used for modeling. The output of each sensor is considered proportional to the bending of the finite element at the location of the sensor. The actuator is considered to create a uniformly distributed bending moment along its length (10 adjacent nodes). Mass variations are applied at multiple locations. An aluminum beam with physical properties given in Tab. 3.1 is considered. ANSYS is used to form the mass and stiffness matrices for a model with 100 BEAM3 elements. The equation of motion for the FEM structural model with nonlinear feedback excitation is expressed as

$$\mathbf{M}\ddot{\mathbf{u}} + \mathbf{C}\dot{\mathbf{u}} + \mathbf{K}\mathbf{u} = \mathbf{G}\mathbf{s} + \mathbf{N}\mathbf{p}_3(\mathbf{s}), \tag{3.10}$$

where matrices $\mathbf{M}$, $\mathbf{C}$, and $\mathbf{K}$ are mass, damping, and stiffness matrices, $\mathbf{G}$ and $\mathbf{N}$ are linear and nonlinear feedback gain matrices, $\mathbf{u}$ is the vector of nodal displacements and rotations, and $\mathbf{s}$ is the vector of sensor outputs. The vector $\mathbf{p}_3(\mathbf{s})$ contains the entries of $\mathbf{s}$ each raised to power 3. Two sensors (placed at distinct locations) are used. Thus, $\mathbf{s}$ is a 2×1 vector expressed as

$$\mathbf{s} = \begin{Bmatrix} s_a & s_b \end{Bmatrix}^T = \begin{Bmatrix} -r_{a1} + r_{a2} & -r_{b1} + r_{b2} \end{Bmatrix}^T, \tag{3.11}$$

where r_1 and r_2 are the rotations of the 2 nodes on an element as shown in FIG. 3.7, and $\mathbf{p}_3(\mathbf{s}) = \begin{Bmatrix} s_a^3 & s_b^3 \end{Bmatrix}^T$. Subscripts a and b indicate the element index among the 100 elements which represent all the possible sensor locations. The vector $\mathbf{s}$ can be expressed in terms of $\mathbf{u}$ as follows

$$\mathbf{s} = \mathbf{E}\mathbf{u}, \tag{3.12}$$

where $\mathbf{E}$ is given by

$$\mathbf{E} = \begin{bmatrix} 0 & \cdots & 0 & 0 & -1 & 0 & 0 & 1 & \cdots & \cdots & \cdots & \cdots & \cdots & \cdots & \cdots & \cdots & 0 \\ 0 & \cdots & \cdots & \cdots & \cdots & \cdots & \cdots & \cdots & 0 & 0 & -1 & 0 & 0 & 1 & \cdots & 0 \end{bmatrix},$$

and $\mathbf{u}$ is expressed as

$$\mathbf{u} = \{ \begin{array}{ccccccccccccccc} x_{11} & \cdots & x_{a1} & y_{a1} & r_{a1} & x_{a2} & y_{a2} & r_{a2} & \cdots & x_{b1} & y_{b1} & r_{b1} & x_{b2} & y_{b2} & r_{b2} & \cdots & r_{n2} \end{array} \}^T.$$

The first subscript indicates element number, and the second subscript denotes the node number for each element.
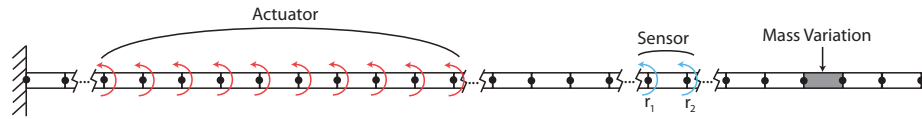
Figure 3.7: Cantilever beam model with actuator and sensors.

Table 3.1: Properties of the cantilever beam

Property	Symbol	Value
Length	L	$0.28\ m$
Width	b	$0.03\ m$
Height	h	$1.27 \cdot 10^{-3}\ m$
Young's Modulus	E	$69.9\ GPa$
Poisson Ratio	μ	0.33
Density	ρ	$2660\ kg/m^3$

Considering time delay in feedback excitation and the expression of delayed sensor output $\mathbf{s}_d$ in terms of $\mathbf{E}$ and $\mathbf{u}_d$, the final equation of motion for delayed nonlinear feedback is expressed as

$$\mathbf{M\ddot{u} + C\dot{u} + Ku = GEu}_d + \mathbf{Np}_3\left(\mathbf{Eu}_d\right). \tag{3.13}$$

Once the equations of motion for the discretized system are obtained, the model can be reduced by general modal analysis. Calculating the $n \times m$ normalized eigenmatrix $\mathbf{V}_m$

composed of eigenvectors of the system, and introducing the modal coordinate vector $\mathbf{x}$, vectors $\mathbf{u}$ and $\mathbf{u}_d$ can be expressed as

$$\mathbf{u} = \mathbf{V}_m\mathbf{x},$$

$$\mathbf{u}_d = \mathbf{V}_m\mathbf{x}_d. \tag{3.14}$$

Substituting $\mathbf{x}$ into Eq. (3.13) and multiplying by $\mathbf{V}_m^T$ one obtains

$$\mathbf{V}_m^T \quad \mathbf{M}\mathbf{V}_m\ddot{\mathbf{x}} + \mathbf{V}_m^T\mathbf{C}\mathbf{V}_m\dot{\mathbf{x}} + \mathbf{V}_m^T\mathbf{K}\mathbf{V}_m\mathbf{x}$$

$$= \mathbf{V}_m^T\mathbf{G}\mathbf{E}\mathbf{V}_m\mathbf{x}_d + \mathbf{V}_m^T\mathbf{N}\mathbf{p}_3\left(\mathbf{E}\mathbf{V}_m\mathbf{x}_d\right). \tag{3.15}$$

A final m-DOF reduced order model is obtained as

$$\mathbf{I}\ddot{\mathbf{x}} + \mathbf{D}\dot{\mathbf{x}} + \mathbf{\Omega}\mathbf{x} = \mathbf{G}_r\mathbf{x}_d + \mathbf{N}_r\mathbf{p}_3\left(\mathbf{E}_r\mathbf{x}_d\right), \tag{3.16}$$

where $\mathbf{I}$ is the identity matrix, $\mathbf{D}$ is a diagonal matrix with diagonal values of $2\omega_i\zeta_i$ and $\mathbf{\Omega}$ is a diagonal matrix with diagonal values of ω_i^2. For numerical simulations, ζ_i are assumed to all have a value of 0.1.

3.3   Results

3.3.1   Bifurcation boundary with delayed nonlinear feedback

Although challenging, it is possible to obtain the bifurcation boundary for the cantilever model with delayed nonlinear feedback by an analytical approach. In addition, the bifurcation boundary can be identified by numerically constructing bifurcation diagrams for multiple locations in the parameter space. Results obtained for both the analytical and the numerical methods are shown in FIG. 3.8 for the special case of zero delays. Points A, B and C correspond to parameter values (G_a, G_b) shown, whereas the frequency of the dynamics in the post bifurcation regime is indicated by f. The results given by the two methods match very well. All results below are based on numerical simulations.

a. bifurcation points (analytical)　　　b. bifurcation points (numerical)
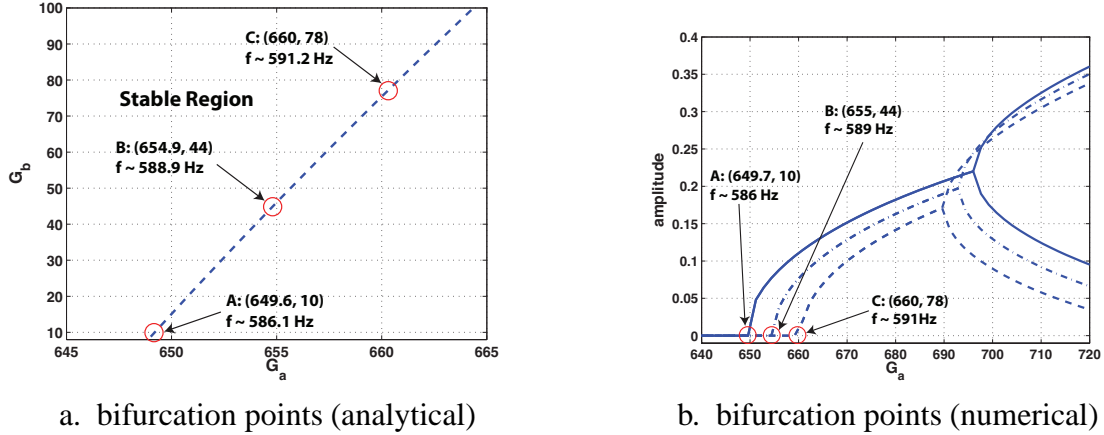
Figure 3.8: Bifurcation points obtained using analytical and numerical methods for cantilever beam model with non-delayed nonlinear feedback excitation. For delayed nonlinear feedback excitation, only the numerical method is used.

In the bifurcation morphing approach choosing sensor locations S_a and S_b is important, not unlike other methods. Thus, twenty combinations of two sensors were tested with sensors at five different locations on the beam to obtain better sensitivity to variations in mass at a few designated locations. The selected combination of two sensors (S_a and S_b) corresponds to the finite elements located around 60% and 80% of the beam length from its clamped end. The nonlinear feedback gains were fixed during simulations, as $N_a = N_b = -0.05$. Bifurcation boundaries in the G_a-G_b parameter space were obtained for increasing time delays from near zero to 50 ms. As time delays increase, the stable region converges to the smallest area in the parameter space, as shown in FIG. 3.9. Dotted lines are the bifurcation boundaries for time delays from 0.1 ms to 0.5 ms. The lines with roman labels are final bifurcation boundaries for the supercritical Hopf bifurcations which occurs when the time delay is 50 ms. Circles indicate intersections of two different boundary curves distinguished by the difference in frequency in the post-bifurcation regime. These frequencies can be compared with those for the final boundaries. The dotted line corresponding to $\tau = 0.4$ ms is the closest to the boundary VIII. The frequencies for this (dotted) boundary range from 1485 Hz to 1490 Hz. The boundary VIII has frequencies
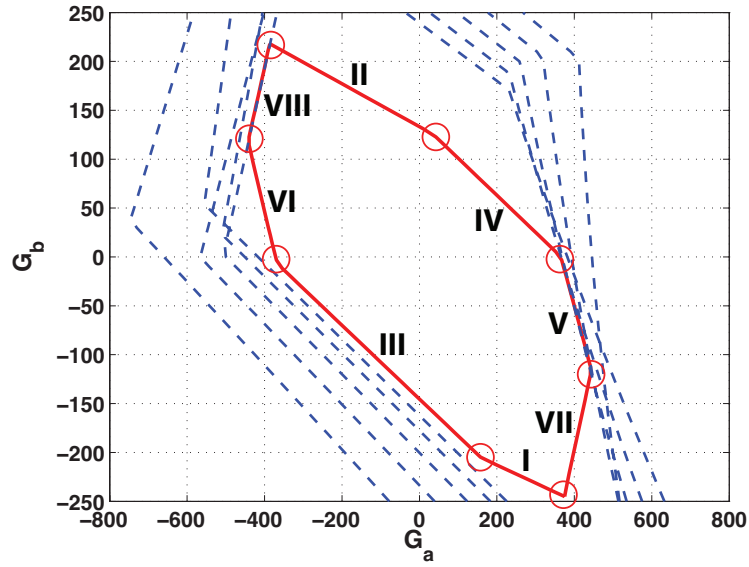
Figure 3.9: As time delays increase, the stable region converges to the minimal area with multiple intersections of the boundaries.

from 1491 Hz to 1492 Hz. On the boundary V, closest lines at $\tau = 0.4$ ms $\tau = 0.5$ ms have frequency ranges of $931 \sim 943$ Hz and $910 \sim 921$ Hz respectively, while the final boundary has frequency range only in $928 \sim 929$ Hz. Hence, the whole bifurcation boundary consists of multiple boundary curves divided by intersections, which have distinct frequency characteristics. Multiple boundary curves can be monitored for parameter reconstruction and are effective for detection of simultaneous mass variations on multiple locations, as demonstrated in the next section.

Next, consider a constant $G_b = -162.5$. One point on the boundary VII can then be monitored in detail to evaluate the effects of the time delay. As shown in FIG. 3.10a, the value of G_a (at the bifurcation point) fluctuates (with large variations) and converges to the minimum value of G_a as the time delay increases. This behavior suggests that a smaller stable region is beneficial because the searching process for detecting the bifurcation boundary starts from the origin of the parameter space. Moreover, an important

a. convergence of G_a to minimum   b. decrease of noise by time delay variation
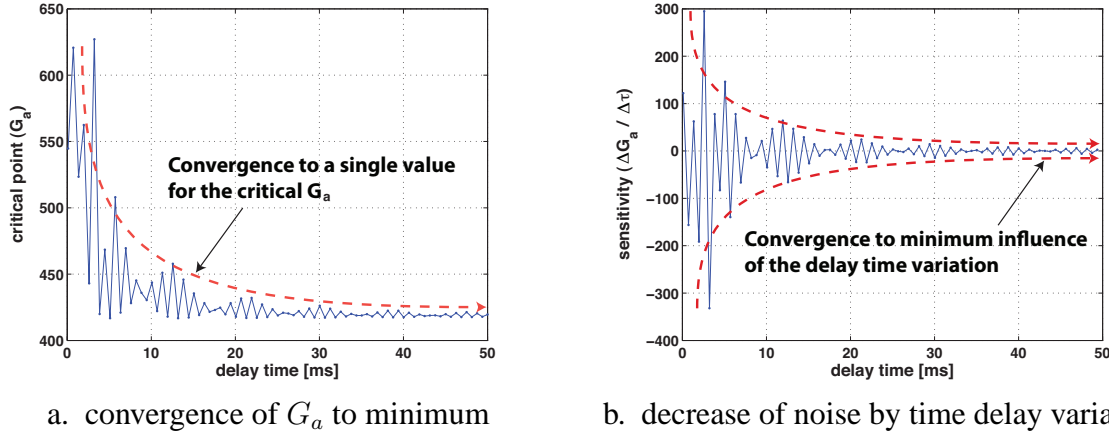
Figure 3.10: As time delay increases, the values on the bifurcation boundary converges to the minimum. Furthermore, the noise caused by time delay variation is minimized.

advantage comes from the fact that G_a converges to a certain value. The large fluctuation of G_a obtained for shorter time delays in FIG. 3.10a are undesirable because small errors in the controlled time delay may result in unintended but substantial variations in the bifurcation boundary. As in FIG. 3.10b, the convergence of G_a is essential to reduce the influence of errors in controlling the time delay. In this figure, $\frac{\Delta G_a}{\Delta \tau}$ is shown to converge to nearly zero as the time delay increases. Additional time delay reduces undesirable sensitivity of the system to errors in the controller, and it helps maintain performance in terms of sensitivity and proportionality to mass variations which are essential for parameter reconstruction. In FIG. 3.11, proportionality is represented by a normalized value. A value of 1 indicates good proportionality within monitored range. Mass variations are applied within a range from 0.05% to 0.2% of the total mass of the beam. Sensitivity can be defined as a nondimensional quantity given by

$$S_m^G = \frac{\frac{\Delta G}{G}}{\frac{\Delta m}{m}}, \tag{3.17}$$

where m is the total beam mass, Δm is the mass variation and G is a feedback gain on the bifurcation boundary. Similar to Eq. (3.17), one may define the sensitivity of the natural
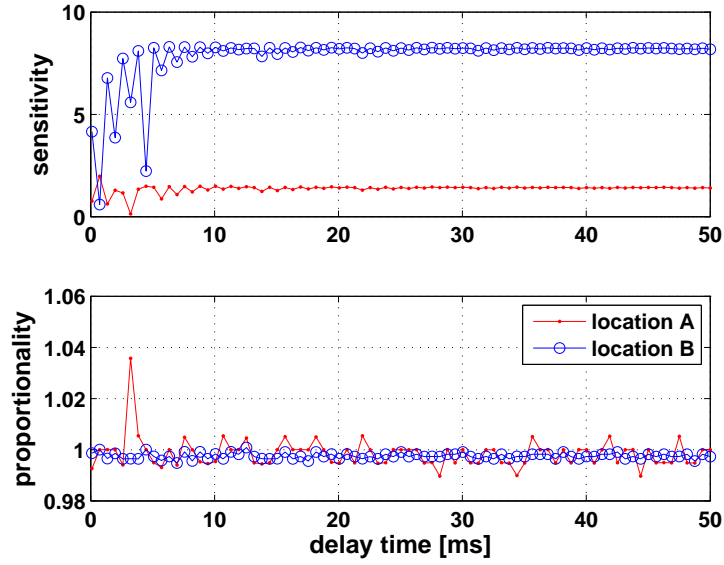
Figure 3.11: Additional time delay eliminates disadvantages caused by natural time delay, it maintains the performance of the proposed approach in terms of sensitivity

frequency shift as

$$S_m^\omega = \frac{\frac{\Delta\omega}{\omega}}{\frac{\Delta m}{m}}, \tag{3.18}$$

where ω is a natural frequency of the beam. A maximum S_m^G of 1.43 is obtained for Δm at location A, and 8.25 for Δm at location B, as shown in FIG. 3.11. Locations A and B correspond to the finite elements located around 30% and 90% of the beam length from its clamped end. For same mass variations, the maximum value of S_m^ω among the first 5 lowest natural frequencies (up to 1.6 kHz) is 1.462 at the first natural frequency (28.2 Hz) for Δm at location B. Overall, the bifurcation morphing is observed to have sensitivities starting from about the same order as frequency shifts to one order of magnitude higher.

Nondimensional values have been used to compare the sensitivities. Nonetheless, there are other aspects of the proposed bifurcation morphing approach which differentiate it from the more common, frequency shift methods. For example, frequency shift methods usually require very low damping (high quality factor) especially in the lower frequency
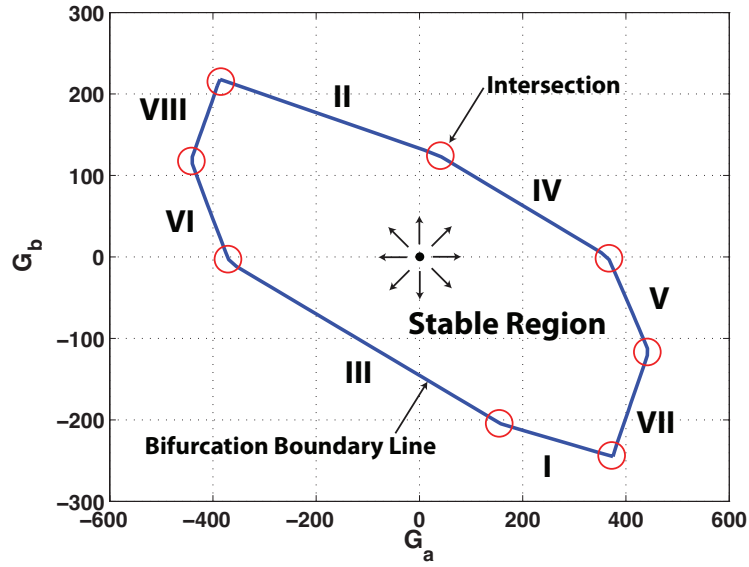
Figure 3.12: Bifurcation boundary with $\tau = 50$ ms

Table 3.2: Frequency Characteristics of the bifurcation boundary curves

Index	Frequency of Limit Cycle [Hz]
I	$153 \sim 154$
II	$168 \sim 169$
III	$451 \sim 452$
IV	$469 \sim 470$
V	$928 \sim 929$
VI	$946 \sim 947$
VII	$1472 \sim 1473$
VIII	$1491 \sim 1492$

range, while limit cycle oscillations (beyond the bifurcation point) are much less dependent on damping regardless of their frequency. Furthermore, the values of the gains (G_a, G_b) are applied to the system, and hence are known with higher resolution than resonant frequencies which have to be measured.

3.3.2 Parameter Reconstruction

The bifurcation boundary for parameter reconstruction is obtained for a time delay of 50 ms, as shown in FIG. 3.12. Each boundary curve is numbered in increasing order by

the frequency of the post bifurcation regime. As presented in Tab. 3.2, narrow ranges of frequencies are observed for all bifurcation boundaries. The boundary curves V and VII are used to apply the bifurcation morphing method and detect simultaneous mass variations at multiple locations. Mass variations are applied at two distinct locations, A and B. A 5% variation of the mass of a single finite element is applied to construct the basis for parameter reconstruction. Also, 10%, 15% and 20% variations of the mass of a single finite element are applied to demonstrate the proportionality of the basis. From the physical properties assumed for the cantilever beam (Tab. 3.1), the total beam mass is 28.4 g, and each finite element has a mass of 284 mg. Hence the range of mass variations are approximately from 14 mg to 56 mg, which are 0.05% $\sim$ 0.2% variations compared to the total mass of the beam.

a. Δm at location A   b. Δm at location B
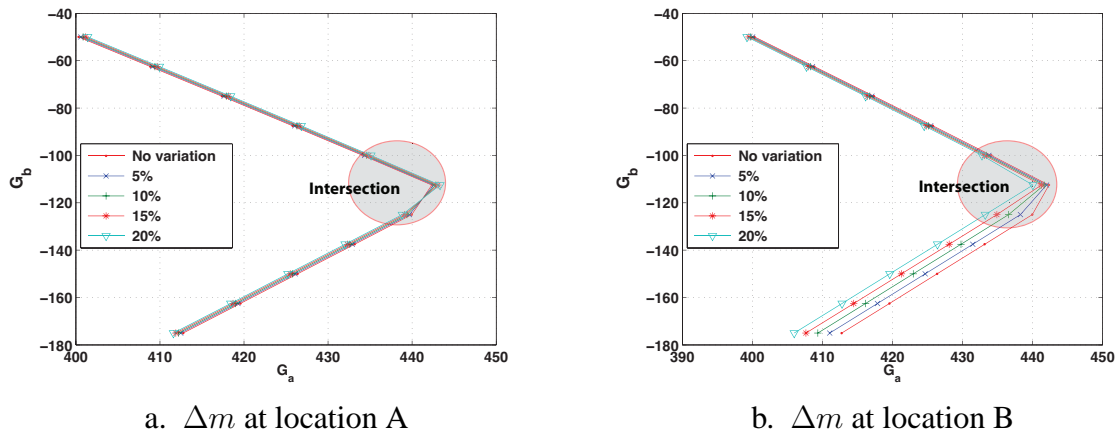
Figure 3.13: Bifurcation boundary morphing by mass variations on a single location.

The bifurcation morphing in the parameter space caused by a single mass variation is shown in FIG. 3.13. The circle indicates an area which is near the intersection between the bifurcation boundary curves V and VII. In this intersection area, the bifurcation morphing is not proportional to the mass variations because the two boundary curves overlap each other as mass changes. Excluding the intersection region, variations of the bifurcation points are measured at four locations along each of the two boundary curves, which leads

to a total of eight points. As demonstrated in FIG. 3.13, there are many portions of the bifurcation boundary which can be probed in detail. However, that is beyond the scope of this paper. Here, we choose to focus on one portion of the boundary. This portion was chosen in a quasi ad-hoc fashion. Of course, an optimized selection process can be designed.

The bifurcation morphing modes are presented by plotting the variation of G_a (on the y-axis) versus G_b (on the x-axis), as shown in Figs. 3.14a and 3.14b. In these figures, the left side of the intersection region is the boundary curve VII and the right side is the boundary curve V. Mass variations are applied at location A in FIG. 3.14a and location B in FIG. 3.14b. A mass variation of 5% is used to construct the basis for reconstruction of mass variations at each location. These figures show that each boundary curve varies in a way which makes it hard to detect simultaneous mass variations using only a single boundary curve. Nonetheless, each boundary curve (with distinct frequency characteristics) varies differently for the same mass variation, and linearly independent bases for distinct locations can be constructed by using a combination of two or more boundary curves.

The proportionality of each basis to mass variations is demonstrated in Figs 3.14c and 3.14d. The amount of morphing of the bifurcation boundary was obtained for 5%, 10%, 15% and 20% mass variation. Next the linearity of this morphing can be compared (as a ratio) to the baseline variation of 5%. The ratio which is obtained for a perfect linearity is of 1 for 5%, 2 for 10%, 3 for 15% and 4 for 20%. The results in Figs 3.14c and 3.14d show that proportionality is ensured for the eight points forming the basis, while some points in the intersection region fail to maintain proportionality.

Parameter reconstruction is demonstrated for five different cases of simultaneous mass variations. The 8×2 basis matrix $\mathbf{B}$ is formed by two 8×1 basis vectors, $\mathbf{b}_A$ for location

a. Mass at location A

b. Mass at location B

c. Mass at location A

d. Mass at location B
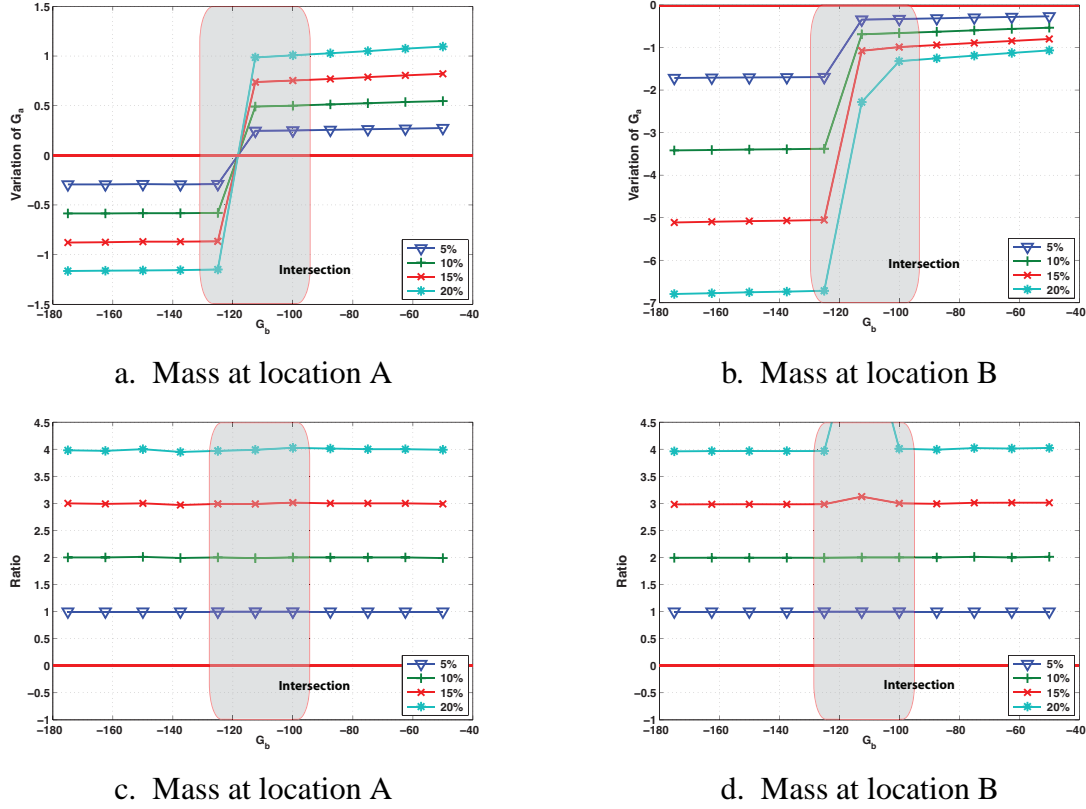
Figure 3.14: Bifurcation morphing modes and proportionality of the basis within desired range of mass variations.

A and $\mathbf{b}_B$ for location B as

$$\mathbf{B} = \begin{bmatrix} \mathbf{b}_A & \mathbf{b}_B \end{bmatrix}. \tag{3.19}$$

Then, the equation used to reconstruct (identify) the mass variation can be expressed as

$$\mathbf{B}\Delta\mathbf{m} = \mathbf{c}_i, \tag{3.20}$$

where $\Delta\mathbf{m}$ is the $2{\times}1$ vector of mass variations at location A and B, $\Delta\mathbf{m} = \{\Delta m_A \quad \Delta m_B\}^T$, and $\mathbf{c}_i$ is the 8×1 vector of bifurcation morphing mode for the test cases from FIG. 3.15 (details in Tab. 3.3). The amount of mass variation can be identified by solving the overdetermined system of equations in Eq. (3.20) simply as

$$\Delta\mathbf{m} = \mathbf{B}^{+}\mathbf{c}_i. \tag{3.21}$$
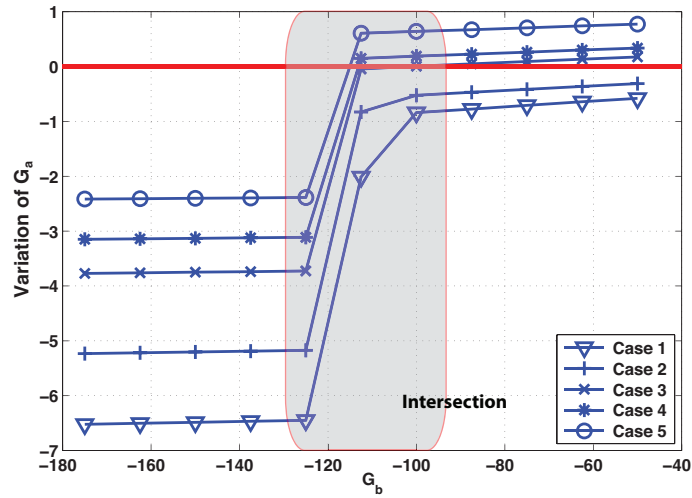
Figure 3.15: Bifurcation morphing modes - different cases (Semi-Temp Figure)

Results obtained for several cases of multiple mass variations by the bifurcation morphing approach with delayed nonlinear feedback are shown in Tab. 3.3. For each case, simultaneous mass variations are applied at both locations (A and B) within a range from 5% to 20% variations of the mass of a single finite element. The maximum relative error for the parameter reconstruction is 3.65% among the tested cases. Note that this relative error is calculated for the variation level (expressed in percentage). Thus, the actual physical relative error is much smaller.

Table 3.3: Reconstruction results from numerical simulations

Case	location	Variation	Reconstruction	Relative Error [%]
1	A	0.07	0.0674	3.65
	B	0.18	0.1787	0.72
2	A	0.08	0.0784	2.04
	B	0.14	0.1392	0.54
3	A	0.12	0.1190	0.87
	B	0.09	0.0896	0.42
4	A	0.13	0.1292	0.58
	B	0.07	0.0697	0.38
5	A	0.18	0.1797	0.18
	B	0.04	0.0397	0.67

3.4 Conclusions and Discussion

New studies of the bifurcation morphing and nonlinear feedback excitation have been presented. The primary topic was the time delay. Time delay is unavoidable for a feedback control system. This (naturally embedded time delay) can have disadvantageous side-effects for sensors based on bifurcation morphing. In particular, it produces undesirable high sensitivity of the boundary to small variations in the time delay and that makes it difficult to achieve high sensing performance. To resolve this critical issue, additional time delay can be applied in the feedback excitation. As the time delay increases, the bifurcation boundary is observed to converge onto a small area in the parameter space. Furthermore, the convergence/stabilization of the bifurcation boundary significantly reduces the sensitivity of the boundary morphing to fluctuations in the time delay. As a consequence, the additional time delay enhances the bifurcation morphing method by reducing and stabilizing the stable region of the system in the parameter space.

Unintended side-effects of the additional time delay are also observed. As time delay increases, the bifurcation boundary curves within the same frequency range (for the post bifurcation regime) are longer in the parameter space. At the same time, as a result of the convergence of the stable region, the total length of the bifurcation boundary becomes shorter as the time delay increases. As a consequence of both these phenomena, the bifurcation boundary has limited range of frequencies, and that results in variations of the boundary which are alike for different types (i.e. levels, locations) of parameter (mass) variations. Therefore, it becomes harder to identify linearly independent bases for multiple parameter variations (such as variations of various types and locations). This issue is compensated by the increased number of intersections observed as the time delay increases. Intersections divide the bifurcation boundary in multiple boundary curves with

distinct characteristics. Using multiple boundary curves, the bifurcation morphing method successfully detects simultaneous parameter (mass) variations. Note that various combinations of sensors have to be tested for finding the highest sensitivities. A similar process can be applied to other applications involving structures with various sensor locations and damage (parameter variation) locations.

Only supercritical Hopf bifurcations were considered. Other types of bifurcation can be considered also but are not discussed. Nonetheless, various other types of bifurcation can be induced by designing the form of the nonlinear feedback excitation.

The level of energy injection by the controller may be high for some types of structures and applications such as damage detection method. However, this level is common for vibration-based cantilever sensors (like resonant mass sensors). The high sensitivity and the ability to detect multiple simultaneous parameter variations show a great potential for sensing.

CHAPTER IV

Forecasting a Class of Bifurcations: Theory and Experiment

4.1 Introduction

Forecasting bifurcations (i.e. predicting bifurcations before they occur) is a significant challenge, especially when an accurate model of the system of interest is not available. In this work, we focus on a certain class of bifurcations. Specifically, jump phenomena (via subcritical and/or saddle-node bifurcations) are important in many applications because they correspond to sudden and dramatic changes in the system dynamics. These types of nonlinear phenomena have been observed and discussed in a variety of systems, e.g. physical systems governed by equations of motion such as the Schrödinger equation [61] or the Swift-Hohenberg equation [62], climate systems [63], ecological systems [64, 65], biomedical systems (exhibiting behaviors such as asthma [66] or epileptic seizures [67, 68]), neuron systems (exhibiting pulse propagation [69]), and global finance systems [70].

Several system characteristics have been explored for forecasting bifurcations of interest (e.g. noise-induced spectrum [71], virtual Hopf phenomenon [72], skewness of probability distributions [73] or flickering in bistable regions before bifurcations [74, 75]). In particular, the critical slowing down phenomenon [76] has been employed as the underlying physical basis of various existing approaches for forecasting the occurrence of

bifurcations [77]. Consider an attractor of the dynamics of a system (e.g. a stable fixed point, a stable limit cycle or a chaotic attractor). When a small perturbation is applied to the system, the dynamics converge toward the attractor at some (recovery) rate. The critical slowing down means that this recovery rate approaches zero as a parameter of the system varies and the size of the basin of attraction shrinks to nil [78]. As a consequence, in the pre-bifurcation regime, the recovery rates (from small perturbations) decrease as the system approaches the bifurcation. These effects can be observed quite far from the bifurcation [77]. Hence, quantifying the effects of the critical slowing down is one method which can be used as an indicator of nearby bifurcations.

Nearby bifurcations have been predicted in various complex systems by monitoring the recovery rates of the system from *small* perturbations. Methods used have included monitoring changes in the autocorrelation [79] or the variance [80] of the system response to small perturbations (which are consequences of the critical slowing down [77]). These techniques for forecasting bifurcations have been studied for various systems, such as ecosystems [80–82], climate dynamics [83], cell signaling [84], and ocean dynamics [79]. Such studies are still far from being able to predict/forecast the most complicated bifurcations when an accurate model of the system is not available. Also, in current techniques there are often two implicit assumptions that the dynamics of the system takes place on a very low dimensional manifold, and that the bifurcations are co-dimension one. Even more importantly, when a physical system is available for testing, the level of perturbations which can be applied to the system have to be very small. That is because the formulations based on observations of critical slowing down have been derived in close proximity to the attractor (by linearization after eliminating higher order terms).

In this paper, an alternate approach to characterizing the recovery rates of dynamical systems is proposed. Specifically, the rate of change of the amplitude of the dynamics

(including certain higher order terms) is quantified. This new characterization shows that critical slowing down can also be observed when using much larger levels of perturbation. By tracking the change of the recovery rate from large perturbations, it is possible to predict both stable and unstable branches in a bifurcation diagram. Of course, when an accurate numerical model is available, bifurcation branches can be computed using several computational bifurcation tools, e.g. AUTO [85], DDE-BIFTOOL [86] and PDDE-CONT [87]. Only a few recent studies consider detecting unstable periodic orbits in the bifurcation diagram experimentally [88–90]. These approaches use controllers to stabilize unstable orbits and track them while a parameter of the system is varied. Such approaches are useful in detecting many types of bifurcations. However, controller-based approaches have many requirements. In contrast, the proposed approach does not require a controller and does not need the parameter to vary (or to enter the post-bifurcation region). Instead, this approach predicts the bifurcation and the unstable branches simply by tracking the recovery rate of the system dynamics. These advantages come at the price of limiting the class of bifurcations which can be tracked. Specifically, only Hopf and saddle-node bifurcations can be handled. Nonetheless, the characterized recovery rates can be used to predict both the occurrence and the type of bifurcations (i.e. supercritical or subcritical) before they occur.

Numerical simulations and experimental results are provided to demonstrate the use of our technique for forecasting bifurcations. Limit cycle oscillations of a simple mechanical system are used in the experiments. To simulate bifurcations of limit cycle oscillations, properly designed nonlinear feedback excitations are applied so that the desired types of bifurcations take place in an otherwise linear system. Nonlinear feedback excitations have been employed in structural health monitoring [42, 91] and sensing [92] as an active interrogation approach. However, the feedback control, in this paper, is only used as a tool

to simulate desired nonlinear dynamics. The proposed approach does not require any type of control to be applied. As the time scale of the system used herein is very short (compared to several systems used in current studies [77]), our experimental set-up provides large amounts of data in a short time. Moreover, the results obtained using the proposed approach suggest that predictions of bifurcations by critical slowing down can be sufficiently accurate for applications to engineered systems which generally require high precision (such as sensing). Many of engineered systems experience the class of bifurcations of interest here (subcritical/supercritical Hopf bifurcations and/or saddle-node bifurcations), e.g. relief valves [93], shape memory oscillators [94], aeroelastic systems [95], machine tools [96], and automotive components such as torque converter clutches [97].

4.2 Theory

This section presents a method to forecast bifurcations by using time series collected *only* in the pre-bifurcation regime. The method is based on observation of how the system recovers to its equilibrium state from perturbations. Such a recovery of the oscillation amplitude to equilibrium is shown in FIG. 4.1. Discussion focuses on forecasting co-dimension one supercritical/subcritical Hopf bifurcations and saddle-node bifurcations.

Consider a nonlinear system with the perturbed dynamics characterized by an amplitude r, and a fixed point or periodic dynamics characterized by an amplitude $\tilde{r}$. Consider also that a perturbation with a certain level r_0 is applied initially to the system. When the system has a stable behavior, it converges from the initial perturbation r_0 back onto the (stable) fixed point or the (stable) limit cycle of amplitude $\tilde{r}$ as shown in FIG. 4.1. When the system has an unstable fixed point or an unstable limit cycle, the amplitude r diverges away from $\tilde{r}$. The time rate of change of the amplitude in either of these cases is

considered to be of the form

$$\dot{r} = r \left[\alpha(\mu - \mu_c) - p(r) \right], \tag{4.1}$$

where α is a fixed parameter of the system, μ is a controlled/monitored parameter of the system, μ_c is the critical value of the parameter μ where a bifurcation occurs, and $p(r)$ is a polynomial function of r with $p(0) = 0$. Note that $p(r)$ is assumed to be independent of the control parameter μ. This is an important assumption which delineates the range of application of the proposed method. Here $\alpha > 0$, and the pre-bifurcation regime corresponds to $\mu < \mu_c$. In the pre-bifurcation regime, the dynamics of the system has a fixed point at $r = 0$. In the post-bifurcation regime, the dynamics has one fixed point at $r = 0$ and another at $\tilde{r}$, where $\tilde{r}$ is given by $p(\tilde{r}) = \alpha(\mu - \mu_c)$. Also, note that, in general, α is not known unless an accurate model for the system is available. Herein, we consider α an unknown that has to be identified/detected.

The rate of change of the phase θ of the system is not considered because we do not focus on infinite period bifurcations or other similar bifurcations. The phase of the system can be defined for any system exhibiting a limit cycle oscillation of period T to reveal the fact that the dynamics is periodic. Hence, θ varies by 2π when time varies by T. Only a generic phase definition is needed because the proposed approach uses only the amplitude of the oscillations as input data (and the system response is assumed to be periodic). Hence, θ and $\dot{\theta}$ do not significantly influence the analytic formulation.

The rate of amplitude variation at time t is defined as

$$\lambda(\mu, r) = \frac{d \log r}{dt}. \tag{4.2}$$

Using Eq. (5.4) one obtains

$$\lambda(\mu, r) = \frac{1}{r}\dot{r} = \alpha(\mu - \mu_c) - p(r). \tag{4.3}$$
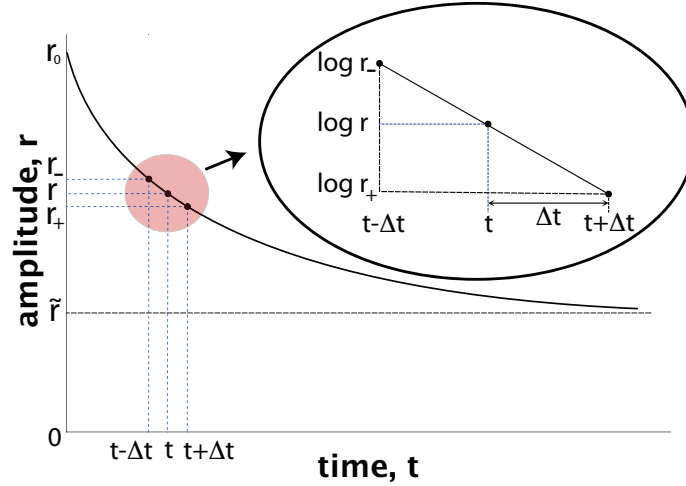
Figure 4.1: The rate function λ can be measured at each level of perturbation by measuring r_-, r and r_+ at times $t - \Delta t$, t and $t + \Delta t$. Note that perturbations do not have to be small. Only Δt needs to be small.

The rate of amplitude variation λ in Eq. (4.3) is a function of μ (the controlled/measured parameter) and r (the amplitude at time t), and is composed of two terms. The first term $\alpha(\mu - \mu_c)$ is the distance from the current parameter value μ to the critical value μ_c scaled by the fixed coefficient α. The second term $p(r)$ is a polynomial which characterizes the type of bifurcation.

Consider that measurements are collected at times $t - \Delta t$, t and $t + \Delta t$ to obtain three amplitudes r_-, r and r_+ as shown in FIG. 4.1. To determine λ, one can employ the following approximation

$$\lambda(\mu, r) = \frac{d \log r}{dt} \cong \frac{\log r_+ - \log r_-}{2\Delta t}, \tag{4.4}$$

which holds for small Δt. Note that the measured perturbations r_-, r and r_+ do not have to be infinitesimal as long as Δt is small.

Generally, λ can be exploited in either the r-λ space or the μ-λ space. First, consider the dynamics of the system for a fixed parameter μ and a varying perturbation level r. As

a. dependence of λ on r for a fixed μ b. bifurcation diagram
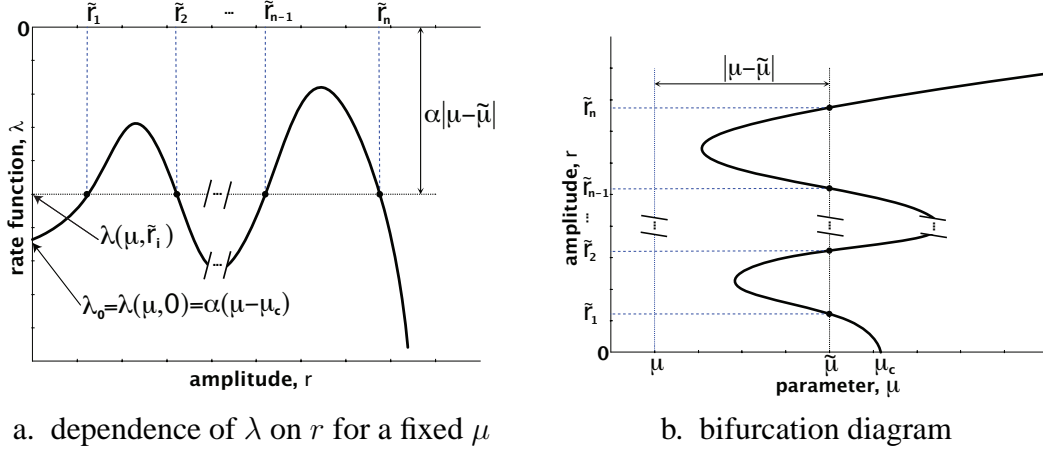
Figure 4.2:
Once λ is obtained for a certain μ, the shape of the actual bifurcation can be predicted without exploring the post-bifurcation regime. For each i, $\lambda(\mu, \tilde{r}_i) = \alpha(\mu - \tilde{\mu})$ and the actual distance between μ and $\tilde{\mu}$ can be estimated (for a known α). Note that α can be easily obtained by measuring (as few as only) two values of λ for two distinct values of μ.

shown in FIG. 4.2a, the dependence of λ on r is a polynomial given by

$$\lambda(\mu, r) \;=\; \lambda_0 - p(r), \tag{4.5}$$

where $\lambda_0 = \alpha(\mu - \mu_c)$ represents the rate of amplitude variation when r tends to zero, $\lambda(\mu, r = 0)$. Different polynomials $p(r)$ correspond to distinct types of bifurcations. Therefore, the shape of $\lambda(\mu, r)$ in the r-λ space can be used to determine the type of bifurcation which takes place at $\mu = \mu_c$. Note that the bifurcation is forecasted, i.e. it is identified *before* it takes place (using only μ values which are less than μ_c). This ability to forecast is not found in other existing techniques [85–90].

In general, for a given parameter value $\mu = \tilde{\mu}$, a system may have several coexisting fixed points or limit cycles. Consider the amplitude $\tilde{r}_i$ of one of those stable/unstable fixed points or limit cycles. As shown in FIG. 4.2b, all points $(\tilde{\mu}, \tilde{r}_i)$ on the bifurcation curve satisfy the equation of motion and correspond to fixed points for r. Hence,

$$\dot{r}(\tilde{\mu}, \tilde{r}_i) = \tilde{r}_i \left[\alpha(\tilde{\mu} - \mu_c) - p(\tilde{r}_i) \right] = 0. \tag{4.6}$$

Now, recall the dependence of λ on r expressed in Eq. (4.3) (and presented in FIG. 4.2a). For all $\tilde{r}_i$, the value of $\lambda(\mu, \tilde{r}_i)$ is the same, as we show here

$$
\begin{aligned}
\lambda(\mu, \tilde{r}_i) &= \alpha(\mu - \mu_c) - p(\tilde{r}_i) \\
&= \alpha(\mu - \tilde{\mu} + \tilde{\mu} - \mu_c) - p(\tilde{r}_i).
\end{aligned}
\tag{4.7}
$$

Using Eq. (4.6), one obtains

$$
\begin{aligned}
\lambda(\mu, \tilde{r}_i) &= \alpha(\mu - \tilde{\mu}) + \overbrace{\alpha(\tilde{\mu} - \mu_c) - p(\tilde{r}_i)}^{0} \\
&= \alpha(\mu - \tilde{\mu}).
\end{aligned}
\tag{4.8}
$$

Eq. (4.8) reveals the fact that the value of λ at $\tilde{r}_i$ represents the distance (scaled by α) from the current μ to $\tilde{\mu}$. Note that for each i, $\lambda(\mu, \tilde{r}_i)$ is a line in the μ-λ space, which has the slope of α and crosses the μ-axis ($\lambda = 0$) at $\tilde{\mu}$. An example of such a line (defined by Eq. (4.8)) is shown in FIG. 4.4. One can measure $\lambda(\mu, \tilde{r}_i)$ for as few as two distinct values of μ to obtain this line. This requirement is distinct from classical approaches where μ has to have many values which span both the pre-bifurcation and the post-bifurcation regimes. Next, the fixed coefficient α can be estimated as it is the slope of the line (defined by Eq. (4.8)). One can then measure λ (for a given value of $\tilde{r}$, and a given value of μ) and compute $\tilde{\mu}$ as

$$
\tilde{\mu} = \mu - \frac{1}{\alpha}\lambda(\mu, \tilde{r}).
\tag{4.9}
$$

Finally, the bifurcation diagram can be predicted by the set of points $(\tilde{\mu}, \tilde{r})$.

Note that λ is derived without eliminating higher order terms. Hence, its definition can be used at any level of perturbation. Based on the values of λ at large amplitudes, one may predict the distance to μ_c from the current μ by estimating $\lambda_0 = \alpha(\mu - \mu_c)$ from Eq. (4.5). In most cases, it is a challenge to observe the system dynamics (and estimate λ) from very small perturbations because the measurements of actual dynamics can be

obscured by noise. Therefore, the estimated value of λ_0 is more accurate if obtained using data collected for sufficiently large amplitudes.

The general algorithm for forecasting the bifurcation diagram using this approach is as follows:

1. For a given value of the parameter $\mu = \mu_k$ (with $k = 1 \cdots M$, where M is chosen by the user), a perturbation is applied to the system, and amplitude values r_j (with $j = 1 \cdots N$, where N is chosen by the user) are collected at various time instances t_{jk}.

2. Using Eq. (4.4), the rate of amplitude variation $\lambda_{jk} = \lambda(\mu_k, r_j)$ is computed at time t_{jk} for all $j = 1 \cdots N$.

3. The slope α_j of the line $\lambda(\mu_k, r_j)$ vs. μ_k is computed for each r_j ($j = 1 \cdots N$). Note that these N values of α_j can be averaged over j to obtain an average value of α for improved noise rejection.

4. A value of $\tilde{\mu}_{jk}$ is obtained for each μ_k ($k = 1 \cdots M$) and each r_j ($j = 1 \cdots N$) using Eq. (4.9) (where $\tilde{r}$ has a value $\tilde{r}_j$ of r_j) and the slope α obtained at step 4. Note that these M values of $\tilde{\mu}_{jk}$ can be averaged over k to obtain an average value for $\tilde{\mu}_j$ for improved noise rejection.

The bifurcation diagram is finally obtained as the plot of $\tilde{r}_j$ vs. $\tilde{\mu}_j$ for $j = 1 \cdots N$ (where $\tilde{r}_j = r_j$).

4.3   Results

In this section we demonstrate our approach by applying it first to a numerical model and then to an experimental system.

a. exact and predicted bifurcation   b. λ vs. r
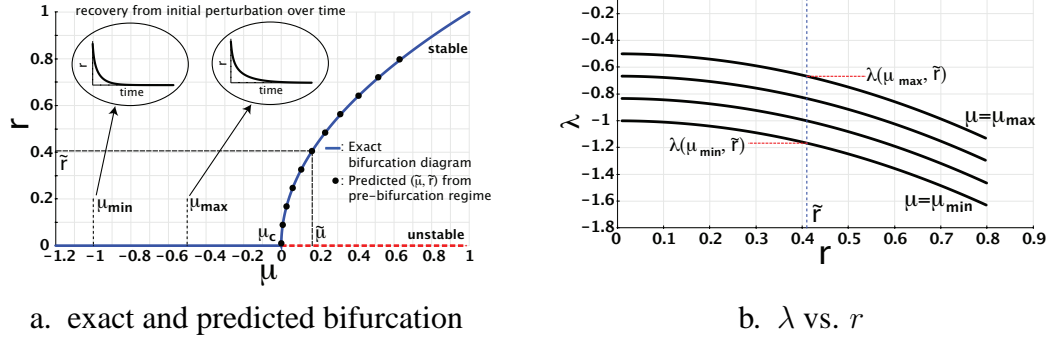
Figure 4.3:
Predictions based on λ are demonstrated using a numerical model for a super-critical Hopf bifurcation.

4.3.1 Numerical results

Forward (supercritical) and backward (subcritical) Hopf bifurcations are considered. The governing equations of motion for systems with such bifurcations are of the form shown in Eq. (5.4). They are characterized by two different types of polynomials $p(r)$ as follows

$$p_f(r) \;=\; \beta r^2, \tag{4.10}$$

$$p_b(r) \;=\; -\beta r^2 + \gamma r^4. \tag{4.11}$$

The values of $\beta = 1$ and $\gamma = 1$ are used to obtain numerical data. The values of μ_c and α from Eq. (5.4) are considered to be $\mu_c = 0$ and $\alpha = 1$. The results obtained for λ, and the predictions made for both bifurcations are presented in FIG. 4.3 and FIG. 4.5.

For a supercritical Hopf bifurcation, values for λ were obtained in a range of μ from $\mu_{min} = -1$ to $\mu_{max} = -0.5$, with a given initial perturbation amplitude $r_0 = 0.8$. The curve shown in FIG. 4.3a is the exact bifurcation diagram obtained by analytically solving $\dot{r} = 0$ for r at every μ between -1.2 and 1. The points $(\tilde{\mu}, \tilde{r})$ in FIG. 4.3a are predictions obtained by the proposed approach using multiple curves of λ collected for distinct values of μ between μ_{min} and μ_{max}. Specifically, the values of λ for a certain amplitude $\tilde{r}$ on
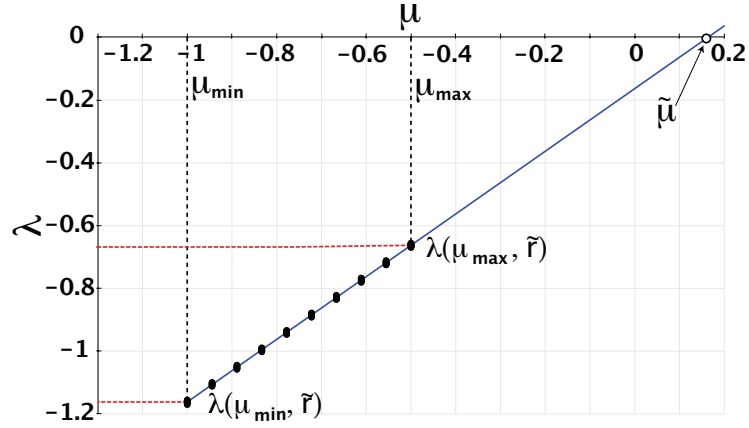
Figure 4.4: Each predicted point for $\tilde{r}$ in FIG. 4.3a is estimated by line fitting the measurements of $\lambda(\mu, \tilde{r})$ for various μ. The slope of the line fitting all measurements (for a given $\tilde{r}$) is α.

the dotted line shown in FIG. 4.3b are projected onto the μ-λ space as shown in FIG. 4.4. As discussed in Section II, this line has the slope of α and crosses the μ-axis (λ=0) at $\tilde{\mu}$. All predicted points shown in FIG. 4.3a are obtained by the same approach under the assumption that α is unknown (and must be measured). Note that, once α is identified, measurements of λ for a single μ value are sufficient to obtain a prediction for the entire bifurcation diagram in FIG. 4.3a.

For a subcritical Hopf bifurcation, the range considered for μ was from $\mu_{min} = -2$ to $\mu_{max} = -1$, and the initial perturbation amplitude was $r_0 = 1$. The results shown in FIG. 4.5 were obtained by exactly the same procedure as for the supercritical Hopf bifurcation (FIG. 4.3). However, the curves obtained are distinct because the polynomial used to generate the (numerical) data is that given in Eq. (4.11) instead of Eq. (4.10). Additional important results are observed in the subcritical case. For example, the new approach can successfully predict the saddle-node bifurcation of cycles located at point S in FIG. 4.5a. The predicted points approximate very well the exact location of the saddle-node bifurcation. In addition, the large amplitude of the emerging limit cycle at point S is

captured accurately.

a.   exact and predicted bifurcation

b. λ vs. r
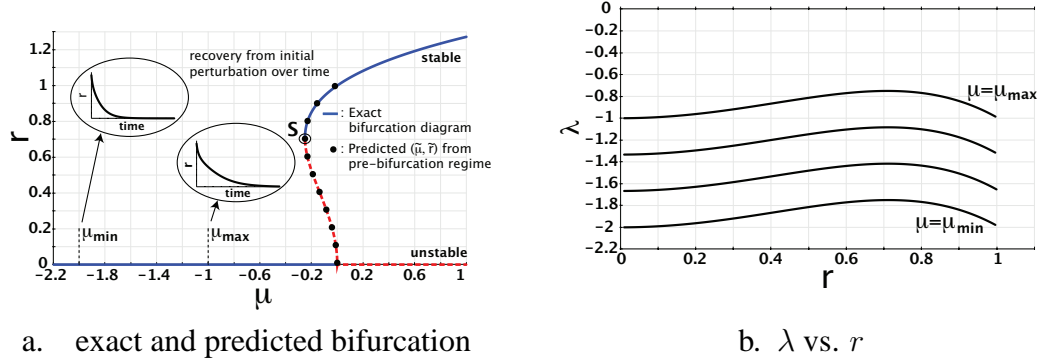
Figure 4.5:   Predictions based on λ are demonstrated using a numerical model for a sub-critical Hopf bifurcation.

The predicted bifurcation diagrams obtained based on λ measured in the pre-bifurcation regime perfectly match the analytical diagrams for the numerical models of general Hopf bifurcations considered. The predicted information includes the locations of the bifurcation points, and the whole bifurcation diagram, including the unstable limit cycles. The curves of λ vs. r were obtained by tracking the time history of the system during its recovery from the initial perturbations.

Several time history plots shown as inserts in FIG. 4.3a and FIG. 4.5a demonstrate that it is not easy to discern specific bifurcation characteristics without proper analysis. Our approach presents a clear characterization of the time histories both qualitatively (between different types of bifurcations), and quantitatively (between different values of μ for the same bifurcation). Our technique is experimentally demonstrated and verified in the next section for limit cycle bifurcations of a mechanical oscillatory system.

4.3.2   Experimental results

A clamped-free aluminum beam is used in the experiments. To induce supercritical or subcritical Hopf bifurcations in the system dynamics, nonlinear feedback excitations are applied to enhance the nonlinearity of the system [42]. A diagram of the experimen-

tal system is shown in FIG. 4.6. As shown in the figure, a piezo-sensor and a pair of piezo-actuators are attached to the aluminum beam. The sensor output signal is conditioned through a charge amplifier and is the input to a real-time processor. In the real-time processor, the sensor output data is stored while the data is also used to form a designed nonlinear feedback excitation, which is then amplified and sent to the piezo-actuators on the beam. Note that the feedback controller is not a requirement of the proposed approach to forecast bifurcations, but is used only for creating a system which exhibits the desired bifurcations. The proposed approach only uses the time series data from the sensor. The controller actuation is used to provide an excitation which repeatedly induces large level perturbations to the system. That is done for the sake of experimental validation and is not needed when other external perturbations exist or can be easily applied. Also, note that the large level perturbations applied do not have to be identical.
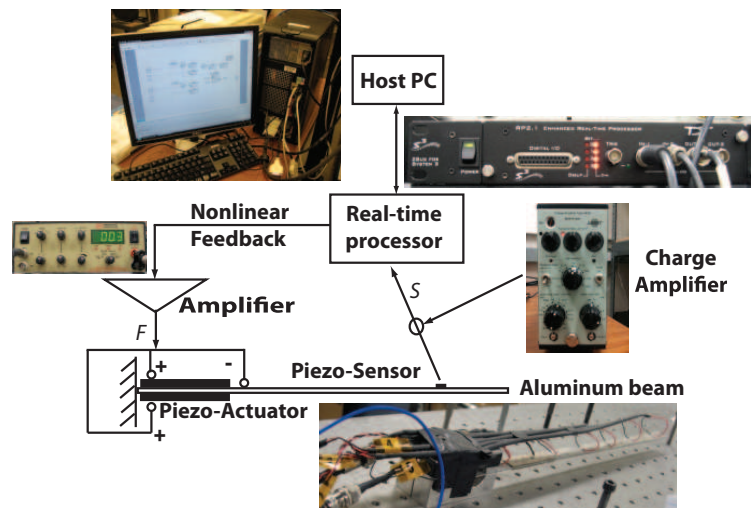
Figure 4.6: An aluminum beam is used for experimental tests. Nonlinear feedback is designed and applied to generate supercritical or subcritical Hopf bifurcations. Only one of the sensors on the beam is used in these experiments. From the piezo-sensor output signal s which is proportional to the amplitude of oscillation, nonlinear feedback F is formed and applied to the base of the beam (as a locally distributed bending) by a pair of piezo-actuators.

a. supercritical Hopf bifurcation (μ=0.9)   b. subcritical Hopf bifurcation (μ=2)
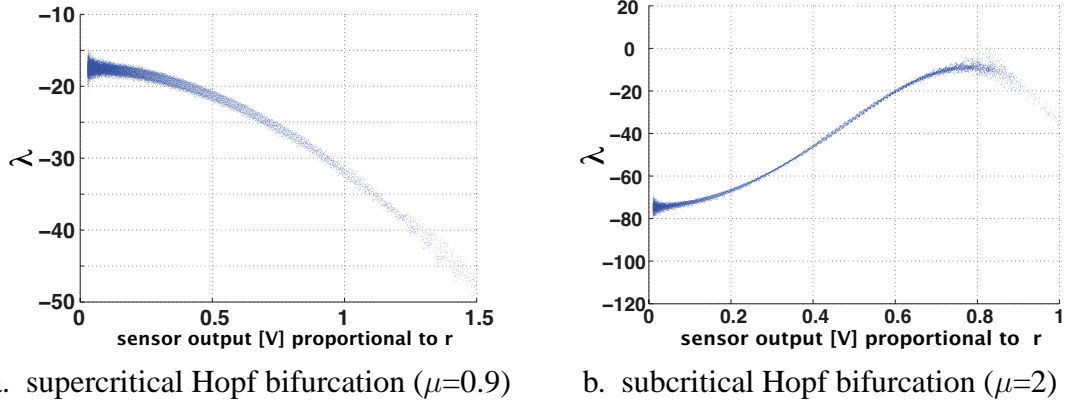
Figure 4.7: 4000 values of λ are obtained for distinct r values from a transient phase. The process is repeated 16 times for each μ value.

To induce desired supercritical or subcritical Hopf bifurcations, nonlinear feedback is generated from the piezo-sensor output signal s which is proportional to the oscillation amplitude. The nonlinear feedback is applied to the beam (as a locally distributed bending) by a pair of piezo-actuators attached on both (upper and lower) sides of the beam. The nonlinear feedback F can be expressed as a function of the sensor output s as

$$F = \mu s + \beta s^3 + \gamma s^5, \tag{4.12}$$

where μ is the control parameter, and β and γ are the nonlinear feedback gains, which are fixed for each desired bifurcation. For creating a supercritical Hopf bifurcation, nonlinear gain parameters are fixed as $\beta = -0.01$ and $\gamma = 0$, with 20 dB of charge amplifier gain. For creating a subcritical Hopf bifurcation and a saddle-node bifurcation, nonlinear gain parameters are fixed as $\beta = 5$ and $\gamma = -0.05$, with 10 dB of charge amplifier gain. These parameters were chosen based on a few preliminary experimental tests.

Each experiment consists of two steps. The first step is to obtain the actual bifurcation diagram by the classic method of parameter sweeping. This step is performed so that the predictions obtained using our approach can be compared to the actual bifurcation diagram. To obtain the actual bifurcation diagram, the linear feedback gain (the controllable

parameter μ) is changed from pre-bifurcation values to post-bifurcation values in the parameter space. For subcritical bifurcations, a reverse sweep in the parameter is also applied (to capture the jump phenomenon at the saddle-node bifurcation of cycles). After ignoring transients, the amplitude of the limit cycle oscillations is obtained and plotted vs. its corresponding parameter value to obtain a bifurcation diagram. The bifurcation diagram obtained by this classic method is shown in FIG. 4.8 in form of dashed lines. Note that the lines in FIGs 4.8b and 4.8c which (at first glance) may look like an imperfect bifurcation are an artifact of the plotting of the results. They are caused by the finite step size between each parameter value considered in the classical method. Lines (connecting actual measured points) are used instead of points for better visibility because the results of our approach are marked as circles (with error bars). Also, the jump phenomena presented in FIGs 4.8d, 4.8e and 4.8f are caused by subcritical Hopf bifurcation and saddle-node bifurcation. Note that the jump phenomena may also be observed for supercritical Hopf bifurcations as a delay effect for systems with slowly varying parameters [109]. However, in the experiment herein the applied nonlinear feedback is designed specifically to induce a subcritical Hopf bifurcation, and the parameters of the system are maintained constant long enough to reach steady-state for each parameter value.

The second and critical step is to predict the bifurcation location and shape using only λ values obtained in the *pre-bifurcation* regime. To obtain the curve of λ for a fixed parameter μ, a perturbation is applied to the system. The perturbation is caused by a harmonic excitation (with a high frequency and a certain amplitude) which is applied to the system for a very short time, to provide a desired perturbation. After the perturbation, the dynamics of the system in its transient regime (as the system recovers from its perturbed state) are recorded. Specifically, the amplitude of the oscillation is measured during the transient phase. In this case, recovery is complete when the transients decay to zero. Note

a. based on multiple μ values   b. $\mu = 0.45$ c. $\mu = 0.95$

d. based on multiple μ values   e. $\mu = 1$ f. $\mu = 2$
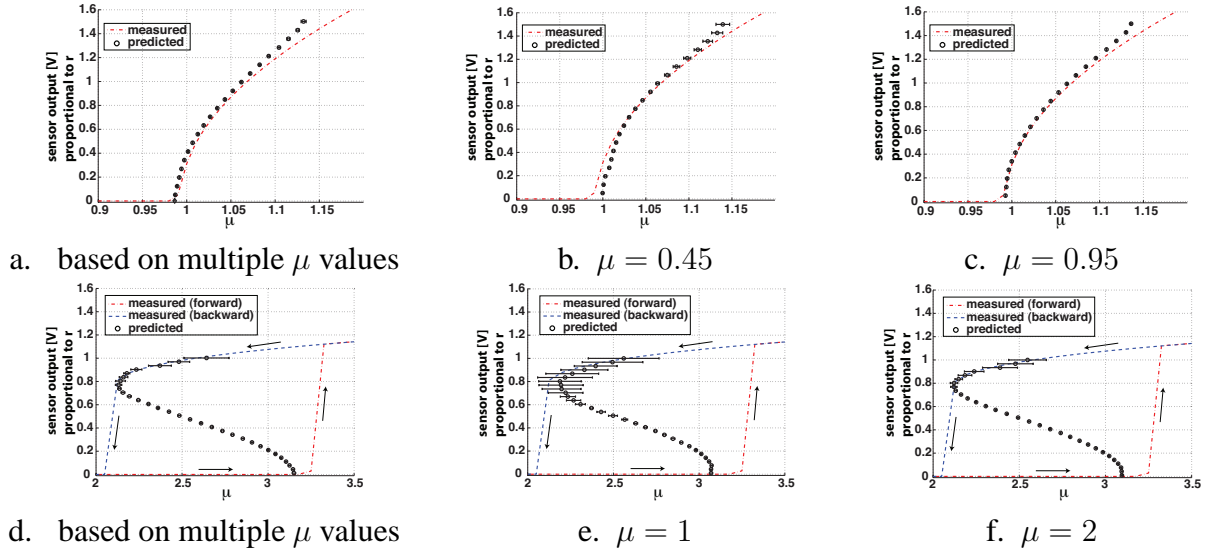
Figure 4.8: Predictions for the bifurcation diagram obtained based on λ are demonstrated for supercritical and subcritical Hopf bifurcations. The upper plots (a, b and c) are for a supercritical Hopf bifurcation, and the lower plots (d, e and f) are for a subcritical Hopf bifurcation. The dashed lines represent the actual bifurcation diagram measured by applying actual parameter variations in the post-bifurcation regime. Results show that predictions are more accurate when they are based on λ values obtained at multiple μ values. Also, once α is calculated, predictions are most accurate when they are based on measurements at a value of μ close to the actual bifurcation, i.e. for μ close to μ_c. The horizontal bars represent standard deviation error bars computed for each predicted point on the bifurcation diagram.

that the frequency of the short perturbations is chosen close to the resonant frequency of the system. Other types of perturbations can be applied, however they may place more stringent restrictions on the data acquisition (sampling rate and resolution). Although interesting, the study of other perturbations is beyond the scope of this paper.

The resonant frequency of the system (close to the bifurcation) was measured experimentally and found to be approximately 6.1 kHz for both supercritical and subcritical Hopf bifurcations. The sampling rate of the data acquisition was approximately 200 kHz.

The measured dependence of λ on r for supercritical and subcritical Hopf bifurcations is shown in FIG. 4.7. For a given value of μ, a time series of 4000 individual r values was

obtained as the system decayed to the equilibrium (zero) state. Then the values of λ were obtained using Eq. (4.4) for those r values. This process was repeated 16 times for each μ value. In obtaining λ values using Eq. (4.4), experimental noise can affect small values of r and lead to large errors in λ. Hence, r values below a pre-set minimum amplitude were eliminated. This minimum amplitude depends on the data acquisition system used. For the results herein, the value used was 50 mV. Note that our method is designed to provide estimates for the values of λ even when these values are small. This is accomplished by taking advantage of data obtained from larger perturbations, and by using the curves of λ in the r-λ plane. These results are demonstrated in FIG. 4.7, where the amplitude of the dynamics r is proportional to the output voltage of the sensor.

For the supercritical Hopf bifurcation, values of μ were chosen between $\mu_{min} = 0.45$ and $\mu_{max} = 0.95$. Similarly, for the subcritical bifurcation, μ values between $\mu_{min} = 1$ and $\mu_{max} = 2$ were used. 11 distinct values of μ were selected for the experiments in each of these ranges. In the μ-λ space, line fitting was conducted to predict the location of each corresponding limit cycle amplitude (similar to what was done using numerical data to obtain the results in FIG. 4.4). Also, the value of α was estimated based on the slopes of the lines in the μ-λ space. The value of α obtained for the supercritical Hopf bifurcation is $\alpha_f = 195.82$ (with a standard deviation of 1.56), and for the subcritical Hopf bifurcation is $\alpha_b = 66.81$ (with a standard deviation of 2.93). As shown in FIG. 4.8, the predictions using Eq. (4.9) match the actual bifurcation diagrams very well.

Our results also show that a bifurcation can be predicted quite well even when measurements obtained at a single value of μ are used (once α is obtained). Note that in all measurements, μ is lower than the value where the system actually encounters the bifurcation (at μ_c).

Figures 4.8b, 4.8c, 4.8e and 4.8f present the predictions obtained using measurements

at single values of μ. Figures 4.8b and 4.8e show results obtained using a value of μ which is μ_{min}, and is the farthest from the actual bifurcation (at μ_c). Figures 4.8c and 4.8f show results obtained using a value of μ which is μ_{max}, and is the closest to the actual bifurcation (at μ_c). As the parameter μ approaches its bifurcation value μ_c, the predictions based on λ are more accurate. Note, however, that the bifurcation is well predicted even when using measurements collected at μ_{min}. These measurements are quite far from the bifurcation (half way between zero feedback and the actual bifurcation point). For the subcritical Hopf bifurcation (FIGs. 4.8d, 4.8e and 4.8f), one can observe a small difference between the actual and the predicted bifurcation points. However, these results are reliable, especially considering that the values of μ are chosen in a range well below μ_c (where the saddle-node emerges).

4.4 Discussion and Conclusions

A new method of characterizing the dynamics of a nonlinear system during its transient recovery to a stable limit cycle or a stable fixed point after perturbations (in the pre-bifurcation regime) was presented. The proposed approach is designed for forecasting bifurcations of fixed points or limit cycles. By keeping all higher order (nonlinear) information in the formulation, the perturbation levels do not have to be small. Allowing for large perturbations is important because it can be challenging to measure recovery from small perturbations due to a loss of accuracy caused by noise and/or a lack of resolution in measurement. In most cases, operating with larger perturbations is a good way to resolve such accuracy issues and obtain better predictions of the bifurcations without the need to explore the post-bifurcation regime. Also, the recovery rates obtained using large perturbations enable the prediction of locations in parameter space where the stable/unstable limit cycles lie as well as the amplitudes of those limit cycles.

Another important feature of the proposed method is its ability to accurately predict saddle-node bifurcations and unstable limit cycles for the case of subcritical Hopf bifurcations. There are several recent studies to experimentally follow unstable branches by means of feedback control. However, those studies differ fundamentally from the approach in this paper. The proposed method predicts the unstable branches without following them, i.e. in the pre-bifurcation regime (where the system always recovers to its equilibrium). From a practical standpoint, this is clearly the safest way to investigate a system. Furthermore, the use of feedback in this paper is only for the purpose of creating a well known system which can be used for quantitative evaluation of the predictions our method provides. In contrast to other experimental techniques [88–90], the feedback is not needed (and not used) for forecasting the bifurcations or the unstable branches. Due to its minimal requirements (i.e. time series data), the proposed method has strong potential for application to other areas, such as biological systems or natural systems, where the implementation of feedback control for the purpose of forecasting bifurcations or measuring unstable branches may be difficult.

A clamped-free aluminum beam with a nonlinear feedback excitation was introduced for experimental verification of the proposed method. The oscillatory system with nonlinear feedback has several advantages for testing nonlinear techniques. First, desired types of bifurcations can be induced easily in the system because the nonlinearity of the system comes from the control feedback (which can be designed for each specific case of interest). Second, the predicted shape of the bifurcation can be obtained very quickly because (once α is known) a single time history of the recovery from a large perturbation contains all necessary information for the range of the corresponding amplitudes as well. This contrasts with classical techniques where the bifurcation parameter has to be varied and many steady-state curves have to be measured to obtain the bifurcation diagram. In addition,

the results using the proposed approach are very accurate when compared with results of classical techniques.

In the experiments, the actuation (by the controller) was used to induce perturbations repeatedly. Multiple perturbations were used for two reasons: (1) to enhance the accuracy of the predictions, and (2) to develop a method to predict unstable branches, to be used precisely when the response of the system *is* available for multiple perturbations. Note that, when multiple perturbations are available, they do not have to be the same (e.g., they do not have to have a similar level). Some can be large and some small, or they can be large and of different levels. In fact, natural (small or large) perturbations can be used. The only requirement here is that the system recovers to its equilibrium state from these perturbations. For example, the proposed method (using time series) can be applied to a system which undergoes an impulse-type disturbance during operation (e.g., an aeroelastic system encountering a gust during flight) which causes (large or small) perturbations after which the system recovers to its regular (stable) operating conditions.

Of course, the proposed approach has restrictions on its applicability. First, the dynamics are assumed to be effectively one dimensional and periodic, and the bifurcation is assumed to be co-dimension one. Currently available techniques also consider limited types of dynamics and co-dimension one bifurcations. These studies (and ours) are still far from being able to predict/forecast bifurcations for the most complex systems, especially when an accurate model of the system of interest is not available. Second, if the system does not experience large perturbations (either induced or natural), then one cannot fully take advantage of the proposed method. However, the proposed approach can still be used (in a limited sense) by monitoring small perturbations (either induced or natural) to locate the bifurcation point. Third, the perturbations are assumed to be of a magnitude which does not make the system switch between different attractors. That is, the assumption

is that the system reverts to its initial equilibrium position (or to its initial periodic limit cycle oscillation) in time after the perturbation subsides. Fourth, the nonlinear terms are assumed to be independent of the control parameter. These restrictions are necessary when one needs to forecast the bifurcation (instead of detecting it by sweeping up and/or down a system parameter).

The proposed technique enables the use of larger perturbation levels which broadens its applicability as compared to existing techniques based on the critical slowing down. In addition to predicting where bifurcations occur, the proposed approach can be used to anticipate the type of the bifurcations (supercritical or subcritical) and predict their branches without exploring the post-bifurcation regime. Due to the dramatic change in the dynamics at bifurcations, predicting subcritical and saddle-node bifurcations without placing the system in the post-bifurcation regime provides great advantages in many applications.

CHAPTER V

Forecasting Bifurcation Morphing: Application to Cantilever-based Sensing

5.1   Introduction

Since atomic force microscopes (AFM) have been introduced [1], various cantilever-based sensing techniques have been proposed as tools in various fields. Specifically, MEMS and NEMS resonant sensors have been studied and shown to have remarkable sensitivity [48–53]. In common resonant sensing techniques, changes in resonant frequencies of a cantilever are monitored to detect local mass variations caused by the adsorption or attachment of analytes of interest onto the sensor. Many studies have addressed the idea of enhancing the sensitivity of such resonant sensors. The use of higher order resonance modes, and dimensional reduction of the cantilever have been discussed for enhancing sensitivity [54]. Recently, attogram (10^{-18} g) level mass sensing was demonstrated by structural modifications of the resonant sensors, such as suspended micro-channel resonators [55], or integrated electronic displacement transducers [56].

Various studies of features of nonlinear systems have also been studied for application to cantilever-based sensors, such as electrostatic nonlinear forcing [57], parametric resonances [58, 59], and nonlinear modal interactions [60]. Studies of nonlinear approaches are important because they suggest that higher sensitivity can be achieved by just chang-

ing the algorithm of sensing (for the same sensors which use linear techniques) instead of applying dimensional or structural modifications.

Bifurcation morphing by nonlinear feedback excitation is a novel nonlinear approach for damage detection and sensing [42, 91]. This nonlinear approach is based on inducing a bifurcation by nonlinear feedback applied to a linear structure. The change in the bifurcation point can then be measured and tracked as the system parameters vary. That leads to information about the morphing of the bifurcation boundary in the parameter space. Recently, it has been numerically demonstrated that the bifurcation morphing approach has high sensitivity for cantilever-based sensors. Those results have been complemented by a study of the effects of the time delay on the bifurcation morphing created by nonlinear feedback excitation [110]. In practical applications, the time delay is unavoidable due to the delay caused by measuring the dynamics, creating the nonlinear feedback, and forming the feedback loop. This unavoidable time delay may cause undesirable high sensitivity of the bifurcation points to small variations in the time delay. Additional time delay in the controller has been numerically shown to reduce that undesirable sensitivity and enhance the robustness of the sensor.

While the bifurcation morphing approach has high sensitivity to parameter variations, its use is hindered by the fact that detecting bifurcation points using the common technique of sweeping parameters from pre-bifurcation to post-bifurcation regions (in the parameter space) takes a long time and requires the system to be able to operate safely in the post-bifurcation regime. To characterize bifurcations quickly and maintain the system in the safe pre-bifurcation regime during operation, the recent approach of forecasting bifurcations developed by the authors [111] is applied to the sensor. Forecasting bifurcations has been based on monitoring various system characteristics, such as noise-induced spectra [71], virtual Hopf phenomena [72], skewness of probability distributions [73] or

flickering in bistable regions before bifurcations [74, 75]. Particularly, the critical slowing down phenomenon [76, 78] has been studied as a tool for predicting bifurcations [77] (by monitoring the recovery rate of the system from small perturbations). These techniques for forecasting bifurcations have been discussed for a diversity of applications, including ecosystems [80–82], climate systems [83], cell signaling [84], and ocean dynamics [79]. It has been demonstrated recently [111] that forecasting approaches can predict not only the bifurcation point, but also the type of bifurcation by monitoring the rates at which the system recovers from large perturbation levels. These techniques can also be applied to the engineered systems which generally require higher accuracy [111].

In this chapter, an experimental investigation of a prototype of a cantilever-based sensor using bifurcation morphing coupled with delayed nonlinear feedback excitation and employing bifurcation forecasting is presented. Brief conceptual and theoretical aspects of this work are introduced in Sec. 5.2. Experimental results are presented in Sec. 5.3 where the effects of the controlled time delay are explored in the context of mass sensing.

5.2   Background

5.2.1   Delayed nonlinear feedback excitations

The main idea of the bifurcation morphing approach is to apply nonlinear feedback excitations to the system to actively destabilize its dynamics and create bifurcation points in the parameter space [42]. The goal is to create bifurcation points which have high sensitivity to small parameter variations in the system. Because these bifurcations are created by controlled nonlinear feedback, desired types of bifurcation can be induced by specifically designed nonlinear feedback. For example, consider one of the most common types of bifurcations, namely Hopf bifurcations. The nonlinear feedback excitation F
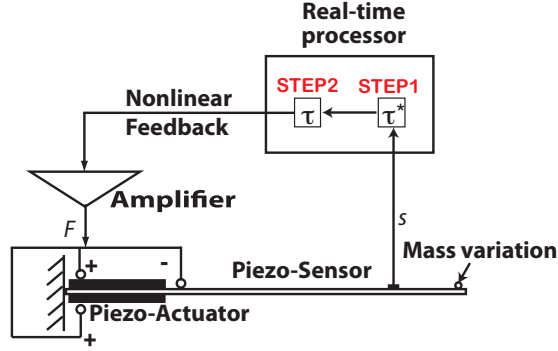
Figure 5.1: A clamped-free aluminum beam with piezo actuators and sensors is used for experiments. Piezo-sensors and a pair of piezo-actuators are attached to the aluminum beam. Mass variations are applied to the tip of the beam. The sensor output is sent to a real-time processor. The unavoidable time delay τ^* is generated during the process of storing data (sensor signal) and creating the nonlinear feedback excitation (STEP1). The controller adds the controlled time delay τ (STEP2) before the nonlinear feedback is amplified and sent to the piezo-actuators on the beam.

applied to create Hopf bifurcations can be expressed as

$$F(t) = \mu s(t) + \beta s(t)^3 + \gamma s(t)^5, \tag{5.1}$$

where s is the output of the sensor used in the feedback loop, and μ is a linear feedback gain (the control parameter), while β and γ are cubic and quintic nonlinear feedback gains. For creating supercritical Hopf bifurcations, β is negative and γ is zero. For creating subcritical Hopf bifurcations, β is positive and γ is negative.

Theoretically, $F(t)$ depends only on $s(t)$. In practical applications, however, there is an unavoidable time delay generated in the controller. The expression of the nonlinear feedback in Eq. (5.1) is thus expressed as

$$F(t) = \mu s(t - \tau^*) + \beta s(t - \tau^*)^3 + \gamma s(t - \tau^*)^5, \tag{5.2}$$

where τ^* is the unavoidable time delay in the controller. This delay takes place during STEP1, as shown in FIG. 5.1. Note that the time delays during signal transfers are negligible.

In the past, it has been shown numerically that the bifurcation points obtained by this approach are sensitive to small variations in the time delay τ^*, especially when τ^* is very short [110]. The sensitivity to fluctuations in τ^* is undesirable because the sensor may lose robustness. To address this problem, an additional time delay τ is implemented as a control parameter in STEP2, as shown in FIG. 5.1. Then, the nonlinear feedback in Eq. (5.2) can be rewritten as

$$F(t) \;=\; \mu s(t - \tau_{tot}) + \beta s(t - \tau_{tot})^3 + \gamma s(t - \tau_{tot})^5, \qquad (5.3)$$

where τ_{tot} is the total time delay, $\tau_{tot} = \tau^* + \tau$. In the past, it was shown that the bifurcation point lost its sensitivity to variations in the time delay as τ increased. Specifically, as τ increases, the bifurcation points converge to values which are insensitive to τ but they are sensitive to mass variations in the system [110]. Hence, the cantilever-based sensor based on the bifurcation morphing approach can operate with enhanced robustness to τ_{tot} and good sensitivity to mass variations for large enough τ.

5.2.2 Forecasting bifurcations

Consider a codimension-one bifurcation where the change rate of the amplitude of the dynamics of a system can be expressed as

$$\dot{r} = r\left[\alpha(\mu - \mu_c) - p(r)\right], \qquad (5.4)$$

where α is a fixed parameter (which is generally unknown unless an accurate model of the system is provided), μ is a (known) control parameter, μ_c is a critical value of the control parameter (where a bifurcation occurs), and $p(r)$ is a polynomial function of r with $p(0) = 0$ (and assumed to be independent of the control parameter μ). The system has a fixed point at $r = 0$ in the pre-bifurcation regime. In the post-bifurcation regime, there are additional fixed points $\tilde{r}$ given by $p(\tilde{r}) = \alpha(\mu - \mu_c)$. Also, the change rate of

amplitude λ at time t is defined as

$$\lambda(\mu, r) \;=\; \frac{d \log r}{dt} = \frac{1}{r}\dot{r} = \alpha(\mu - \mu_c) - p(r). \tag{5.5}$$

Chapter IV provides details regarding the use of λ to forecast bifurcations. In particular, Chapter IV numerically and experimentally shows that this method can forecast supercritical and subcritical Hopf bifurcations and saddle-node bifurcations accurately. Furthermore, when forecasting subcritical Hopf bifurcations and saddle-node bifurcations, this approach successfully predicts the locations and amplitudes of the saddle-nodes, and the unstable branches of the bifurcation diagram. This approach is safe as the system operates only in the pre-bifurcation regime, and all required data is collected in the pre-bifurcation regime. Furthermore, (once α is identified) this approach can forecast the bifurcation point and the bifurcation diagram very quickly and accurately, because data collected for a single perturbation given to the system (at a single μ in the pre-bifurcation regime) is sufficient for forecasting [111].

5.3 Results and Discussion

5.3.1 Experimental setup

A clamped-free aluminum beam with piezo actuators and sensors is used. As shown in FIG. 5.1, a piezo-sensor and a pair of piezo-actuators are attached to the aluminum beam. The sensor output is sent to a real-time processor. The sensor signal is input to the real-time processor. This data is stored and also used to create a designed nonlinear feedback excitation. Note that the unavoidable time delay τ^* is generated during the process of storing data and creating the nonlinear feedback excitation (STEP1). The controller inserts an additional time delay τ (STEP2) before the nonlinear feedback is amplified and sent to the piezo-actuators on the beam.

The dimensions of the aluminum beam and those of a single piezo actuator patch are provided in Tab. 5.1. The total mass of the cantilever beam with the piezo actuators attached to both sides of the beam is approximately $M \approx 34.5$ g. To simulate mass variations, small amounts of mass are added to the tip of the aluminum beam in increments of approximately $m = 20$ mg. Note that $\frac{m}{M}$ is approximately 6×10^{-4}.

Herein, only the supercritical Hopf bifurcation is considered with fixed nonlinear gains of $\beta = -0.01$ and $\gamma = 0$ in Eq. (5.3). Note that μ is the linear feedback gain in Eq. (5.3), and hence it is the controlled parameter for the experiments. Also, note that τ is increased by the controller, and τ^* is the unavoidable time delay (unknown quantity). Finally, note that the proposed sensor measures variations in the points of the bifurcation diagram $\tilde{\mu}(\tilde{r})$, instead of just the bifurcation point μ_c. Here, $\tilde{r}$ represents the amplitude of the stable limit cycle in the post-bifurcation regime corresponding to a value $\tilde{\mu}$ of the linear gain. Thus, $\mu_c = \tilde{\mu}(\tilde{r} = 0)$.

5.3.2 Additional time delay

To test the effects of the time delay on the system, an additional time delay τ was added in the controller. In the experiments, τ was varied from 0 ms to 5 ms with a step of 0.01 ms. At each value of the time delay τ, the bifurcation diagram was estimated. For clarity, this estimation (which is not used for sensing) was done just by the classical

Table 5.1: Dimensions of the components of the sensor

Aluminum beam	Length	280 mm
	Width	27.5 mm
	Thickness	1.4 mm
	Density	2660 kg/m^3
Piezo actuator	Length	60 mm
	Width	15 mm
	Thickness	1 mm
	Density	7800 kg/m^3
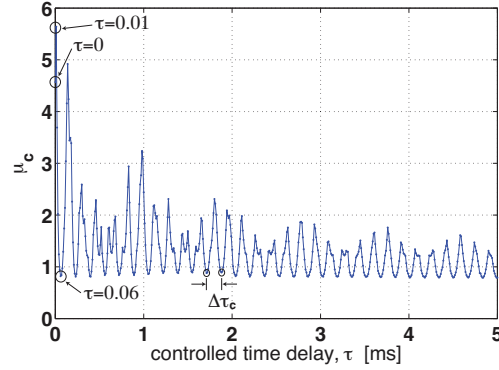
Figure 5.2: As τ is increased, the fluctuation of the bifurcation points along the τ-axis is restrained. The increased time delay enhances the robustness of the sensor by reducing the undesirable high sensitivity to variations in the time delay.

technique of sweeping parameters across the bifurcation point. When $\tau = 0$ (i.e. $\tau_{tot} = \tau^*$), the bifurcation point was found to be $\mu_c \approx 4.57$. As shown in FIG. 5.2, μ_c changes significantly as τ varies from 0 ms to 0.06 ms. These changes in the bifurcation point within a narrow range of τ_{tot} is undesirable because sensing cannot be robust to fluctuations in τ_{tot}.

In FIG. 5.2, the fluctuations of the bifurcation point μ_c due to the variation in the time delay is gradually restrained as τ increases. For example, comparing the region of $\tau = 0 \sim 1$ ms and the region of $\tau = 4 \sim 5$ ms, one may note how the increased time delay reduces the influence of the variation in the time delay. The experimental results shown in FIG. 5.2 are consistent with the numerical results previously presented for a FEM model of the cantilever beam with nonlinear feedback excitation [110].

To evaluate the sensitivity of the sensor, one can define a non-dimensional relative sensitivity as

$$S_q^P = \frac{\frac{\Delta P}{P}}{\frac{\Delta q}{q}}, \tag{5.6}$$

where P is the parameter used for sensing, and q is the system property of which variations are to be detected. In the experiments, the parameter P represents the $\tilde{\mu}$ values

a. bifurcation diagrams when $\tau = 1$ ms

b. bifurcation diagrams when $\tau = 4.95$ ms
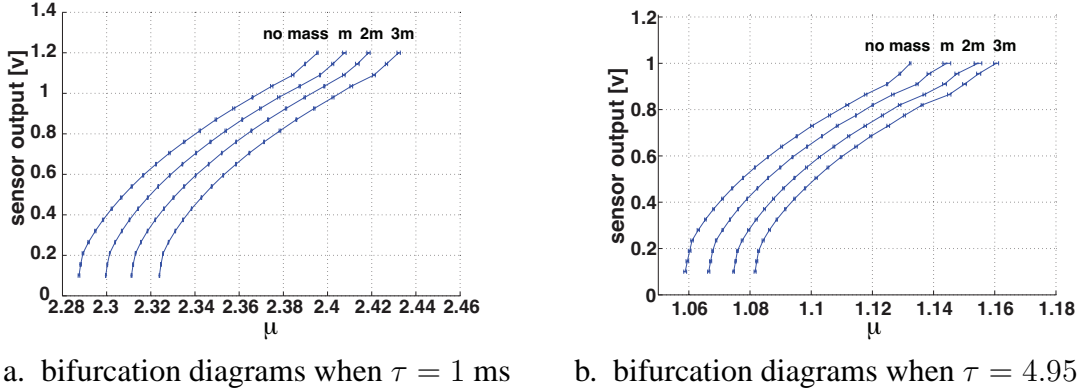
Figure 5.3: While undesirable high sensitivity to variations in the time delay is reduced as τ is increased, the relative sensitivity to mass variations is maintained at the same order of magnitude.

in the bifurcation diagram $\tilde{\mu}(\tilde{r})$, and the system property q is the mass of the system M. Hence, the relative sensitivity of interest is $S_M^{\tilde{\mu}}$. While the undesirable large fluctuation of the bifurcation boundary in the τ-μ_c space (as shown in FIG. 5.2) is restrained as τ increases, the relative sensitivity to mass variation has been shown computationally to be maintained [110]. Herein, we observe experimentally the same behavior. Once significantly large fluctuations (observed before $\tau \approx 1$ ms) are reduced, the relative sensitivity is maintained at a level of $O(10)$ as τ varies. Sample cases are presented in FIG. 5.3 for mass variations ΔM of 0, m, $2m$, and $3m$. For $\tau = 1$ ms (FIG. 5.3a), the relative sensitivity is $S_M^{\tilde{\mu}} \approx 9.1$. For $\tau = 4.95$ ms (FIG. 5.3b), the relative sensitivity is $S_M^{\tilde{\mu}} \approx 11.9$. The relative sensitivities at other time delays have been observed to have similar magnitudes also.

The curve shown in FIG. 5.2 has local minima (which are smaller than 1) at time delays $\tau_{c,i}$. The relative sensitivity of the bifurcations to mass variations is observed to approach zero at these values of the time delay. Nonetheless, the proportionality of $\Delta\tilde{\mu}$ to mass variations was experimentally measured at several time delays $\tau_{c,i}$, and that proportionality could still be observed despite the significantly low sensitivity. As the relative sensitivity becomes smaller, however, it is likely that sensing can be significantly affected

a. shifts in linear mode frequency

b. shifts in linear mode frequency (detail)
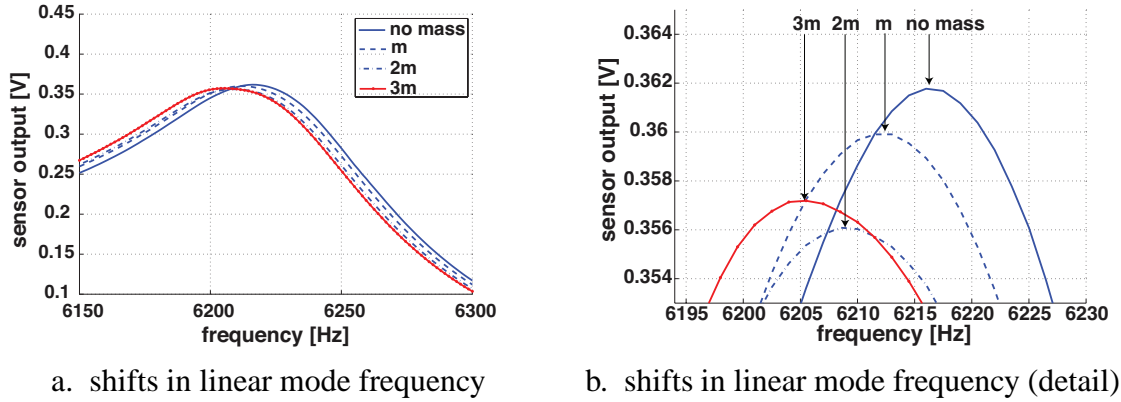
Figure 5.4:

The relative sensitivity of the linear mode frequency (6216 Hz) in similar level with the frequency of the limit cycle (6026 Hz) is $S_M^{\omega_r} \approx 0.97$ which is approximately one order of magnitude smaller than the proposed sensor.

by small errors or noise. Interestingly, the intervals between $\tau_{c,i}$ and $\tau_{c,i+1}$ are approximately constant, $\Delta\tau_c \approx 0.16$ ms. That is a value very close to the period of the limit cycle of the system near the bifurcation point, which is $T = 0.166$ ms.

The reason why the sensitivity of the bifurcation points to $\Delta\tau$ is significantly low for delays near $\tau_{c,i}$ may be explained by the fact that the sensitivity of the bifurcation points to small changes in the frequency (or period) of the limit cycle is very low. That is consistent with analytical results for a simple two-degree-of-freedom spring-mass system subject to nonlinear feedback excitations [110], where the bifurcation point is a function of the frequency of the limit cycle which appears just after the bifurcation. The correlation between the value of $\Delta\tau_c$ and the period of the limit cycle indicates that the loss of sensitivity of the sensor may take place independent of the time delay, at a certain phase of the dynamics of the system (and that phase is constant as the time delay varies). Note that it is difficult to estimate the exact phase which causes the loss of sensitivity because τ_{tot} cannot be accurately identified as τ^* is unknown.

a. r-λ space
b. μ-λ space
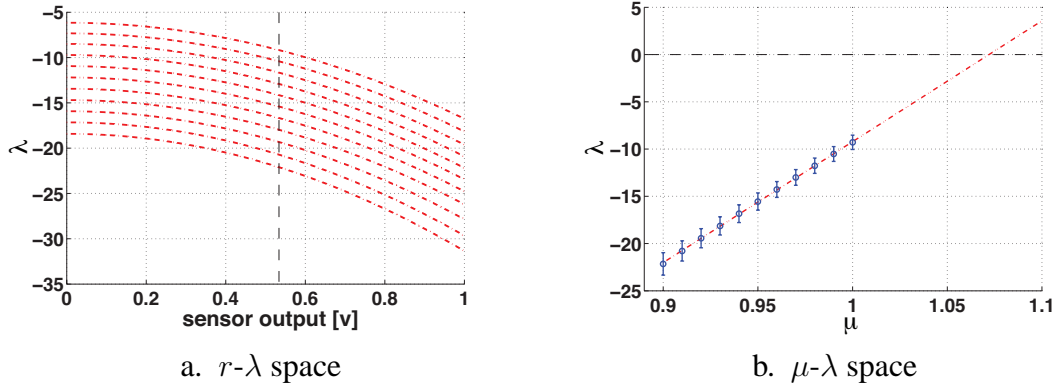
Figure 5.5: α is estimated in range of μ values with $\mu_{min} = 0.9$ and $\mu_{max} = 1$. The top figure shows the fitted curves in r-λ space based on λ values obtained from experimental data at different μ values. In the bottom figure, r (sensor output [V]) is chosen at 0.55 [V] and the fitted line in μ-λ space is presented. Identified α (based on the slopes of the fitted lines at various amplitudes) is 126.2 (with standard deviation of 3.5).

5.3.3 Cantilever-based sensing

The novel cantilever-based sensor based on forecasting bifurcation morphing was experimentally tested for detecting mass variations. The common sensing approach of monitoring linear resonant frequency shifts was also tested using the same cantilever beam. To compare these two approaches, a linear resonant frequency of $\omega_r \approx 6216$ Hz was monitored. This frequency was used because the frequency of the limit cycle near the bifurcation point is near 6216 Hz, at approximately 6026 Hz.

Based on the frequency-amplitude plot in FIG. 5.4, the relative sensitivity of the corresponding linear frequency to mass variation is $S_M^{\omega_r} \approx 0.97$. Note that this value is approximately one order of magnitude smaller than the sensitivity obtained by monitoring the points on the bifurcation diagram. One may compare the relative sensitivities for different points on the bifurcation diagram $\tilde{\mu}$ and the linear mode frequency ω_r. In doing so, the level of accuracy of measuring $\tilde{\mu}$ and ω_r should be considered also. In that context one may note that obtaining the bifurcation diagram is straightforward and accurately

done using bifurcation forecasting based directly on the time series data, while capturing the resonant frequency can be challenging especially when a large damping is present. Furthermore, the forecasting approach enables very quick and accurate characterization of the overall bifurcation diagram. Particularly, the forecasting approach can be employed in its most accurate fashion when used for high sensitivity sensing. First, an accurate value of α can be identified through repeated calibration tests in the range of μ of interest (in the pre-bifurcation region) as shown in FIG. 5.5. Second, a fixed value of μ for sensor operation can be accurately chosen (near the known bifurcation point). Third, various time delays can be applied and tested for enhancing the performance of the sensor. Fourth, as the forecasting approach takes advantages of the large amounts of data obtained from a single recovery of the system, just adding a few repeated recovery cycles can greatly enhance the accuracy of the forecasted bifurcation diagram with little (experimental) effort. As shown in FIG. 5.3, the horizontal error-bars for most of the predicted points of the bifurcation diagram are very narrow. That indicates that accurate values are obtained by the forecasting approach when a well established calibration process is used. Therefore, the actual performance difference between the proposed sensing approach and the shifts in linear mode frequency can be larger than that revealed by the comparison of the relative sensitivities.

After calibration, the proposed cantilever-based sensor was tested for detecting mass variations of m, $2m$ and $3m$ at $\tau = 4.95$ ms. The proportionality p_i is defined as

$$p_i = \frac{\Delta \tilde{\mu}_{i \times m}(\tilde{r})}{\Delta \tilde{\mu}_m(\tilde{r})}, \tag{5.7}$$

where the subscript indicates the level of mass variation. For ideal sensing and proportionality, each p_i should have the integer value of i. As shown in FIG. 5.6, the cantilever-based sensor based on the proposed approach exhibits remarkable proportionality in the range of
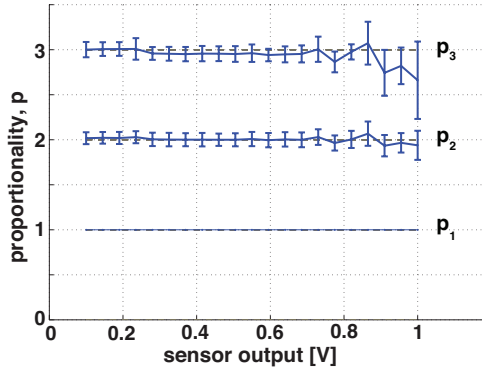
Figure 5.6: The cantilever-based sensor by the proposed approach demonstrates remarkable proportionality in the range of applied mass variations.

applied mass variations (when r is chosen in a proper range).

5.4 Conclusions

The application of bifurcation morphing created by nonlinear feedback excitations has been demonstrated for a cantilever-based sensor. Two novel techniques have been implemented to enhance the cantilever-based sensor.

First, short and unavoidable time delays in the controller can cause undesirable high sensitivity of the bifurcation points to small fluctuations in this time delay. Additional time delay in the controller can reduce this undesirable sensitivity without significantly affecting the high performance of sensing. However, upon studying the effects of additional time delay, periodic loss of sensitivity has been observed. At those time delays, the bifurcation morphing has been observed to lose its sensitivity to both variations in the time delay and in the mass. The periodicity of the loss of sensitivity was observed to be correlated with the period of the limit cycle (in the post-bifurcation regime). That may be caused by a certain delay-independent phase of the dynamics of the system.

Second, detecting bifurcation points by sweeping parameters through the bifurcation point takes a long time. The approach of forecasting bifurcations was applied and was

shown to significantly reduce the time required to detect bifurcation points and measure the overall bifurcation diagram. This forecasting approach has been experimentally shown to be quick and accurate when applied to the cantilever-based sensor. Comparing sensitivities, the bifurcation morphing approach has been observed to be about one order of magnitude higher than that of the linear mode frequency shift. Furthermore, the bifurcation diagrams obtained by the forecasting approach have been shown to have remarkable accuracy (with very small errors), especially when the sensor system is precisely calibrated.

The experimental results of mass sensing highlight the high performance of the proposed cantilever-based mass sensor. Nonetheless, this approach can be applied to sensing various other parametric variations in a diversity of systems of interest.

CHAPTER VI

Conclusions

6.1 Contributions

The original contributions of this dissertation can be summarized as follows:

- In Chapter II, various issues regarding application of the SVF approach have been discussed. To achieve the most important property of the SVF approach, which is the linearity of the SVFs for single parameter variations, an approach for filtering sample points was introduced with a focus on the most important parameter of interest. By filtering, one can generally ensure a satisfactory level of linearity for all parameters to be reconstructed. After filtering, the re-selection process is performed by investigating the SVFs for each single parameter variation. The possible significant loss of sensitivity and the possible linear dependence among distinct parameters due to filtering have been discussed. Thus, certain parameters had to be eliminated from the reconstruction process. A correction factor has been introduced to resolve the weak nonlinearity of the SVFs of certain parameter variations. The correction factor has been calculated from test SVFs of known single parameter variations. The parameter variations identified using the correction factor have been shown to be very accurate. Using AFM as an example chaotic system for demonstration of the new approaches, the major influence of the higher harmonics onto the tapping mode

AFM dynamics has been discussed. For certain regimes, higher order modes have been shown to predict a chaotic dynamics for the system although a single-mode approximation predicts limit cycle oscillations.

- In Chapter III, new studies of the bifurcation morphing and nonlinear feedback excitation have been presented. The primary topic was the time delay. Time delay is unavoidable in feedback control systems. This naturally embedded time delay produces undesirable high sensitivity of bifurcation morphing to small variations in the time delay, and that makes it difficult to achieve high-sensitivity. As the time delay is increased by the controller, the bifurcation boundary is observed to converge onto a small area in the parameter space. Furthermore, the convergence/stabilization of the bifurcation boundary significantly reduces the sensitivity of the bifurcation morphing to fluctuations in the time delay. As a consequence, the additional time delay enhances the bifurcation morphing method by reducing and stabilizing the stable region of the dynamics in the parameter space.

- In Chapter IV, a method of characterizing the dynamics of a nonlinear system during its transient recovery to a stable limit cycle or a stable fixed point after perturbations (in the pre-bifurcation regime) was presented. The proposed approach is designed for forecasting bifurcations of fixed points or limit cycles. By keeping all higher order (nonlinear) information in the formulation, the perturbation levels do not have to be small. In most cases, operating with larger perturbations is a good way to resolve accuracy issues for measuring small perturbations and to obtain better predictions of the bifurcations. The proposed technique enables the use of larger perturbations which broadens its applicability as compared to existing techniques based on the critical slowing down. In addition to predicting where bifurcations

occur, the proposed approach can be used to anticipate the type of the bifurcations (supercritical or subcritical) and predict their branches without exploring the post-bifurcation regime. Due to the dramatic change in the dynamics at bifurcations, predicting subcritical and saddle-node bifurcations without placing the system in the post-bifurcation regime provides great advantages in many applications.

- In Chapter V, bifurcation morphing by nonlinear feedback excitation was applied to cantilever-based sensors. The two novel techniques discussed in Chapter III and Chapter IV were implemented to enhance the proposed cantilever-based sensor. First, additional time delay in the controller was applied. A periodic loss of sensitivity was observed. At those time delays, the bifurcation morphing has been observed to lose its sensitivity to both variations of the time delay and the sensed mass. The periodicity of the loss of sensitivity in synchronization with the period of the limit cycle suggests that the low sensitivity occurs at a certain phase of the dynamics of the system, and the phase is independent of the time delay. Second, the approach of forecasting bifurcations was applied to significantly reduce the time required to detect bifurcation points and bifurcation diagrams. The forecasting approach was experimentally shown to be quick and accurate in application to the proposed cantilever-based sensing. Comparing the bifurcation morphing and the linear mode frequency shift, the relative sensitivity of bifurcation morphing was observed to be one order of magnitude higher. Furthermore, obtaining bifurcation diagrams by the forecasting approach was shown to have remarkable accuracy with very small errors, when it is specifically calibrated for a known sensor system. The experimental results of mass sensing demonstrate the high performance of the proposed cantilever-based sensor.

6.2 Future Research

Below are some ideas for future research that may expand the topics presented in this dissertation.

- **Development of MEMS/NEMS cantilever-based sensors using the approach of forecasting bifurcation morphing with delayed nonlinear feedback excitation**

  The prototype of the cantilever-based sensor demonstrated quick, robust and accurate performance of sensing. Furthermore, the relative sensitivity of the proposed sensor was observed to be one order of magnitude larger than that of the common approach of measuring linear frequency shifts. Also, detecting bifurcation diagrams can be more accurate than measuring the frequency of the resonant mode. These experimental results suggest that the development of MEMS/NEMS sensing device using the proposed approach could impact MEMS sensing significantly.

- **Attractor and bifurcation morphing modes for various types of structures**

  Cantilever-beam structures have been considered in this work. Nonetheless, theoretically all of the proposed approaches are not limited to a certain type of structure. One of the area of recommended future work is the application of the proposed techniques to various types of other structures.

- **Design of new nonlinear feedback excitation to induce different types of bifurcations for application to cantilever-based sensing**

  As bifurcations in the proposed approach are induced by specifically designed nonlinear feedback excitations, various types of bifurcations can be tested by re-designing the feedback excitation. For example, subcritical bifurcations can be tested for cantilever-based sensing. As the jump phenomena at a subcritical bifurcation point

or at a saddle-node bifurcation point are more dramatic changes in the dynamics than supercritical bifurcation, it is likely that they can be detected with higher sensitivity. Nonetheless, the system is affected by small external disturbances also. Hence, further studies are needed to make the sensor robust to undesirable external disturbances.

- **Development of the cantilever-based sensor using multiple piezo-sensors for two dimensional bifurcation boundary morphing to detect multiple simultaneous parameter variations**

Two dimensional bifurcation boundary morphing was numerically discussed and shown to have high sensitivity and ability to detect multiple simultaneous parameter variations [42,110]. The cantilever-based sensor was developed for one dimensional bifurcation morphing for detecting a single parameter variation in this dissertation. The development and experimental test of a sensor using two or larger dimensional bifurcation morphing would be the next step.

- **Application of the forecasting approach to multidisciplinary areas of research interests**

In addition to the bifurcation point, the proposed approach of forecasting bifurcations in this dissertation is capable of predicting exact amplitudes and locations of the saddle-nodes and the stable/unstable branches of the bifurcation diagram. This ability of characterizing bifurcations in the pre-bifurcation regime with easy applicability (no controller needed) can have significant advantages in applications to a diversity of systems which requires non-invasive evaluations. Those may include biomedical applications, such as cardiac dynamics, asthma or epileptic seizures. As this approach is shown to have remarkable accuracy, those applications may also

include engineered systems, such as aeroelastic systems encountering gusts during flight.

BIBLIOGRAPHY

BIBLIOGRAPHY

[1] G. Binnig, C. F. Quate, and C. Gerber. Atomic force microscope. *Physical Review Letters*, 56(9):930 – 933, 1986.

[2] MH Lee and WH Jhe. General theory of amplitude-modulation atomic force microscopy. *Physical Review Letters*, 97(3):id. 036104, 2006.

[3] SM Lin, CT Liauh, WR Wang, and SH Ho. Analytical solutions of the first three frequency shifts of afm non-uniform probe subjected to the lennard-jones force. *Ultramicroscopy*, 106(6):508 – 515, 2006.

[4] M Tsukada, N Sasaki, R Yamura, N Sato, and K Abe. Features of cantilever motion in dynamic-mode afm. *Surface Science*, 401(3):355 – 363, 1998.

[5] K Wolf and O Gottlieb. Nonlinear dynamics of a noncontacting atomic force microscope cantilever actuated by a piezoelectric layer. *Journal of Applied Physics*, 91(7):4701 – 4709, 2002.

[6] NA Burnham, AJ Kulik, G Gremaud, and GAD Briggs. Nanosubharmonics - the dynamics of small nonlinear contacts. *Physical Review Letters*, 74(25):5092 – 5095, 1995.

[7] R Garcia and A San paulo. Attractive and repulsive tip-sample interaction regimes in tapping-mode atomic force microscopy. *Physical Review B*, 60(7):4961 – 4967, 1999.

[8] O Sahin, CF Quate, O Solgaard, and A Atalar. Resonant harmonic response in tapping-mode atomic force microscopy. *Physical Review B*, 69(16):id. 165416, APR 2004.

[9] MV Salapaka, HS Bergh, J Lai, A Majumdar, and E McFarland. Multi-mode noise analysis of cantilevers for scanning probe microscopy. *Journal of Applied Physics*, 81(6):2480 – 2487, 1997.

[10] M Balantekin and A Atalar. Enhanced higher-harmonic imaging in tapping-mode atomic force microscopy. *Applied Physics Letters*, 87(24):id. 243513, DEC 12 2005.

[11] M Balantekin and A Atalar. Enhancing higher harmonics of a tapping cantilever by excitation at a submultiple of its resonance frequency. *Physical Review B*, 71(12):id. 125416, MAR 2005.

[12] TR Rodriguez and R Garcia. Compositional mapping of surfaces in atomic force microscopy by excitation of the second normal mode of the microcantilever. *Applied Physics Letters*, 84(3):449 – 451, 2004.

[13] RW Stark and WM Heckl. Higher harmonics imaging in tapping-mode atomic-force microscopy. *Review of Scientific Instruments*, 74(12):5111 – 5114, 2003.

[14] RW Stark. Spectroscopy of higher harmonics in dynamic atomic force microscopy. *Nanotechnology*, 15(3):347 – 351, 2004.

[15] RW Stark, G Schitter, M Stark, R Guckenberger, and A Stemmer. State-space model of freely vibrating and surface-coupled cantilever dynamics in atomic force microscopy. *Physical Review B*, 69(8):id. 085412, FEB 2004.

[16] S. W. Doebling, C. R. Farrar, M. B. Prime, and D. W. Shevitz. Damage identification and health monitoring of structural and mechanical systems from changes in their vibration characteristics: a literature review. *Report LA-13070-MS, Los Alamos National laboratories, Los Alamos, NM*, 1996.

[17] C. H. Loh and I. C. Tou. A system-identification approach to the detection of changes in both linear and nonlinear structural parameters. *Earthquake Engineering & Structural Dynamics*, 24(1):85–97, January 1995.

[18] M. O. Abdalla, K. M. Grigoriadis, and D. C. Zimmerman. Enhanced structural damage detection using alternating projection methods. *Aiaa Journal*, 36(7):1305–1311, July 1998.

[19] R. S. Pappa, G. H. James, and D. C. Zimmerman. Autonomous modal identification of the space shuttle tail rudder. *Journal of Spacecraft and Rockets*, 35(2):163–169, Mar-Apr 1998.

[20] D. C. Zimmerman. Model validation and verification of large and complex space structures. *Inverse Problems In Engineering*, 8(2):93–118, 2000.

[21] K. D'Souza and B. I. Epureanu. Damage detection in nonlinear systems using system augmentation and generalized minimum rank perturbation theory. *Smart Materials & Structures*, 14(5):989–1000, October 2005.

[22] V. K. Amaravadi, K. Mitchell, V. S. Rao, and M. M. Derriso. Structural integrity monitoring of composite patch repairs using wavelet analysis and neural networks. *Proceedings of SPIE: Smart Structures and Materials 2002: Smart Structures and Integrated Systems*, 4701(1):156–166, 2002.

[23] B. Amizic, V. K. Amaravadi, V. S. Rao, and M. M. Derriso. Two-dimensional wavelet mapping techniques for damage detection in structural systems. *Proceedings of SPIE: Smart Structures and Materials 2002: Modeling, Signal Processing, and Control*, 4693(1):267–278, 2002.

[24] H. Sohn and C. R. Farrar. Damage diagnosis using time series analysis of vibration signals. *Smart Materials & Structures*, 10(3):446–451, June 2001.

[25] J. M. Nichols, L. N. Virgin, M. D. Todd, and J. D. Nichols. On the use of attractor dimension as a feature in structural health monitoring. *Mechanical Systems and Signal Processing*, 17(6):1305–1320, November 2003.

[26] J. M. Nichols, S. T. Trickey, M. D. Todd, and L. N. Virgin. Structural health monitoring through chaotic interrogation. *Meccanica*, 38(2):239–250, 2003.

[27] J. M. Nichols, M. D. Todd, and J. R. Wait. Using state space predictive modeling with chaotic interrogation in detecting joint preload loss in a frame structure experiment. *Smart Materials & Structures*, 12(4):580–601, August 2003.

[28] J. M. Nichols, M. D. Todd, M. Seaver, and L. N. Virgin. Use of chaotic excitation and attractor property analysis in structural health monitoring. *Physical Review E*, 67(1), January 2003.

[29] B. I. Epureanu, L. S. Tang, and M. P. Paidoussis. Exploiting chaotic dynamics for detecting parametric variations in aeroelastic systems. *Aiaa Journal*, 42(4):728–735, April 2004.

[30] B. I. Epureanu and S. H. Yin. Identification of damage in an aeroelastic system based on attractor deformations. *Computers & Structures*, 82(31-32):2743–2751, December 2004.

[31] B. I. Epureanu, S. H. Yin, and M. M. Derriso. Attractor-based damage detection in a plate subjected to supersonic flows. *Proceedings of SPIE: Health Monitoring and Smart Nondestructive Evaluation of Structural and Biological Systems III*, 5394(1):340–350, 2004.

[32] R. S. Chancellor, R. M. Alexander, and S. T. Noah. Detecting parameter changes using experimental nonlinear dynamics and chaos. *Journal of Vibration and Acoustics-Transactions of the Asme*, 118(3):375–383, July 1996.

[33] W. J. Wang, Z. T. Wu, and J. Chen. Fault identification in rotating machinery using the correlation dimension and bispectra. *Nonlinear Dynamics*, 25(4):383–393, August 2001.

[34] D. Chelidze, J. P. Cusumano, and A. Chatterjee. A dynamical systems approach to damage evolution tracking, part 1: Description and experimental application. *Journal of Vibration and Acoustics-Transactions of the Asme*, 124(2):250–257, April 2002.

[35] J. P. Cusumano, D. Chelidze, and A. Chatterjee. A dynamical systems approach to damage evolution tracking, part 2: Model-based validation and physical interpretation. *Journal of Vibration and Acoustics-Transactions of the Asme*, 124(2):258–264, April 2002.

[36] B. I. Epureanu, S. H. Yin, and M. M. Derriso. High-sensitivity damage detection based on enhanced nonlinear dynamics. *Smart Materials & Structures*, 14(2):321–327, April 2005.

[37] I. Trendafilova. State space modelling and representation for vibration-based damaged assessment. *Damage Assessment of Structures, Proceedings*, 245-2:547–555, 2003.

[38] I. Trendafilova. A state space based approach to health monitoring of vibrating structures. *Modern Practice In Stress and Vibration Analysis*, 440-4:203–210, 2003.

[39] A Hashmi and B Epureanu. Sensitivity resonance and attractor morphing quantified by sensitivity vector fields for parameter reconstruction. *Nonlinear Dynamics*, 45(3-4):319 – 335, 2006.

[40] A. I. Hashmi and B. I. Epureanu. Sensitivity vector fields for damage detection and sensing. *Smart Structures and Materials 2005: Sensors and Smart Structures Technologies for Civil, Mechanical, and Aerospace, PTS 1 and 2*, 5765:236 – 244, 2005.

[41] B. I. Epureanu, S. H. Yin, and E. H. Dowell. Enhanced nonlinear dynamics for accurate identification of stiffness loss in a thermo-shielding panel. *Nonlinear Dynamics*, 39(1-2):197–211, January 2005.

[42] S. H. Yin and B. I. Epureanu. Enhanced nonlinear dynamics and monitoring bifurcation morphing for the identification of parameter variations. *Journal of fluids and structures*, 21(5-7):543–559, December 2005.

[43] F. Jamitzky, M. Stark, W. Bunk, W. M. Heckl, and R. W. Stark. Chaos in dynamic atomic force microscopy. *Nanotechnology*, 17(7):S213–S220, Jan 2006.

[44] J. Lim and B. I. Epureanu. Multimode dynamics of atomic-force-microscope tip-sample interactions and application of sensitivity vector fields. *Proceedings of SPIE: Sensors and Smart Structures Technologies for Civil, Mechanical, and Aerospace Systems 2007*, 6529(1):65293Y, 2007.

[45] J. Lim and B. I. Epureanu. Sensitivity vector fields for atomic force microscopes. *Nonlinear Dynamics*, 59(1):113–128, 01 2010.

[46] W. M. Zhang, G. Meng, J. B. Zhou, and J. Y. Chen. Nonlinear dynamics and chaos of microcantilever-based tm-afms with squeeze film damping effects. *Sensors-Basel*, 9(5):3854–3874, Jan 2009.

[47] M. Liu and D. Chelidze. A new type of atomic force microscope based on chaotic motions. *Int J Nonlin Mech*, 43(6):521–526, Jan 2008.

[48] A. Gupta, D. Akin, and R. Bashir. Single virus particle mass detection using microresonators with nanoscale thickness. *Applied Physics Letters*, 84(11):1976–1978, Jan 2004.

[49] B. Ilic, H. G. Craighead, S. Krylov, W. Senaratne, C. Ober, and P. Neuzil. Attogram detection using nanoelectromechanical oscillators. *Journal of Applied Physics*, 95(7):3694–3703, Jan 2004.

[50] B. Ilic, Y. Yang, and H. G. Craighead. Virus detection using nanoelectromechanical devices. *Applied Physics Letters*, 85(13):2604–2606, Jan 2004.

[51] D. Lange, C. Hagleitner, A. Hierlemann, O. Brand, and H. Baltes. Complementary metal oxide semiconductor cantilever arrays on a single chip: Mass-sensitive detection of volatile organic compounds. *Anal Chem*, 74(13):3084–3095, Jan 2002.

[52] N. V. Lavrik and P. G. Datskos. Femtogram mass detection using photothermally actuated nanomechanical resonators. *Applied Physics Letters*, 82(16):2697–2699, Jan 2003.

[53] T. Thundat, E. A. Wachter, S. L. Sharp, and R. J. Warmack. Detection of mercury-vapor using resonating microcantilevers. *Applied Physics Letters*, 66(13):1695–1697, Jan 1995.

[54] M. Narducci, E. Figueras, M. J. Lopez, I. Gracia, J. Santander, P. Ivanov, L. F., and C. Cane. Sensitivity improvement of a microcantilever based mass sensor. *Microelectron Eng*, 86(4-6):1187–1189, Jan 2009.

[55] T. P. Burg, M. Godin, S. M. Knudsen, W. Shen, G. Carlson, J. S. Foster, K. B., and S. R. Manalis. Weighing of biomolecules, single cells and single nanoparticles in fluid. *Nature*, 446(7139):1066–1069, Jan 2007.

[56] M. Li, H. X. Tang, and M. L. Roukes. Ultra-sensitive nems-based cantilevers for sensing, scanned probe and very high-frequency applications. *Nat Nanotechnol*, 2(2):114–120, Jan 2007.

[57] M. I. Younis and F. Alsaleem. Exploration of new concepts for mass detection in electrostatically-actuated structures based on nonlinear phenomena. *Journal of Computational and Nonlinear Dynamics*, 4(2):021010, Jan 2009.

[58] W. H. Zhang and K. L. Turner. Application of parametric resonance amplification in a single-crystal silicon micro-oscillator based mass sensor. *Sensor Actuat A-Phys*, 122(1):23–30, Jan 2005.

[59] J. F. Rhoads, S. W. Shaw, and K. L. Turner. Nonlinear dynamics and its applications in micro- and nanoresonators. *Proceedings of the ASME Dynamic Systems and Control Conference 2008, Pts A and B*, pages 543–572, 2009.

[60] A. Vyas, D. Peroulis, and A. K. Bajaj. A microresonator design based on non-linear 1:2 internal resonance in flexural structural modes. *J Microelectromech S*, 18(3):744–762, Jan 2009.

[61] U Bortolozzo, M. G Clerc, and S Residori. Local theory of the slanted homoclinic snaking bifurcation diagram. *Physical Review E*, 78(3):036214, Jan 2008.

[62] Andrea Sacchetti. Universal critical power for nonlinear schrodinger equations with a symmetric double well potential. *Physical Review Letters*, 103(19):194101, Jan 2009.

[63] Timothy M Lenton, Hermann Held, Elmar Kriegler, Jim W Hall, Wolfgang Lucht, Stefan Rahmstorf, and Hans Joachim Schellnhuber. Tipping elements in the earth's climate system. *Proceedings of the National Academy of Sciences of the United States of America*, 105(6):1786–1793, Jan 2008.

[64] M Scheffer, S Carpenter, JA Foley, C Folke, and B Walker. Catastrophic shifts in ecosystems. *Nature*, 413(6856):591–596, Jan 2001.

[65] Margot Parkes. Personal commentaries on "ecosystems and human well-being: Health synthesis - a report of the millennium ecosystem assessment". *Ecohealth*, 3(3):136–140, Jan 2006.

[66] JG Venegas, T Winkler, G Musch, MFV Melo, D Layfield, N Tgavalekos, AJ Fischman, RJ Callahan, G Bellani, and RS Harris. Self-organized patchiness in asthma as a prelude to catastrophic shifts. *Nature*, 434(7034):777–782, Jan 2005.

[67] B Litt, R Esteller, J Echauz, M D'Alessandro, R Shor, T Henry, P Pennell, C Epstein, R Bakay, M Dichter, and G Vachtsevanos. Epileptic seizures may begin hours in advance of clinical onset: A report of five patients. *Neuron*, 30(1):51–64, Jan 2001.

[68] PE McSharry, LA Smith, and L Tarassenko. Prediction of epileptic seizures: are nonlinear methods relevant? *Nature Medicine*, 9(3):241–242, Jan 2003.

[69] D Golomb and GB Ermentrout. Bistability in pulse propagation in networks of excitatory and inhibitory populations. *Physical Review Letters*, 86(18):4179–4182, Jan 2001.

[70] Robert M May, Simon A Levin, and George Sugihara. Complex systems - ecology for bankers. *Nature*, 451(7181):893–895, Jan 2008.

[71] C Jeffries and K Wiesenfeld. Observation of noisy precursors of dynamical instabilities. *Physical Review A*, 31(2):1077–1084, Jan 1985.

[72] K Wiesenfeld. Virtual hopf phenomenon - a new precursor of period-doubling bifurcations. *Physical Review A*, 32(3):1744–1751, Jan 1985.

[73] Vishwesha Guttal and Ciriyam Jayaprakash. Changing skewness: an early warning signal of regime shifts in ecosystems. *Ecology Letters*, 11(5):450–460, Jan 2008.

[74] S. R Carpenter, W. A Brock, J. J Cole, J. F Kitchell, and M. L Pace. Leading indicators of trophic cascades. *Ecology Letters*, 11(2):128–138, Jan 2008.

[75] N Berglund and B Gentz. Metastability in simple climate models: Pathwise analysis of slowly driven langevin equations. *Stochastics and Dynamics*, 2:327–356, Jan 2001.

[76] S. H. Strogatz. *Nonlinear Dynamics and Chaos- With Applications to Physics, Biology, Chemistry, and Engineering 1st edn*. Westview Press, 2001.

[77] Marten Scheffer, Jordi Bascompte, William A Brock, Victor Brovkin, Stephen R Carpenter, Vasilis Dakos, Hermann Held, Egbert H van Nes, Max Rietkerk, and George Sugihara. Early-warning signals for critical transitions. *Nature*, 461(7260):53–59, Jan 2009.

[78] C Wissel. A universal law of the characteristic return time near thresholds. *Oecologia*, 65(1):101–107, Jan 1984.

[79] Thomas Kleinen, Hermann Held, and Gerhard Petschel-Held. The potential role of spectral properties in detecting thresholds in the earth system: application to the thermohaline circulation. *Ocean Dynamics*, 53:53, Jan 2003.

[80] SR Carpenter and WA Brock. Rising variance: a leading indicator of ecological transition. *Ecology Letters*, 9(3):308–315, March 2006.

[81] Ryan A Chisholm and Elise Filotas. Critical slowing down as an indicator of transitions in two-species models. *Journal of Theoretical Biology*, 257(1):142–149, Jan 2009.

[82] Egbert H van Nes and Marten Scheffer. Slow recovery from perturbations as a generic indicator of a nearby catastrophic shift. *American Naturalist*, 169(6):738–47, Jun 2007.

[83] Vasilis Dakos, Marten Scheffer, Egbert H van Nes, Victor Brovkin, Vladimir Petoukhov, and Hermann Held. Slowing down as an early warning signal for abrupt climate change. *Proceedings of the National Academy of Sciences of the United States of America*, 105(38):14308–14312, Jan 2008.

[84] C P Bagowski and J E Ferrell, Jr. Bistability in the jnk cascade. *Current Biology*, 11(15):1176–82, Aug 2001.

[85] E. Doedel, A. Champneys, T. Fairgrieve, Y. Kuznetsov, B. Sandstede, and X. Wang. *AUTO 97: continuation and bifurcation software for ordinary differential equations*, 1998.

[86] K Engelborghs, T Luzyanina, and D Roose. Numerical bifurcation analysis of delay differential equations using dde-biftool. *ACM Transactions on Mathematicacl Software*, 28(1):1–21, MAR 2002.

[87] R. Szalai. *PDDE-CONT: a continuation and bifur- cation software for delay-differential equations*, 2005.

[88] J Sieber, A Gonzalez-Buelga, S. A Neild, D. J Wagg, and B Krauskopf. Experimental continuation of periodic orbits through a fold. *Physical Review Letters*, 100(24):244101, Jan 2008.

[89] Jan Sieber and Bernd Krauskopf. Control based bifurcation analysis for experiments. *Nonlinear Dynamics*, 51(3):365–377, Jan 2008.

[90] David A. W. Barton and Stephen G. Burrow. Numerical continuation in a physical experiment: Investigation of a nonlinear energy harvester. *ASME Conference Proceedings*, 2009(49019):361–368, 2009.

[91] Kiran D'Souza and Bogdan I Epureanu. Nonlinear feedback auxiliary signals for system interrogation and damage detection. *Proceedings of the Royal Society A - Mathematical Physical and Engineering Sciences*, 464(2100):3129–3148, Jan 2008.

[92] Kiran D'Souza and Bogdan I Epureanu. Detection of global and local parameter variations using nonlinear feedback auxiliary signals and system augmentation. *Journal of Sound and Vibration*, 329(13):2463–2476, Jan 2010.

[93] A Maccari. Saddle-node bifurcations of cycles in a relief valve. *Nonlinear Dynamics*, 22(3):225–247, Jan 2000.

[94] V Piccirillo, J. M Balthazar, and B. R Pontes. Analytical study of the nonlinear behavior of a shape memory oscillator: Part i-primary resonance and free response at low temperatures. *Nonlinear Dynamics*, 59(4):733–746, Jan 2010.

[95] K. W Chung, Y. B He, and B. H. K Lee. Bifurcation analysis of a two-degree-of-freedom aeroelastic system with hysteresis structural nonlinearity by a perturbation-incremental method. *Journal of Sound and Vibration*, 320(1-2):163–183, Jan 2009.

[96] T Kalmar-Nagy, G Stepan, and FC Moon. Subcritical hopf bifurcation in the delay equation model for machine tool vibrations. *Nonlinear Dynamics*, 26(2):121–142, Jan 2001.

[97] Firoz Ali Jafri, Amit Shukla, and David F Thompson. A numerical bifurcation study of friction effects in a slip-controlled torque converter clutch. *Nonlinear Dynamics*, 50(3):627–638, Jan 2007.

[98] B. Epureanu and A. Hashmi. Parameter reconstruction based on sensitivity vector fields. *Journal of Vibration and Acoustics - Transactions of the ASME*, 128(6):732–740, December 2006.

[99] SH Yin and BI Epureanu. Structural health monitoring based on sensitivity vector fields and attractor morphing. *Philosophical Transactions of the Royal Society A-Mathematical Physical and Engineering Sciences*, 364(1846):2515 – 2538, 2006.

[100] AS Paulo and R Garcia. Unifying theory of tapping-mode atomic-force microscopy. *Physical Review B*, 66(4):id. 041406, JUL 15 2002.

[101] A Sebastian, MV Salapaka, DJ Chen, and JP Cleveland. Harmonic and power balance tools for tapping-mode atomic force microscope. *Journal of Applied Physics*, 89(11):6473–6480, Jan 2001.

[102] K Yagasaki. Nonlinear dynamics of vibrating microcantilevers in tapping-mode atomic force microscopy. *Physical Review B*, 70(24):id. 245419, DEC 2004.

[103] X Zhao and H Dankowicz. Characterization of intermittent contact in tapping-mode atomic force microscopy. *Journal of Computational and Nonlinear Dynamics*, 1(2):109–115, APR 2006.

[104] M Ashhab, MV Salapaka, M Dahleh, and I Mezic. Melnikov-based dynamical analysis of microcantilevers in scanning probe microscopy. *Nonlinear Dynamics*, 20(3):197 – 220, 1999.

[105] S Rutzel, SI Lee, and A Raman. Nonlinear dynamics of atomic-force-microscope probes driven in lennard-jones potentials. *Proceedings of the Royal Society of London Series A-Mathematical Physical and Engineering Sciences*, 459(2036):1925 – 1948, 2003.

[106] O Pfeiffer, C Loppacher, C Wattinger, M Bammerlin, U Gysin, M Guggisberg, S Rast, R Bennewitz, E Meyer, and HJ Guntherodt. Using higher flexural modes in non-contact force microscopy. *Applied Surface Science*, 157(4):337 – 342, 2000.

[107] Jacob N Israelachvili. *Intermolecular and surface forces*. London : Academic Press, Inc., 1992.

[108] M Basso, L Giarre, M Dahleh, and I Mezic. Complex dynamics in a harmonically excited lennard-jones oscillator: Microcantilever-sample interaction in scanning probe microscopes. *Journal of Dynamic Systems Measurement and Control*, 122(1):240 – 245, 2000.

[109] SM Baer, T Erneux, and J Rinzel. The slow passage through a hopf-bifurcation - delay, memory effects, and resonance. *Siam Journal of Applied Mathematics*, 49(1):55–71, Jan 1989.

[110] Joosup Lim and Bogdan I Epureanu. Exploiting delayed nonlinear feedback for sensing based on bifurcation morphing. *International Journal of Structural Stability and Dynamics*, accepted for publication, 2010.

[111] Joosup Lim and Bogdan I. Epureanu. Forecasting a class of bifurcations: Theory and experiment. *Phys. Rev. E*, 83(1):016203, Jan 2011.